

DISS. ETH NO. 22524

GEOMETRIC PHASES AND NOISE IN CIRCUIT QED

A thesis submitted to attain the degree of
DOCTOR OF SCIENCES of ETH ZURICH
(Dr. sc. ETH Zurich)

presented by
Simon Jacques Berger
MSc ETH Physics, ETH Zurich
born on 05.10.1985
citizen of Fahrni BE

accepted on the recommendation of
Prof. Dr. Andreas Wallraff
Prof. Dr. Jukka Pekola

2015

Cover page: Ekberg, Helsinki

*Computers are cheap
and thinking hurts.*

attributed to Uwe Ligges

ABSTRACT

This work presents experiments carried out in a framework called circuit quantum electrodynamics, which could serve to implement a viable quantum computer or quantum simulator. The quantum bits (qubits for short) which make up such a system are realized as superconducting circuits called transmons. The transmon is connected to a coplanar transmission line resonator (or a three-dimensional cavity) for manipulation and readout.

Controlling a qubit is tantamount to manipulating its wave function, in particular the phase. In addition to the familiar dynamic phase, which is the time-integral of the energy of the qubit, there is also the so-called geometric phase, which depends neither on the energy of the qubit nor on total evolution time, but only on the sequence of quantum states the qubit traverses.

This thesis experimentally explores various novel aspects of the adiabatic and cyclic geometric phase, termed Berry phase, where the control parameters of the Hamiltonian governing qubit evolution are changed cyclically and slowly in time. Using a coherent microwave drive (which serves as control field), the qubit is brought to acquire a determined amount of phase. It is found that due to the weakly anharmonic energy level structure of the transmon, the energy levels outside the computational subspace sizeably contribute to the geometric phase acquired by the qubit. These findings apply to any weakly anharmonic quantum system.

Then, the influence of noise in the control field of the qubit is examined. We find that the geometric phase is resilient to noise as long as it preserves the adiabaticity of the qubit evolution. A direct comparison with the dynamic phase shows that the dynamic phase is more affected by decoherence than the adiabatic geometric phase when exposed to the same kind of noise.

Finally, by applying different types of correlated noise, we explicitly show that the geometric dephasing of a qubit depends on the direction in which the control field traces out a path, making the geometric nature of geometric dephasing manifest. This somewhat tautological finding has profound implications for the state of the qubit: the geometric operation can either induce decoherence or restore coherence.

CONDENSÉ

Cette thèse présente des expériences réalisées dans un système appelé électrodynamique quantique en circuit. Ce système est fondé sur des circuits supraconducteurs et pourrait servir à réaliser un ordinateur quantique ou un simulateur quantique. Les deux niveaux énergétiques les plus bas d'un atome artificiel nommé transmon servent de bit quantique (en abrégé : qubit). Pour le manipuler et pour le mesurer, le qubit est relié à un résonateur à ligne de transmission planaire ou à une cavité à trois dimensions.

Contrôler un qubit revient à manipuler sa fonction d'ondes, notamment la phase. Or, une fonction d'onde peut acquérir deux genres de phase, la phase dynamique et la phase géométrique. Tandis que la phase dynamique est simplement l'intégrale sur le temps de l'énergie du système, la phase géométrique est indépendante de l'énergie et du temps total. Elle dépend seulement de la séquence des états que parcourt le qubit.

La présente thèse explore plusieurs aspects nouveaux de la phase géométrique cyclique et adiabatique, appelée phase de Berry. Dans ce cas-ci, les paramètres de contrôle de l'hamiltonien qui décrit l'évolution du qubit sont changés lentement au fil du temps. Ici, un signal micro-onde sert de champ de contrôle et est utilisé pour manipuler le qubit de sorte qu'il acquière une phase déterminée. On trouve que la structure des niveaux d'énergie peu anharmonique du transmon fait que la phase géométrique accumulée par le qubit comporte une partie de taille qui relève des niveaux d'énergie supérieurs inusités. Ce modèle s'applique à tout système peu anharmonique.

Ensuite, l'influence de bruit dans les paramètres du champ de contrôle du qubit est étudiée. On trouve que la phase géométrique du qubit est résistante au bruit tant que l'évolution du qubit demeure adiabatique. Une comparaison directe avec la phase dynamique montre que celle-ci est davantage touchée par la décohérence que la phase géométrique adiabatique exposée au même bruit.

Finalement, une série de bruits corrélés différemment sert à démontrer que le déphasage géométrique du qubit dépend de la direction dans laquelle le champ de contrôle traverse un trajet. Cette expérience corrobore la nature géométrique de ce genre de déphasage et a de profondes conséquences pour l'état du qubit : une opération géométrique peut soit induire de la décohérence, soit restaurer de la cohérence.

CONTENTS

Abstract	iii
Condensé	v
Contents	vii
List of publications	xi
Preface	1
I Prolegomena	3
1 Introduction	5
1.1 Quantum information	5
1.1.1 The quantum bit	5
1.1.2 The Bloch sphere	6
1.1.3 Density matrices	6
1.1.4 The qutrit	7
1.2 Geometric phases	8
1.2.1 The Berry phase	8
1.2.2 Berry phase & parallel transport	10
1.2.3 Generalizations of the Berry phase	11
1.2.4 Experimental observations of geometric phases	12
1.2.5 Geometric quantum computation	12
1.3 Circuit quantum electrodynamics	13
1.3.1 Introduction	13
1.3.2 Superconducting qubits	14
1.3.3 Transmon qubit	14
1.3.4 Coplanar waveguide resonators	16
1.3.5 Transmon coupled to a resonator	18
2 Experimental aspects	21
2.1 Sample fabrication	21
2.2 Cryogenic aspects	21

2.2.1	Cryostat	22
2.2.2	Microwave wiring	22
2.2.3	Sample holder	24
2.3	Signal generation	24
2.4	Data acquisition	27
2.5	Experimental basics	29
2.5.1	Dispersive readout & population reconstruction	29
2.5.2	Parametric amplifier	30
2.5.3	Microwave control	31
II Experiments		37
3	Beyond the two-level approximation	39
3.1	Experiment	40
3.1.1	Experimental idea	40
3.1.2	Sample and setup	40
3.1.3	Measurement of the geometric phase	42
3.2	Theory	44
3.2.1	Perturbative treatment of higher levels	44
3.2.2	Applicability to experiment	46
3.3	Adiabaticity	47
3.4	Conclusion	47
4	Noise resilience of the Berry phase	49
4.1	Analytical expressions	50
4.1.1	Noise-induced dispersion in phase	50
4.1.2	Noise-induced dephasing	52
4.2	Experiments	53
4.2.1	Experimental idea	53
4.2.2	System parameters	54
4.2.3	Measurement scheme	55
4.2.4	Histograms	55
4.2.5	Dependence of coherence on solid angle	56
4.2.6	Varying the noise amplitude	57
4.2.7	Coherence of the dynamic phase	57
4.2.8	Comparison of dynamic and geometric phase	58
4.3	Conclusion	58
5	Geometric dephasing	61
5.1	Experiment	62
5.1.1	System and setup	62
5.1.2	Experimental idea	63
5.1.3	Experimental results	64
5.2	Theory	66
5.2.1	Ramsey experiment	67

5.2.2	Short and long correlation-time limits	68
5.2.3	Protocol R: ‘geometric’ echo	70
5.2.4	Protocol P: ‘complete’ echo	71
5.2.5	Discussion of parameter estimates for a, b, c	71
5.2.6	Considerations about adiabaticity	72
5.2.7	Fitting the measured coherences	73
5.3	Conclusion	75
Concluding remarks		77
III Appendices		79
A	Aspects of microwave mixers	81
A.1	Operating principle of a mixer	81
A.1.1	Three-port mixer	81
A.1.2	IQ mixer	82
A.2	Mixer calibration for sideband modulation	84
A.2.1	Removing the mirror image	84
A.2.2	Suppressing LO leakage	85
A.3	Higher harmonics of sideband mixing	86
A.4	Mixer calibration for direct modulation	87
A.4.1	Mixer calibration procedure	88
A.4.2	Off-resonant mixer calibration	91
A.5	Linearity of mixer	92
B	Noise generation	95
B.1	Ornstein-Uhlenbeck process	95
B.2	Spectral density function	96
B.3	Numerical generation of the noise	97
B.3.1	Fourier representation	97
B.3.2	Smoothing of the noise envelope	98
B.3.3	Measurements with spectrum analyser	99
Bibliography		103
Acknowledgements		117
Curriculum vitae		119

LIST OF PUBLICATIONS

This thesis is based in part on the following articles:

1. *Berger S, Pechal M, Kurpiers P, Eichler C, Shnirman S, Gefen Y, Filipp S and Wallraff A*. ‘Observation of geometric dephasing in circuit QED’. In preparation
2. *Berger S, Pechal M, Abdumalikov A A, Eichler C, Steffen L, Fedorov A, Wallraff A and Filipp S*. ‘Exploring the effect of noise on the Berry phase’. *Phys. Rev. A* **87**, 060303(R) (2013)
3. *Berger S, Pechal M, Pugnetti S, Abdumalikov A A, Steffen L, Fedorov A, Wallraff A and Filipp S*. ‘Geometric phases in superconducting qubits beyond the two-level approximation’. *Phys. Rev. B* **85**, 220502(R) (2012)

In addition, contributions have been made to the following articles:

4. *Zeytinoğlu S, Pechal M, Berger S, Abdumalikov A A, Wallraff A and Filipp S*. ‘Microwave-induced amplitude and phase tunable qubit-resonator coupling in circuit quantum electrodynamics’. Submitted to *Phys. Rev. A*. Available at arXiv: 1502.03692
5. *Gasparinetti S, Berger S, Abdumalikov A A, Wallraff A and Filipp S*. ‘Observation of the vacuum-induced Berry phase’. In preparation
6. *Pechal M, Huthmacher L, Eichler C, Zeytinoğlu S, Abdumalikov A A, Berger S, Wallraff A and Filipp S*. ‘Microwave-controlled generation of shaped single photons in circuit quantum electrodynamics’. *Phys. Rev. X* **4**, 041010 (2014)
7. *Mortemousse P A, Berger S, Sekiguchi T, Culan C, Elliman R G and Itoh K M*. ‘Hyperfine clock transitions of bismuth donors in silicon detected by spin-dependent recombination’. *Phys. Rev. B* **89**, 155202 (2014)
8. *Abdumalikov A A, Fink J M, Juliusson K, Pechal M, Berger S, Wallraff A and Filipp S*. ‘Experimental realization of non-Abelian non-adiabatic geometric gates’. *Nature* **496**, 482 (2013)
9. *Pechal M, Berger S, Abdumalikov A A, Fink J M, Mlynek J A, Wallraff A and Filipp S*. ‘Geometric phase and non-adiabatic effects in an electronic harmonic oscillator’, *Phys. Rev. Lett.* **108**, 170401 (2012)

PREFACE

A certain, quite fundamental concept of quantum mechanics had managed to lay quiet, hidden in the Schrödinger equation, for about fifty years. At times, someone (Pancharatnam, 1956; Mead and Truhlar, 1979) caught a fleeting glimpse of it, but its true nature remained elusive. Finally, though, after it had caught Berry's (1984) eye, it immediately took the spotlight in the physicists' community.

It is surprising that no-one had noticed *the geometric phase* for so long, since it pervades physics. It appears in the quantum Hall effect (Thouless et al., 1982; Simon, 1983) and the Aharonov-Bohm effect can be described in terms of a geometric phase change (Berry, 1984). Its analogue in classical mechanics, the Hannay angle (Hannay, 1985), can be used to explain the precession of Foucault's pendulum. Geometric phases are also thought to play a role in oscillations of neutrino flavours (Blasone et al., 1999).

This thesis presents new findings about the Berry phase, a kind of geometric phase, which were gained in an experimental framework known as circuit quantum electrodynamics (Blais et al., 2004). Part I provides background information on quantum information theory, geometric phases and circuit quantum electrodynamics. It also introduces the experimental setup as well as basic measurement techniques. In part II, the main results of this thesis are presented. The appendices in part III provide details on technical aspects.

PART I

PROLEGOMENA

INTRODUCTION

1.1 Quantum information

This section introduces some fundamental notions of quantum information theory which are relevant for this thesis. The quantum unit of information, the quantum bit or qubit for short, and its extension to three levels, the qutrit, are introduced. For more background, refer to the monographs by Nielsen and Chuang (2000) or by Peres (2002), which also gives an introduction to measurement theory.

1.1.1 The quantum bit

In classical information theory, information is encoded in bits. A bit can take on only two distinct values, 0 or 1. In contrast, its quantum mechanical analogue, the qubit can be in a *superposition state*, i.e. a linear combination of the basis states $|0\rangle$ and $|1\rangle$. The wave function $|\psi\rangle$ of a qubit is a vector of the form

$$|\psi\rangle = \alpha|0\rangle + \beta|1\rangle = \begin{pmatrix} \alpha \\ \beta \end{pmatrix} \quad (1.1)$$

with $\alpha, \beta \in \mathbb{C}$. To accommodate the interpretation of α and β in eq. (1.1) as probability amplitudes to observe the qubit in state $|0\rangle$ respectively $|1\rangle$, it is required that $|\alpha|^2 + |\beta|^2 = 1$. Sometimes $|\alpha|^2$ is called population of the ground state, and $|\beta|^2$ population of the excited state. Even though a projective measurement of a qubit state has only two outcomes, $|0\rangle$ and $|1\rangle$, superposition states can be used during computation. This parallelism inherent to quantum computation is an advantage of quantum bits over classical bits.

In practice, the computational states $|0\rangle$ and $|1\rangle$ are mapped directly to the two states of a spin one-half system, or to two singled out levels of an anharmonic many-level-system. Nakahara and Ohmi's (2008) text gives an introduction to major physical implementations of qubits. In this thesis, the two lowest energy levels of an artificial atom called transmon (Koch et al., 2007) are used as a qubit (see sec. 1.3).

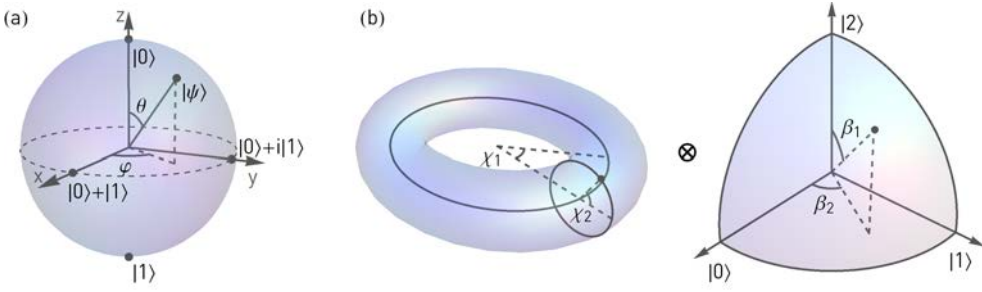


Figure 1.1: (a) The wave function $|\psi\rangle$ of a two-level system can be represented as a point on the Bloch sphere. (b) The wave function of a three-level system is a point in the product space of a torus and an octant of a sphere S^2 .

1.1.2 The Bloch sphere

The wave function eq. (1.1) can be written as

$$|\psi(\theta, \phi)\rangle = e^{i\gamma} \left(\cos\left(\frac{\theta}{2}\right)|0\rangle + e^{i\phi} \sin\left(\frac{\theta}{2}\right)|1\rangle \right),$$

where γ , θ and ϕ are real. The expectation value of an observable O with respect to the state $|\psi\rangle$ is defined as $\langle O \rangle_{|\psi\rangle} = \langle \psi | O | \psi \rangle$. From this, it appears that the global phase $e^{i\gamma}$ cannot be observed directly, so we drop it. We define the *Bloch vector* \mathbf{r} as

$$\mathbf{r} = (\langle X \rangle, \langle Y \rangle, \langle Z \rangle) = (\sin\theta \cos\phi, \sin\theta \sin\phi, \cos\theta) \quad (1.2)$$

via expectation values of the Pauli matrices

$$X = \begin{pmatrix} 0 & 1 \\ 1 & 0 \end{pmatrix}, \quad Y = \begin{pmatrix} 0 & -i \\ i & 0 \end{pmatrix}, \quad Z = \begin{pmatrix} 1 & 0 \\ 0 & -1 \end{pmatrix}.$$

It can be shown (Nakahara, 2003) that there is a bijection between $|\psi(\theta, \phi)\rangle$ and the $\mathbf{r}(\theta, \phi)$ for $0 \leq \theta \leq \pi$ and $0 \leq \phi < 2\pi$. The state of a qubit $|\psi(\theta, \phi)\rangle$ can thus be visualized as a point $\mathbf{r}(\theta, \phi)$ on the unit sphere $S^2 \subset \mathbb{R}^3$. In quantum information theory, the set of all vectors \mathbf{r} is called *Bloch* or *Poincaré sphere* (see Fig. 1.1(a)). These vectors describe the *pure states*.

1.1.3 Density matrices

The states corresponding to a vector lying inside the Bloch sphere,

$$\mathbf{r} = (r \sin\theta \cos\phi, r \sin\theta \sin\phi, r \cos\theta), \quad r \in [0, 1], \quad (1.3)$$

are called *mixed states*. These cannot be described in terms of wave functions $|\psi\rangle$, but only in terms of density matrices.

A *density matrix* describing a qubit state is a complex two-by-two matrix which is positive semi-definite and fulfils $\text{tr } \rho = 1$. A pure state $|\psi\rangle$ is associated with the density matrix

$$\rho = |\psi\rangle\langle\psi|. \quad (1.4)$$

For mixed states, there is no wave function $|\psi\rangle$ satisfying eq. (1.4).

Any density matrix ρ describing a qubit state can be written as (Nielsen and Chuang, 2000)

$$\rho = \frac{1}{2} (\text{id} + \mathbf{r} \cdot \boldsymbol{\sigma}). \quad (1.5)$$

where expectation values $\langle X \rangle$ of the spin projection operator X with respect to the state ρ are defined as $\text{tr}(X\rho)$ (and similarly for $\langle Y \rangle$ and $\langle Z \rangle$; cf. eq. (1.2)). The dot \cdot denotes the standard dot product. When ρ describes a pure state, $\rho = |\psi\rangle\langle\psi|$, we have $\rho^2 = \rho$ and therefore $|\mathbf{r}| = 1$. When ρ describes a mixed state, $|\mathbf{r}| < 1$. Thus, mixed states can be visualized as points lying within the Bloch sphere.

1.1.4 The qutrit

The representation of a pure state of a two-level system as a point on the Bloch sphere can be generalized to three-level systems, called *qutrits*. (Arvind et al., 1997). Any pure three-level state $|\psi\rangle = \alpha|0\rangle + \beta|1\rangle + \gamma|2\rangle$ can be written in a manner analogous to eq. (1.5) as

$$\rho = \frac{1}{3} (\text{id}_3 + \sqrt{3}\mathbf{r} \cdot \boldsymbol{\lambda}),$$

where \mathbf{r} is a unit vector in \mathbb{R}^8 and $\boldsymbol{\lambda} = (\lambda_1, \dots, \lambda_8)$ are the Gell-Mann matrices. These eight Hermitian, traceless and orthogonal¹ matrices are the generators of $SU(3)$ and therefore play a role similar to the Pauli matrices for the two-dimensional case. Explicitly, they are

$$\begin{aligned} \lambda_1 &= \begin{pmatrix} 0 & 1 & 0 \\ 1 & 0 & 0 \\ 0 & 0 & 0 \end{pmatrix}, & \lambda_2 &= \begin{pmatrix} 0 & -i & 0 \\ i & 0 & 0 \\ 0 & 0 & 0 \end{pmatrix}, & \lambda_3 &= \begin{pmatrix} 1 & 0 & 0 \\ 0 & -1 & 0 \\ 0 & 0 & 0 \end{pmatrix}, \\ \lambda_4 &= \begin{pmatrix} 0 & 0 & 1 \\ 0 & 0 & 0 \\ 1 & 0 & 0 \end{pmatrix}, & \lambda_5 &= \begin{pmatrix} 0 & 0 & -i \\ 0 & 0 & 0 \\ i & 0 & 0 \end{pmatrix}, & \lambda_6 &= \begin{pmatrix} 0 & 0 & 0 \\ 0 & 0 & 1 \\ 0 & 1 & 0 \end{pmatrix}, \\ \lambda_7 &= \begin{pmatrix} 0 & 0 & 0 \\ 0 & 0 & -i \\ 0 & i & 0 \end{pmatrix}, & \lambda_8 &= \frac{1}{\sqrt{3}} \begin{pmatrix} 1 & 0 & 0 \\ 0 & 1 & 0 \\ 0 & 0 & -2 \end{pmatrix}. \end{aligned}$$

Each pure state therefore can be bijectively mapped to a point on S^7 , the seven-dimensional unit sphere embedded in \mathbb{R}^8 . For mixed states, we have

$$\rho = \frac{1}{3} (\text{id}_3 + \sqrt{3}c\mathbf{r} \cdot \boldsymbol{\lambda}),$$

where $c \leq \frac{\sqrt{3}}{2} \csc(\phi + \pi/3)$ for some $\phi \in [\pi/6, \pi/2]$. The value of ϕ can be computed from an invariant involving \mathbf{r} and a product \star based on the anticommutation relations of $SU(3)$ (Malles and Mukunda, 1997). More concretely, we define completely symmetric d -symbols by

$$\{\lambda_a, \lambda_b\} = \lambda_a \lambda_b + \lambda_b \lambda_a = \frac{4}{3} \delta_{ab} + 2d_{abc} \lambda_c$$

¹w.r.t. the Hilbert-Schmidt inner product $(\lambda_i, \lambda_j) = \text{tr}(\lambda_i^\dagger \lambda_j)$

where δ_{ab} is the Kronecker delta, and the product \star by

$$(\mathbf{r} \star \mathbf{r})_a = \sqrt{3}d_{abc}\mathbf{r}_b\mathbf{r}_c.$$

Then, $\mathbf{r} \cdot \mathbf{r} \star \mathbf{r} = -\sin(3\phi)$.

Leaving out the global phase, any pure three-level state can be written as

$$|\psi\rangle = e^{i\chi_1} \sin \beta_1 \cos \beta_2 |0\rangle + e^{i\chi_2} \sin \beta_1 \sin \beta_2 |1\rangle + \cos \beta_1 |2\rangle,$$

where $\chi_1 \in [0, 2\pi[$ is the phase of the ground state and $\chi_2 \in [0, 2\pi[$ the phase of the first excited state relative to the phase of the second excited state, and $\beta_1 \in [0, \pi/2[$, $\beta_2 \in [0, \pi/2[$ parameterize the populations. Therefore every state can be represented as a point in the product manifold of a torus $S \times S$ and an octant of the unit sphere S^2 . The phase of $|0\rangle$ with respect to $|2\rangle$ is well-defined except for the case where $\beta_2 = \pi/2$ (and therefore χ_1 is undefined). The phase of $|1\rangle$ with respect to $|2\rangle$ is well-defined except for the case where $\beta_2 = 0$ (and therefore χ_2 is undefined). The local parametrization forms a subset of S^7 and includes all pure three-level states, with the exception of the points with vanishing third component (i.e. $\beta_1 = \pi/2$). When considering only these omitted states, the Bloch sphere is recovered.

Note that, as opposed to the two-level case where mixed states correspond to points lying within the Bloch sphere, the mixed states of a three-level system are not the points within the torus and the octant, but the set of points $\{\mathbf{r} \in \mathbb{R}^8; \mathbf{r} \cdot \mathbf{r} = 1, \mathbf{r} \star \mathbf{r} = \mathbf{r}\} \subset S^7$ (Arvind et al., 1997; Khanna et al., 1997).

1.2 Geometric phases

The state of a quantum system acquires a phase as the system evolves in time. When the Hamiltonian H governing the evolution is time-independent, for an eigenstate of H this phase is simply the dynamic phase, that is, up to constants, the time-integral of the energy of the system. When the Hamiltonian is time-dependent, there can also be a geometric phase in addition to the dynamic phase. It constitutes a ‘‘memory’’ of the evolution the system has undergone’ (Anandan, 1992). It is independent of both the energy of the eigenstate and the rate of the evolution; what matters is only the sequence of quantum states the system has traversed (Anandan, 1992).

When final $|\psi'\rangle$ and initial state $|\psi\rangle$ are related via $|\psi'\rangle = e^{i\gamma}|\psi\rangle$, the evolution is said to be *cyclic*. Since $|\psi\rangle$ and $|\psi'\rangle$ only differ by a phase factor, they lie in the same ray of the Hilbert space \mathcal{H} (see Fig. 1.2(a)) and are classically indistinguishable. The curve C traced out by $|\psi(t)\rangle$ in the Hilbert space is open (meaning the states have a different phase), while the curve \hat{C} in the projective Hilbert space \mathcal{P} is closed.

1.2.1 The Berry phase

If the evolution of the Hamiltonian H is not only cyclic but also *adiabatic*², by virtue of Ehrenfest’s adiabatic theorem³ an eigenstate at $t = 0$ evolves into an eigenstate at $t = T$.

²Here: slow with respect to the energy scales involved.

³See, for example, Messiah (1991).

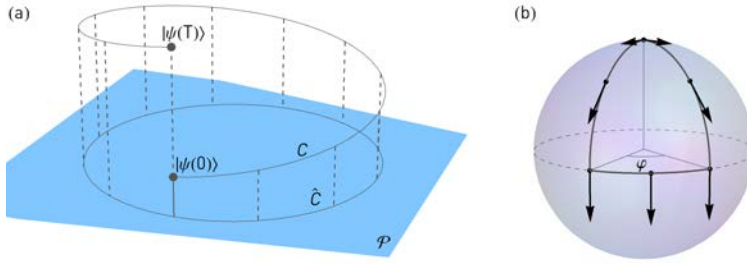


Figure 1.2: (a) After a cyclic and adiabatic evolution of the Hamiltonian, the state vectors $|\psi(0)\rangle$ and $|\psi(T)\rangle$ lie in the same ray of the Hilbert space, but their phase can be different. (b) Example of parallel transport on a sphere, in which a vector transported along a closed path returns to its original position rotated.

What about the phase at time T ? In addition to the usual dynamic part, there is a geometric contribution which is called the Berry phase (Berry, 1984). The brief derivation which follows is based on Nakahara (2003).

Let λ denote the parameters on which the Hamiltonian H depends, and assume that these change adiabatically over time, $\lambda = \lambda(t)$. The Schrödinger equation

$$H(\lambda(t))|\psi(t)\rangle = i\hbar \frac{d}{dt}|\psi(t)\rangle. \quad (1.6)$$

describes the time evolution of the state $|\psi\rangle$ in time. How does the n th normalized eigenstate, $|\psi(0)\rangle = |n, \lambda(0)\rangle$, where

$$H(\lambda(0))|n, \lambda(0)\rangle = E_n(\lambda(0))|n, \lambda(0)\rangle,$$

evolve in time, assuming the eigenvalues are not degenerate? Inserting the ansatz

$$|\psi(t)\rangle = \exp\{i\gamma(t) - i\delta\}|n, \lambda(t)\rangle$$

with the dynamic phase $\delta = \int_0^t dt' E_n(\lambda(t'))/\hbar$ into eq. (1.6) gives

$$\dot{\gamma}(t) = i\langle n, \lambda(t) | \frac{d}{dt} |n, \lambda(t)\rangle.$$

Integrating from $t = 0$ to $t = T$ leads us to the Berry phase of the n th eigenstate

$$\gamma = i \int_{\lambda(0)}^{\lambda(T)} d\lambda \langle n, \lambda(t) | \nabla_{\lambda} |n, \lambda(t)\rangle. \quad (1.7)$$

If the integrand in eq. (1.7) is not a total derivative, γ may be nonzero. From the normalization of the state, $\frac{d}{dt}(\langle n, \lambda(t) | n, \lambda(t)\rangle) = 0$, it follows that γ is real. Its invariance under local gauge transformations $|n, \lambda(t)\rangle \mapsto e^{i\alpha(t)}|n, \lambda(t)\rangle$ follows from eq. (1.7) because non-degenerate eigenvalues can only differ by a phase which is an integer multiple of 2π . The invariance of eq. (1.7) under reparametrization of the integral implies that γ is independent of the rate of traversal of the path $C = \lambda([0, T])$.

Defining the Berry connection $\mathbf{A} = i\langle n, \boldsymbol{\lambda}(t) | \nabla_{\boldsymbol{\lambda}} | n, \boldsymbol{\lambda}(t) \rangle$ (Berry, 1984), eq. (1.7) can be rewritten as

$$\gamma = \int_{\boldsymbol{\lambda}(0)}^{\boldsymbol{\lambda}(T)} d\boldsymbol{\lambda} \cdot \mathbf{A} = \oint_C d\boldsymbol{\lambda} \cdot \mathbf{A}. \quad (1.8)$$

The Berry phase is thus the integral of the Berry connection along the path C .

The archetypal geometric phase (which happens to be relevant for this thesis) is the Berry phase of a spin one-half particle with spin $\boldsymbol{\sigma} = (X, Y, Z)$ in a magnetic field \mathbf{B} , a situation described by the Hamiltonian

$$H = \hbar \boldsymbol{\sigma} \cdot \mathbf{B}/2 \quad (1.9)$$

where \mathbf{B} is in units of angular frequency. The parameters upon which H depends are $\boldsymbol{\lambda}(t) = \mathbf{B}(t)$, and the parameter space is the three-dimensional space describing the magnetic field \mathbf{B} . This field is changed over time, slowly and cyclically, to trace out a loop C . Then, as derived in Berry (1984), the geometric phase acquired by the spin one-half is simply

$$\gamma = \pm \alpha(C)/2, \quad (1.10)$$

where α is the solid angle enclosed by the path C in parameter space, as seen from the origin. This illustrates why this phase is called geometric phase: only the solid angle subtended by C matters. Neither the shape of the contour, nor the speed of traversal play a role.

1.2.2 Berry phase & parallel transport

In a plane, parallel transporting a vector along a curve simply amounts to moving the vector along the curve while preserving its magnitude and direction. A vector \mathbf{v}_f parallel-transported along closed loop is identical to the initial vector \mathbf{v}_i . On a curved surface, in every infinitesimal step of the parallel transport, the following should be kept constant: (i) the length of the vector, (ii) its direction, and (iii) the angle between the vector and the surface normal. Still, interesting things can happen. In Berry's words,

[t]ake a pencil, lay it on the north pole of a globe and point it in the direction of any of the meridians [...]. Move the pencil down along the line to the equator and, keeping it perpendicular to the equator, slide it to another line of longitude. Move the pencil back to the north pole along the new meridian, and you will find that although the pencil has been returned to its starting point and at no time was rotated, it no longer points along the original line of longitude. M.V. Berry (1988)

In this example, the globe represents the curved space, namely a sphere, and the pencil represents the vector (see Fig. 1.2(b)). The vector is rotated by an angle α equal to the solid angle enclosed by the curve. For instance, if the angle between the meridians is $\phi = \pi/4$, the subtended solid angle is $\pi/2$ and so is α .

1.2.3 Generalizations of the Berry phase

For a quantum system to acquire a Berry phase, three conditions must be fulfilled: (i) λ should be modified adiabatically so that (ii) it traces out a closed curve C ; and (iii) the energy eigenstates must not be degenerate. Geometric phases appear in a more general settings, when one or more of these requirements are dispensed with.

Aharonov and Anandan (1987) and Nakagawa (1987) have independently demonstrated that the motion of the quantum system need not be adiabatic. As long as the evolution of the system itself is cyclic, an identical phase factor can be associated with all curves C in the Hilbert space \mathcal{H} which project to the same closed curve \hat{C} in the projective Hilbert space \mathcal{P} . Samuel and Bhandari (1988) have shown that the evolution need not be cyclic. Then, C is open, and the geometric phase is given by the surface inside the projection \hat{C} of C closed by the shortest geodesic curve between the projected initial and final states. For a less formal interpretation, the reader may refer to Aitchison and Wanelik (1992), or to García de Polavieja and Sjöqvist (1998) for worked examples. Both generalizations, the one by Aharonov and Anandan (1987) as well as the one Samuel and Bhandari (1988), are based on the work by Pancharatnam (1956).

As seen in above in sec. 1.2.1, when the energy eigenstate of the Hamiltonian is non-degenerate, a cyclic and adiabatic evolution will map a state back to itself, times a phase factor,

$$|\psi(T)\rangle = \exp\left\{-\frac{i}{\hbar} \int_0^T E(t) dt\right\} \exp(i\gamma) |\psi(0)\rangle. \quad (1.11)$$

When the eigenstates are degenerate, this is not necessarily true. The generalization of the Berry phase for this case has first been studied by Wilczek and Zee (1984). If the N degenerate levels do not cross other levels during the evolution, a degenerate state will be mapped to the subspace of the degenerate levels. The phase it acquires is not a complex number $\gamma \in U(1)$, but a matrix $U_{\alpha\beta} \in U(N)$:

$$|\psi_\alpha(T)\rangle = \sum_{\beta=1}^N \exp\left\{-\frac{i}{\hbar} \int_0^T E(t) dt\right\} U_{\alpha\beta} |\psi_\beta(0)\rangle. \quad (1.12)$$

The non-adiabatic generalization of this case has been treated by Anandan (1988).

Further generalizations exist. Geometric phases for mixed states were introduced by Uhlmann (1986) and an alternative formulation was provided by Sjöqvist et al. (2000). The off-diagonal geometric phases by Manini and Pistoiesi (2000) and the generalization by Filipp and Sjöqvist (2003) treat the case where initial and final state are orthogonal and the usual definition of the geometric phase is not applicable. Simon (1983) has worked out the connection between the Berry phase and differential geometry. Customarily, authors work in the Schrödinger picture, but Kuratsuji and Iida (1985) discuss the Berry phase in the path-integral formalism.

To conclude this section, a few works of reference on geometric phases: Anandan (1992) has written a short review on geometric phases. Berry has written popular articles on the geometric phase itself (Berry, 1988) and its heralds (Berry, 1990). A collection of ground-breaking papers (both theoretical and experimental) on quantal geometric phases can be found in Wilczek and Shapere (1989). The books by Bohm et al. (2003), and Chruscinski and Jamiolkowski (2004) provide the eager reader with a mathematically

rigorous exposition to the topic. The monographs by Pachos (2012) and Nakahara (2003) are broader in scope; Pachos addresses topological quantum computation in general but provides a neat, not too technical introduction to geometric phases and their applications. Nakahara is more formal and gives a compendium of geometrical and topological concepts in physics. The first pages of Resta's (2000) review start off with the Pancharatnam phase (the 'discrete' or 'projective' version of the Berry phase) and illustrate the connection between the Aharonov-Bohm effect and the Berry phase. Quantum mechanics textbooks usually shun geometric phases. The newer editions of the texts by Bohm (1993) and Sakurai (1994) are exceptions.

1.2.4 Experimental observations of geometric phases

The Berry phase was first observed for a spin one particle in photons in an optical fibre (Tomita and Chiao, 1986) and for a spin one-half particle using spin-polarized neutrons (Bitter and Dubbers, 1987). Suter et al. (1988) have observed the non-adiabatic but cyclic geometric phase in a system of two proton spins coupled by magnetic dipolar interactions using NMR interferometry. The non-cyclic geometric phase was measured in spin-polarized neutron experiments (Weinfurter and Badurek, 1990; Wagh et al., 1998)⁴.

Other systems where the Berry phase was measured include: in solid state, a CPB qubit (Leek et al., 2007) and a superconducting charge pump (Möttönen et al., 2008); graphene (Zhang et al., 2005); in optics, optical fibres (Tomita and Chiao, 1986), laser interferometry (Bhandari and Samuel, 1988), and single optical photons (Kwiat and Chiao, 1991); neutrons (Bitter and Dubbers, 1987; Richardson et al., 1988); and NMR (Suter et al., 1987). The anomalous Hall effect in frustrated ferromagnets can be explained in terms of Berry phases acquired by electrons hopping between atoms (Taguchi et al., 2001).

Tycko (1987) has measured the non-Abelian but cyclic and adiabatic geometric phase using spin 3/2 chlorine nuclei in a crystal of sodium chlorate. The full non-Abelian gauge structure was revealed in an experiment by Zwanziger et al. (1990). The demonstration that the phase factors acquired by a degenerate state along two different closed paths do not commute has been achieved by Abdumalikov et al. (2013) in a circuit QED experiment. As of winter 2014, no experimental measurement of non-cyclic non-Abelian geometric phases has been carried out.

For the convenience of the reader, the first theoretical and experimental explorations of the various types of geometric phases have been assembled in table form in Fig. 1.3.

1.2.5 Geometric quantum computation

Using geometric phases to perform circuit-based quantum computation is known as geometric quantum computation (Sjöqvist, 2008). The theoretical groundwork carried out by Zanardi and Rasetti (1999) shows that adiabatic loops in control parameters of a suitable Hamiltonian can be used to perform universal quantum computing. The first experimental geometric quantum computation (more specifically, a controlled phase-shift gate) was implemented by Jones et al. (2000). Universal single qubit operations based on non-Abelian phase factors arising in adiabatic evolution have been observed by Toyoda et al.

⁴According to Wagh et al. (1998), Weinfurter and Badurek (1990) have not measured the noncyclic geometric phase, but rather the amount of precession of the neutron spin. Sjöqvist (2001) concurs.

	cyclic	non-cyclic
adiabatic	Berry (1984) <i>Tomita & Chiao (1986)</i> Wilczek & Zee (1984) <i>Tycko (1987)</i>	Bhandari & Samuel (1988) <i>Wagh et al. (1998)</i> Mostafazadeh (1999) <i>n/a</i>
non-adiabatic	Anandan (1988) <i>Abdumalikov et al. (2013)</i> Aharonov & Anandan (1987) <i>Suter et al. (1988)</i>	<i>n/a</i> <i>n/a</i> non-Abelian Abelian Bhandari & Samuel (1988) <i>n/a</i>

Figure 1.3: Overview of the first theoretical discussion (in roman letters) and the first experimental realizations (in italics) of a variety of geometric phases. Mixed-state geometric phases, off-diagonal geometric phases, and geometric phases in open quantum systems are not represented.

(2013) in a trapped single Ca^+ ion. The authors have also demonstrated robustness against parameter variations.

A drawback of adiabatic gates is the long duration of the evolution. Non-adiabatic geometric quantum computation is a faster alternative. Sjöqvist et al. (2012) have proposed one- and two-qubit gates for universal quantum computation using a Λ -system. The one-qubit gates have been experimentally realized by Abdumalikov et al. (2013) in a circuit QED setup. Zu et al. (2014) claim to have implemented a two-qubit gate using nitrogen-vacancy centres in diamond.

1.3 Circuit quantum electrodynamics

1.3.1 Introduction

Cavity quantum electrodynamics (cavity QED), the study of coherent interactions between matter and light, can be traced back to the 1940s (Dutra, 2005; Haroche and Raimond, 2006). The fundamental idea is to increase the interaction strength between the electromagnetic field and the atoms by confining the field in a cavity and having atoms flying through the cavity. Strong coupling came about in the nineties, with the observation of vacuum Rabi splitting (Thompson et al., 1992) and vacuum Rabi oscillations (Brune et al., 1996).

Blais et al. (2004) have proposed the circuit QED architecture, a variant of cavity QED which makes use of a one-dimensional coplanar waveguide resonator (CPW resonator) coupled to superconducting electrical circuits acting as artificial atoms, instead of the usual three-dimensional cavity with transiting atoms. In circuit QED, the ‘atoms’ stay in

place, and the confined geometry enhances their coupling to the electromagnetic field. Wallraff et al. (2004) have carried out a pioneering experiment in which a single photon is coherently coupled to a single artificial atom. At the same time, Chiorescu et al. (2004) observed Rabi oscillations between a superconducting flux qubit coupled to a capacitively shunted SQUID which acts as a harmonic oscillator.

This section gives a brief introduction to circuit QED. For a more thorough treatment, see e.g. the thesis by Baur (2012).

1.3.2 Superconducting qubits

In a superconductor, the Cooper pairs form a condensate described by a single wave function with two variables, phase and density. Two superconducting electrodes brought together but separated by a thin insulating oxide layer through which Cooper pairs can tunnel form a Josephson junction (Tinkham, 1996). It is fully described in terms of the difference in phase and in Cooper pair number of the condensates on either side (Feynman et al., 1971). The junction has a capacity C_J and a Josephson energy $E_J = I_c \hbar / (2e)$, where I_c is the critical current of the junction.

Superconducting qubits (Clarke and Wilhelm, 2008; Devoret and Schoelkopf, 2013) rely on Josephson junctions. The field took off with the observation of the energy spectrum of a *coherent superposition* of two charge states (Nakamura et al., 1997). In the following years, various types of superconducting qubits have been developed, encoding quantum states in the charge, phase or flux degree of freedom.

1.3.3 Transmon qubit

The transmon qubit is a kind of charge qubit (Makhlin et al., 2001). In its simplest form, the charge qubit (also known as Cooper pair box qubit) consists of a superconducting electrode ('island') sandwiched in between a Josephson junction connected to an other electrode ('reservoir') and a capacitance to ground (C_g , 'gate', see Fig. 1.4(a) for a circuit diagram). Usually, to form a qubit a gate voltage V_g is applied to produce two nearly degenerate charge states (i.e., with almost the same number of Cooper pairs). The degeneracy is lifted due to the Josephson energy.

Replacing the Josephson junction by a SQUID (superconducting quantum interference device, a superconducting loop containing two Josephson junctions in parallel) results in the split Cooper pair box (Fig. 1.4(b)). It behaves like a Cooper pair box whose Josephson energy $E_J(\Phi) = E_{J,\max} |\cos(\pi\Phi/\Phi_0)|$ depends on the magnetic flux Φ flowing through the SQUID-loop. $\Phi_0 = h/(2e)$ is the magnetic flux quantum.

When the effective offset charge⁵ $n_g = C_g V_g / (2e)$ is set to 1/2 (in units of Cooper pairs $2e$), the qubit transition frequency is insensitive to charge noise to first order. At this optimal working point ('sweet spot'), coherence times are much improved (Vion et al., 2002). However, jumps and drifts in the offset charge induced by the environment (charge noise) will affect the qubit transition frequency and induce decoherence.

The transmission-line shunted plasma oscillation qubit, usually abbreviated to transmon, is a variation on the charge qubit (Koch et al., 2007). Its most distinguishing characteristic is a large shunting capacitor with capacitance C_B between island and reservoir which reduces its sensitivity to charge noise (see Fig. 1.4(c)).

⁵It is sometimes also called gate charge.

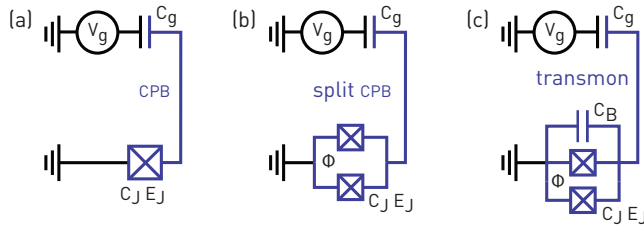


Figure 1.4: Electric circuit diagrams of (a) a Cooper pair box, (b) a split Cooper pair box, and (c) a transmon.

Transmon Hamiltonian

The Hamiltonian of the transmon can be cast in a form identical to the one describing a Cooper pair box,

$$H = 4E_C(n - n_g)^2 - E_J \cos\phi, \quad (1.13)$$

with the operator n of the difference in the number of Cooper pairs across island and reservoir, and the operator ϕ of the difference in phase. $E_C = e^2/(2C_\Sigma)$, the charging (or electrostatic) energy, describes how much energy an electron needs to tunnel across the junction with total capacitance $C_\Sigma = C_J + C_B + C_g$, the sum of the capacitances of the Josephson junction C_J , the shunting capacitor C_B and the gate capacitor C_g . Unlike the Cooper pair box qubit, a transmon has a large ratio E_J/E_C . The Mathieu functions solve the transmon Hamiltonian eq. (1.13) in the phase basis exactly. In Fig. 1.5(a-c), the three lowest lying energy eigenvalues E_m , $m = 0, 1, 2$ of eq. (1.13) are shown for different ratios E_J/E_C , low and high values corresponding to the Cooper pair box and the transmon, respectively.

Anharmonicity

By luck of by foreordination, increasing the ratio E_J/E_C causes an exponential decrease in the charge dispersion (the variation of the transition frequencies as a function of gate charge), but only an algebraic reduction in the anharmonicity⁶ (the energy difference α between the two lowest-energy transitions E_{01} and $E_{12} = E_{01} + \alpha$). Even though the energy level structure of the transmon is only weakly anharmonic, transitions can be addressed individually in relatively short times (~ 8 ns), which is crucial for utilizing it as a qubit. Nonetheless care must be taken to avoid unwanted leakage into other energy levels, and to include sufficiently many energy levels in models of the system. (See e.g. Fink et al. (2008), Chow et al. (2009), Motzoi et al. (2009) and ch. 3 of this thesis; or Steffen et al. (2003) for a discussion in the context of phase qubits.)

For the Cooper pair box operated at $n_g = 0.5$, the anharmonicity $\alpha = E_{12} - E_{01}$ is positive: the level spacing increases with energy. For large ratios E_J/E_C , that is, when going to the transmon regime, α is negative: the level spacing decreases with energy. Asymptotically, $\alpha = -E_C$ (see Fig. 1.5(d)). In practice, E_J/E_C is typically about 60 and $\alpha \approx -1.2E_C$.

⁶The anharmonicity is actually due to the cosine potential in the Hamiltonian eq. (1.13).

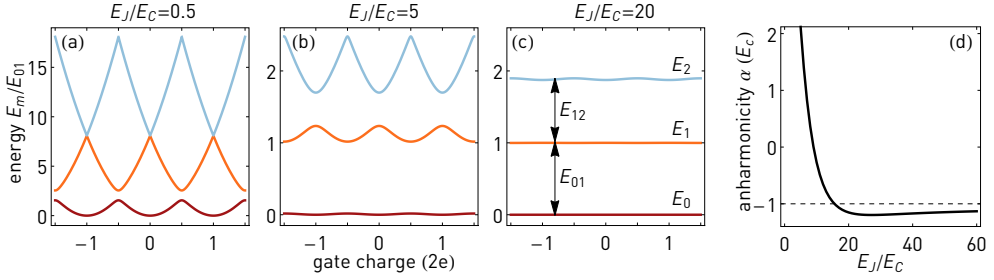


Figure 1.5: (a-c) Energy eigenvalues E_m for $m = 0, 1, 2$ as a function of gate charge. The transition energies are normalized to E_{01} at charge degeneracy $n_g = 0.5$. (d) Anharmonicity normalized to E_C as a function of the ratio E_J/E_C . The dashed line indicates the limit $\alpha = -E_C$ attained for large ratios E_J/E_C .

Approximate energy levels

When E_J/E_C is large, perturbation theory applied to eq. (1.13) gives the approximations $E_{0,m} = m\sqrt{8E_J E_C} - \frac{(m+1)m}{2}E_C$, $m = 1, 2, 3, \dots$ and $E_{m-1,m} = \sqrt{8E_J E_C} - mE_C$, $m = 1, 2, 3, \dots$, with the useful special cases

$$E_{01} \approx \sqrt{8E_J E_C} - E_C, \quad E_{12} \approx \sqrt{8E_J E_C} - 2E_C. \quad (1.14)$$

The transmon is usually realized as a split transmon, that is, it comprises a SQUID instead of a single Josephson junction. Then, its transition energies are flux-tunable because $E_J = E_{J,\max} |\cos(\pi\Phi/\Phi_0)|$; they are periodic with a period of one flux quantum Φ_0 and maximal when the flux Φ is a half-integer. The formulas eq. (1.14) break down if the Josephson energy is flux-tuned to low values and $E_J/E_C \gg 1$ no longer holds.

1.3.4 Coplanar waveguide resonators

The coplanar waveguide resonator is a planar structure consisting of a centre conducting strip separated from the ground planes on either side by narrow gaps (Wen, 1969; Simons, 2001; Pozar, 2012). A sketch of a CPW resonator is shown in Fig. 1.6(a). It can thus be viewed as a longitudinal section of a coaxial cable. Its geometry is set by the width w of the centre strip and the separation s between centre strip and ground planes (see Fig. 1.6(b)). The article by Göppl et al. (2008) gives extensive information about CPW resonators in the context of circuit QED.

Since the wavelength of the microwave radiation it supports are comparable with the dimensions of the CPW resonator itself, transmission line theory is used to describe it—voltage and current vary along the CPW resonator. Nevertheless, the equivalent lumped circuit representation allows to model it using circuit theory (Pozar, 2012), which is convenient for quantizing the resonator (Devoret, 1997).

A coplanar waveguide can support two modes, an even mode (which is a quasi-TEM mode) and an odd mode (or slot mode) which also has field components in longitudinal direction (Wolff, 2006). We suppress the odd mode by keeping both ground panes on the same potential via bonding wires or airbridges (Steffen, 2013).

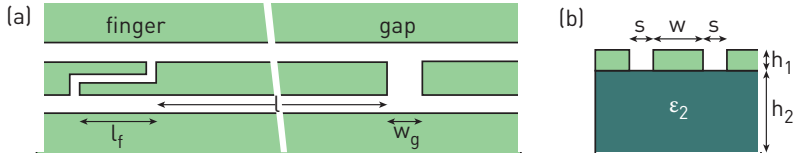


Figure 1.6: (a) Top view of a CPW resonator with ground planes (top and bottom) and centre strip with finger and gap capacitors. (b) Vertical section of the CPW. The two ground planes separated by the centre conductor (light green) lie on top the dielectric plane (dark green).

Design

The centre strip conductor (of length l) is coupled to transmission lines by capacitors with different geometries. In terms of capacitance C_l and inductance L_l of the transmission line per unit length, its impedance $Z_0 = \sqrt{L_l/C_l}$ is a function of the ratio $s/(s+2w)$, which allows to connect it e.g. to a printed circuit board (PCB) without impedance mismatches by adapting its dimensions continuously (Simons, 2001). For a dielectric and non-magnetic substrate, L_l depends only on the geometry of the CPW resonator (Simons, 2001)⁷. C_l is a function both the geometry and the effective permittivity ϵ_{eff} of the CPW resonator. An analytical expression for the quantity ϵ_{eff} exists (Gevorgian et al., 1995), but typically, C_l is determined in a finite element electromagnetic simulation, from which ϵ_{eff} can be computed.

Here, the CPW resonator is patterned in a niobium film of thickness $h_2 = 200$ nm and has dimensions $w = 10$ μm , $s = 4.5$ μm . The substrate is a sapphire (Al_2O_3) wafer of thickness $h_1 = 430$ μm and permittivity $\epsilon_{\parallel} = 11.1$ along the optical axis and $\epsilon_{\perp} = 8.9$ perpendicular to it (Harman et al., 1994). The sapphire being cut perpendicularly to the optical axis, in calculations of ϵ_{eff} the value $\sqrt{\epsilon_{\parallel}\epsilon_{\perp}}$ should be used (Collin, 2000, ch. 3). From this, $C_l \approx 10^{-10}$ F/m, $\epsilon_{\text{eff}} \approx 6$, $L_l \approx 10^{-7}$ H/m and an impedance $Z_0 \approx 50\Omega$ are obtained⁸.

Resonance frequency

The frequency of the fundamental mode of the resonator is

$$v_0 = \frac{c}{\sqrt{\epsilon_{\text{eff}}}} \frac{1}{2l}, \quad (1.15)$$

with c the speed of light in vacuum, and the harmonics are at $v_{n-1} = n f_0$.

Coupling

Here, we consider input and output lines which are symmetrically coupled to the CPW resonator with a capacitance C_K . Asymmetric coupling is treated in Steffen (2013).

The coupling capacitance depends on the geometry of the coupling (such as the gap width w_g , the finger length l_f) and is calculated with finite element simulations. The

⁷The impedance of a superconductor is the sum of the temperature-independent geometric inductance and the temperature-dependent kinetic inductance. Here however, the kinetic inductance is small and can be neglected (Göppl et al., 2008).

⁸The other components in the setup have an impedance of 50Ω , but the resonator could in principle have any impedance. However, making it 50Ω allows us to reuse the designs for transmission line experiments (van Loo et al., 2013) without causing impedance mismatches.

loaded quality factor $Q_L = \nu_0/\delta\nu$ and the resonance frequency ν_0 are obtained by fitting a Lorentzian with transmission peak power P_r and full width half maximum $\delta\nu$

$$P(\nu) = P_r \frac{1}{1 + \left(\frac{\nu - \nu_0}{\delta\nu/2}\right)^2}$$

to the transmission spectrum of the resonator (Göppl et al., 2008). The loaded quality factor is connected to the decay rate κ through

$$\kappa/(2\pi) = \nu_0/Q_L = \delta\nu$$

and obeys the relation

$$1/Q_L = 1/Q_{\text{int}} + 1/Q_{\text{ext}},$$

with internal Q_{int} and external Q_{ext} quality factors. Equivalently in terms of decay rates, we have

$$\kappa_L = \kappa_{\text{int}} + \kappa_{\text{ext}}.$$

The external decay rate κ_{ext} goes with the square of the coupling capacitance, $\kappa_{\text{ext}} \propto C_{\kappa}^2$, and is thus chosen by design. The internal decay rate κ_{int} is probably limited by dielectric losses arising at the metal surface. Radiation losses and resistive losses are thought to be negligible in a superconducting CPW resonator (Göppl et al., 2008).

In the undercoupled regime $\kappa_{\text{ext}} \ll \kappa_{\text{int}}$, the main contribution to the loaded decay rate stems from the intrinsic losses of the resonator. Measurements of the internal decay rate excepted, all experiments are conducted in the overcoupled regime $\kappa_{\text{ext}} \gg \kappa_{\text{int}}$, where the loaded decay rate is dominated by the external decay rate and therefore $\kappa_L \propto C_{\kappa}^2$. The coupling of a resonator is an important design parameter of a circuit QED experiment, since keeping κ_L small makes for a long-lived resonator, but extracting information about it is time-consuming.

In typical experiments the loaded quality factor is a few thousand, and the internal quality factor a few hundred thousand. Quality factors exceeding 10^6 have been achieved (Megrant et al., 2012). The coupling capacitance lies in a range from 0.1 fF to 20 fF, with fingers of length $l_f = 100 \mu\text{m}$ and gaps of width w_g from $1 \mu\text{m}$ to $30 \mu\text{m}$ (Steffen, 2013).

1.3.5 Transmon coupled to a resonator

The prototypical circuit QED experiment consists of a transmon coupled to a resonator. Here, a CPW resonator is considered. Alternatively, three-dimensional cavity resonators can be used (Paik et al., 2011).

Jaynes-Cummings-Hamiltonian

The interaction between a M -level atom and a quantized field is described by the generalized Jaynes-Cummings-Hamiltonian (Jaynes and Cummings, 1963; Koch et al., 2007)

$$H/\hbar = \omega_r \left(a^\dagger a + \frac{1}{2} \right) + \sum_{j=0}^{M-1} \omega_j |j\rangle\langle j| + \sum_{i,j=0}^{M-1} g_{i,j} |i\rangle\langle j| \left(a^\dagger + a \right). \quad (1.16)$$

The first term in eq. (1.16) describes the quantized field as a harmonic oscillator with resonator frequency ω_r , photon creation operator a^\dagger and photon annihilation operator a .

The second term describes the bare transmon with states $|i\rangle$ of energy $\omega_i = E_i/\hbar$ in units of \hbar . The third term couples the transmon to the cavity field.

The coupling term in eq. (1.16) can be simplified (Koch et al., 2007) by dropping couplings $g_{i,j}$ with $|i-j| > 1$ (which are either zero or small for a transmon) and applying the rotating wave approximation (which amounts to ignoring the terms describing simultaneous creation or annihilation of an excitation in both the resonator and the atom). Then,

$$H/\hbar = \omega_r \left(a^\dagger a + \frac{1}{2} \right) + \sum_{j=0}^{M-1} \omega_j |j\rangle \langle j| + \sum_{j=0}^{M-2} g_{j,j+1} \left(|j\rangle \langle j+1| a^\dagger + \text{h.c.} \right), \quad (1.17)$$

with coupling strengths

$$g_{j,j+1} = 2\beta e V_{\text{rms}} \langle j|n|j+1\rangle \approx 2\beta e V_{\text{rms}} \sqrt{\frac{j+1}{2}} \left(\frac{E_J}{8E_C} \right)^{1/4}. \quad (1.18)$$

The capacitance ratio $\beta = C_g/C_\Sigma$ describes what part of the voltage in the resonator is seen by the transmon. The root-mean-square voltage $V_{\text{rms}} = \sqrt{\hbar\omega_r/2C_r}$ (with the effective capacitance of the resonator $C_r = C_l/2$) arises from equating the electrostatic energy of the resonator with its zero-point energy:

$$C_r V_{\text{rms}}^2 = \hbar\omega_r/2.$$

Thus, the coupling strength scales with the root of the resonator mode number (see eq. (1.15)) and the root of the excitation level.

Strong coupling regime

The strong coupling regime is achieved when the relaxation and decoherence rates of both the transmon and the photon field in the resonator are much smaller than their mutual coupling. The states of the resonator and the transmon hybridize when on resonance, leading to vacuum Rabi mode splitting (Wallraff et al., 2004; Fink et al., 2008), and vacuum Rabi oscillations (Johansson et al., 2006; Mlynek et al., 2012), where excitations are swapped repeatedly between them. For more details on this topic, see e.g. Fink (2010).

Dispersive limit

The dispersive limit is attained when (Boissonneault et al., 2010)

$$\langle a^\dagger a \rangle \ll \Delta_i^2 / (4g_i^2), \quad (1.19)$$

in other words, when the mean photon number is much lower than the critical photon number $n_{\text{crit}} = \Delta_i^2 / (4g_i^2)$, where $\Delta_i = (\omega_{i+1} - \omega_i) - \omega_r$ are detunings between the i th transition and the resonance frequency of the resonator. Pictorially, in the dispersive regime, there is little photonic part ($\propto g_i/\Delta_i$) in the transmon states (Blais et al., 2004, eqs. (2)-(6)), and save for some frequency shifts, the resonator and the transmon are decoupled.

In this limit, the Hamiltonian eq. (1.17) can be developed in the small parameter $\lambda_i = g_i/\Delta_i$. To third order, one obtains (Boissonneault et al. (2010), see also Bianchetti et al. (2010))

$$H/\hbar = \omega_r a^\dagger a + \sum_{i=0}^{M-1} \left(\omega_i |i\rangle \langle i| + L_i |i\rangle \langle i| + S_i |i\rangle \langle i| a^\dagger a \right) \quad (1.20)$$

with Lamb-shift and AC-Stark coefficients

$$L_i \approx \chi_{i-1}, \quad S_i \approx \chi_{i-1} - \chi_i.$$

These are given in terms of the pull coefficients $\chi_i = g_i^2/\Delta_i$, letting $\chi_i = 0$ if $i \notin \{0, 1, \dots, M-2\}$. When expanding to fourth order in λ_i , self-Kerr terms $\propto |i\rangle\langle i|(a^\dagger a)^2$ appear in eq. (1.20). Although they become relevant for high-power readout of the transmon, they can safely be neglected here (Reed et al., 2010; Boissonneault et al., 2010).

For a two-level system ($M = 2$) eq. (1.20) simplifies to

$$H/\hbar = \omega_r a^\dagger a + \omega_0 |0\rangle\langle 0| + (\omega_1 + \chi_0) |1\rangle\langle 1| + (-\chi_0 |0\rangle\langle 0| + (\chi_0 - \chi_1) |1\rangle\langle 1|) a^\dagger a.$$

Regrouping the terms gives

$$H/\hbar = (\omega_r - \chi_0) a^\dagger a + \omega_0 |0\rangle\langle 0| + (\omega_1 + \chi_0) |1\rangle\langle 1| + (2\chi_0 - \chi_1) |1\rangle\langle 1| a^\dagger a. \quad (1.21)$$

We identify the quantity $\omega'_r = \omega_r - \chi_0$ as the renormalized resonator frequency—the frequency of the resonator when the transmon is in the ground state⁹. The Lamb-shifted transition frequency of the transmon is $\omega'_{01} = \omega_{01} + \chi_0$. The last term in eq. (1.21) describes the AC Stark shift: the transition frequency ω'_{01} is shifted by $2\chi_0 - \chi_1$ for every photon in the cavity. Or, equivalently, the resonator frequency ω'_r is shifted by $2\chi_0 - \chi_1$ when the transmon is in the excited state $|1\rangle$. This is the foundation of dispersive readout (Blais et al. (2004), see also sec. 2.5.1).

For three transmon levels ($M = 3$), eq. (1.20) leads to

$$\begin{aligned} H/\hbar = & (\omega_r - \chi_0) a^\dagger a + \omega_0 |0\rangle\langle 0| + (\omega_1 + \chi_0) |1\rangle\langle 1| + (\omega_2 + \chi_1) |2\rangle\langle 2| \\ & + ((2\chi_0 - \chi_1) |1\rangle\langle 1| + (\chi_0 + \chi_1 - \chi_2) |2\rangle\langle 2|) a^\dagger a. \end{aligned}$$

In addition to the terms in eq. (1.21), we find the Lamb-shifted $|0\rangle \leftrightarrow |2\rangle$ transition $\omega'_{02} = \omega_{02} + \chi_1$ of the transmon (and thus $\omega'_{12} = \omega_{12} + \chi_1 - \chi_0$), as well as the ac-Stark shift $\chi_0 + \chi_1 - \chi_2$ of the second excited state.

Since the renormalized quantities are experimentally more relevant than the bare ones, in the remainder of this document we *drop the prime* off the renormalized quantities, so that e.g. ω_r refers to the renormalized resonator frequency.

⁹Koch et al. (2007) use a different convention, $\omega'_r = \omega_r - \chi_1/2$. This frequency has no immediate physical interpretation, but it distributes the pull χ_1 equally on the states $|0\rangle$ and $|1\rangle$, so that $H/\hbar = \omega'_r a^\dagger a + (\omega'_{01} Z)/2 + \chi' Z a^\dagger a$, with renormalized quantities $\omega'_{01} = \omega_1 - \omega_0 + \chi_0$ and $\chi' = \chi_0 - \chi_1/2$.

EXPERIMENTAL ASPECTS

In this chapter, the fabrication of the quantum devices and the experimental setup (encompassing cryogenic as well as microwave aspects) are described.

2.1 Sample fabrication

The samples used in circuit QED experiments are fabricated in the FIRST cleanroom at ETH Zurich. Larger structures, for instance the CPW resonator, and gate lines, are fabricated in a positive-resist photolithography process (Steffen, 2013) on a commercially acquired niobium-coated sapphire wafer. The smaller structures, such as the transmon, are made by patterning their structure into a positive resist with electron-beam lithography and then evaporating aluminium. The double-angle shadow-evaporation is interrupted by a static oxidation to create an aluminium oxide layer serving as tunnel barrier in the Josephson junctions (Fink et al., 2010). The duration of the oxidation step determines the Josephson energy E_J of the junction: the longer the oxidation time, the larger the oxide layer, the smaller E_J . The size of the Josephson Junction ($\sim 100 \times 100$ nm) gives additional control over E_J . A measurement of the normal state resistance allows to infer E_J (Ambe- gaokar and Baratoff, 1963; Fink et al., 2010). For an optical image of a sample, refer to Fig. 2.2.

2.2 Cryogenic aspects

Typically, the circuit QED building blocks (transmon, resonator, paramp, etc.) have transition frequencies $\nu \sim 7$ GHz, corresponding to a temperature $T = h\nu/k_B \sim 340$ mK. When performing experiments, these structures are initialized in the ground state by cooling

them well below T . This is achieved by placing them in a dilution refrigerator and shielding off environmental radiation.

2.2.1 Cryostat

The sample is mounted on the base temperature plate of a ^3He - ^4He dilution refrigerator Triton 200 from Oxford Instruments. Simply put, four layers of shielding and evacuating the interior of the cryostat to 10^{-3} mbar at room temperature provide protection from thermal radiation and heat transfer through conduction, convection and thermal radiation. Two stages of a pulse tube cooler (from Cryomech) provide cooling to 40K respectively 4K. The ^3He - ^4He circuit brings the temperature on the base temperature plate down to about 20 mK at the innermost and coldest stage, the mixing chamber. The sample is thermally anchored to this stage. To shield it from stray radiation, it rests in a closed copper box (see sec. 2.2.3). All copper parts are made of oxygen-free high-conductivity copper which is well-suited for thermalization of the sample.

Since the transition frequency of the transmon depends on the magnetic flux enclosed by the SQUID loop, shielding from fluctuating magnetic fields is also required. This is achieved by encasing the sample holder in two shields made of cryoperm, an alloy with high permeability at low temperatures. A picture of the cryostat (all shields removed except for the cryoperm ones) and a schematic of the wiring of the cryostat is shown in Fig. 2.1.

2.2.2 Microwave wiring

The sample is controlled and read out with microwave signals. These are connected to the electronics outside the cryostat via coaxial cables with a diameter of 85 mil (2.2 mm). The materials of the inner conductor and of the outer conductor are a compromise between low loss and low thermal conductivity. Outside the cryostat and at the mixing chamber, tin-plated copper/copper cables (UT-85-TP¹, low loss and high thermal conductivity) are used. All other cables are made of stainless steel/stainless steel (UT-85-SS-SS, high loss and low thermal conductivity) to reduce the heat load to the cryostat.

There is one exception: In the output line where the measurement signal travels, low losses are paramount and different cables with low losses and low thermal conductivity are used. After the sample, the microwave signal is routed through to two circulators terminated at the third port by means of a 50 Ω termination, effectively acting as isolators. This is to avoid signal leaking back into the cavity due to impedance mismatches along the line and due to input voltage noise of the amplifiers in the output line. A NbTi cable, superconducting up to ≈ 7 K, brings the signal from the 20 mK-stage to the input port of a high-electron mobility transistor (HEMT) amplifier attached to the 4 K-stage of the cryostat. It typically provides a gain of 35 dB with a noise temperature of 4 K to 10 K. It is powered by a low-noise power supply (Bianchetti, 2010, app. A.5) A stainless steel/silver-plated copper weld cable (UT-85-SS) then connects the output of the HEMT amplifier to the room temperature stage.

In some recent experiments, before travelling to the HEMT amplifier the signal is pre-amplified at the 20 mK-stage using a parametric amplifier (Yurke and Buks, 2006;

¹The number indicates the diameter of the cable in mils. TP stands for tin-plated.

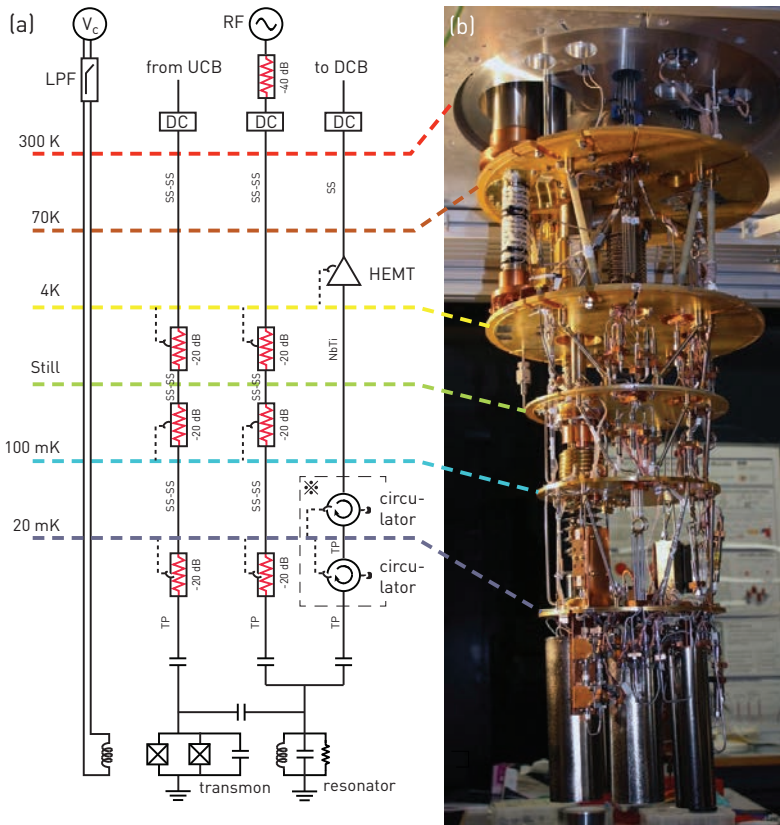


Figure 2.1: (a) Schematic of the cryostat wiring. The symbol \ast indicates what portion of the setup is modified when using a parametric amplifier (see sec. 2.5.2). (b) Photograph of the cryostat without shields.

Castellanos-Beltran and Lehnert, 2007; Yamamoto et al., 2008). These amplifiers have a smaller noise temperature and dissipate less power than HEMT amplifiers (see sec. 2.5.2 and ch. 5).

Further details, such as values of the attenuation per unit length of the coaxial cables can be found in sec. 4.3.3 of Fink et al. (2010). A discussion of the cryogenic heat flows can be found in app. A of Bianchetti et al. (2010).

Johnson noise (the dominant source of noise for temperatures above 100 mK, caused by the thermal motion of charge carriers) and thermal radiation should be suppressed in the microwave lines. 20 dB of attenuation along the microwave lines are sufficient to bring the thermal noise from room temperature down to 4 K. Between the 4 K-stage and the 20 mK-stage, an additional 40 dB of attenuation are installed to bring the thermal population in the sample down to about 0.05 photons in the cavity (Fink et al., 2010), respectively $\approx 2\%$ of population in the excited state of the transmon. To thermalize the inner conductor of the coaxial cable, we use attenuators which are normal conducting even at 20 mK and which connect the inner conductor and the outer conductor via a resistor. The attenua-

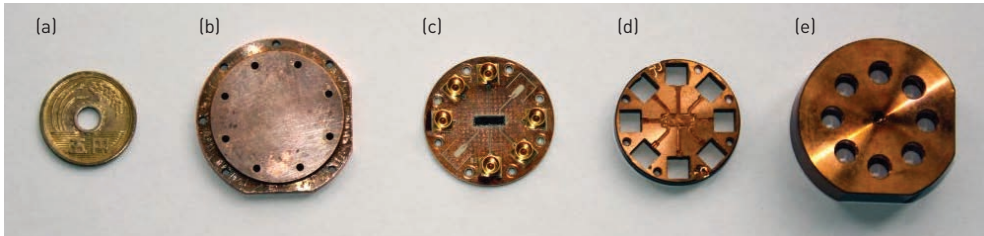


Figure 2.2: Sample and sample holder. (a) A ¥5 coin for size comparison. (b) Bottom of the sample holder. On its bottom side, there is a cutout (not visible here) in which the miniature coils are fitted. (c) The sample: PCB with soldered SMP connectors (golden) leading to the circuit QED chip (dark rectangle). (d) Sample cover with holes for the SMP connectors, and cutouts for the lines in the PCB and the sample. (e) Top of the sample holder with holes for the microwave cables.

tors are wrapped in unfluxed desoldering braid made of copper, a copper clamp is affixed to firmly hold the braid in place, and the braid is connected to a plate of the cryostat, thus creating thermal contact. A balance sheet of loss and gain along a typical microwave line can be found in sec. 3.1 of Bianchetti (2010).

2.2.3 Sample holder

The sample is mounted inside a copper box, which is fixed to a threaded rod of copper screwed to the mixing chamber plate. The bottom part of the box contains a cutout in its centre to accommodate up to three miniature superconducting coils (Bianchetti, 2010, sec. 3.5). These are used to create a static magnetic field for flux-biasing SQUID loops e.g. in a split transmon or a parametric amplifier. To avoid magnetic flux noise, they are battery-powered and filtered with low-pass RC filters with a cut-off frequency of about 10Hz (see Fig. 2.3(b)).

The sample itself (the sapphire chip with the microfabricated circuit) is glued and wire-bonded to a specially designed PCB. The PCB contains coplanar waveguides from the chip to PCB-mount SMP connectors which are soldered onto the PCB. The latter is screwed on the bottom part of the box, and closed off with a copper cover. The cover lies on the PCB but has cutouts for the chip and along the waveguides on the PCB. In absence of a cover, there are cavity modes in the space between sample and top of the box (Liu, 2012). The assembled parts (bottom, sample, cover) are connected with screws to the top of the box. The top of the box has holes through which microwave lines are connected. This connection is realized with SMP bullets placed in the PCB-mount SMP connectors.

2.3 Signal generation

As mentioned above, the microwave signals for controlling and reading out the qubit are created at room temperature and sent into the cryostat and to the sample through coaxial lines. To create microwave pulses with a square envelope, it is sufficient to use the pulse modulation option on an analogue signal generator (such as Agilent² E8257D).

²Agilent is now operating under the name Keysight.

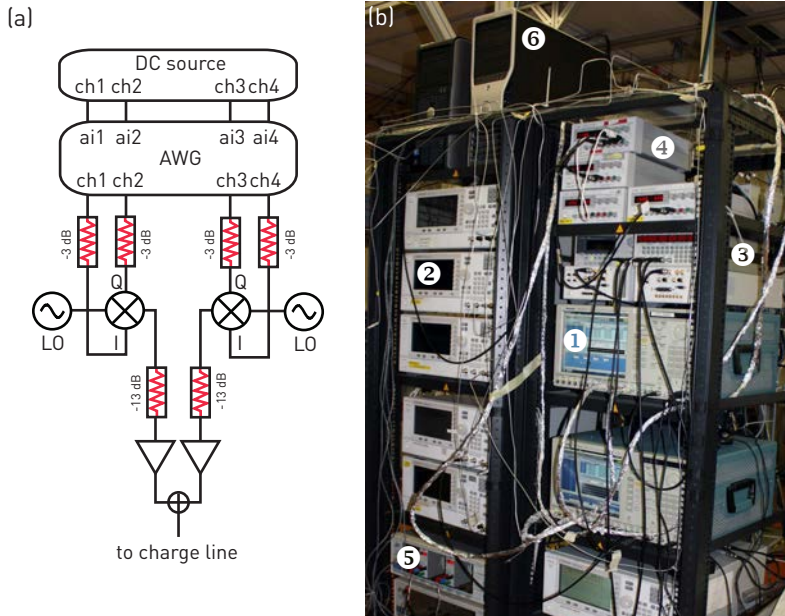


Figure 2.3: Signal generation and measurement setup. (a) Schematic of the upconversion setup. See text for details. (b) Photograph of the measurement racks. The equipment is (1) an AWG, (2) a microwave signal generator, (3) a digital delay generator, (4) DC power sources for the amplifiers in the measurement chain (5) a frame with DC source modules (for the static qubit flux bias), (6) the computer for data acquisition. The rubidium frequency standard and the DC source modules (for biasing the mixers and operating the switches) are not shown. The upconversion board rests on top of the rack on the right.

Generation of phase- and amplitude-controlled pulses is done with an in-phase/quadrature mixing (IQ-mixing, sometimes also called quadrature IF mixing): the signals from two analogue channels of an arbitrary waveform generator (AWG, such as Tektronix 5014C) are fed into the in-phase (I) and quadrature (Q) ports of an IQ-mixer and upconverted to an microwave signal. A signal generator serves as local oscillator (LO) to drive the mixer. The signals on the I and Q ports are either at DC ('direct modulation') or at an IF frequency of typically 100 MHz ('single sideband upconversion'). To avoid applying potentially damaging voltages to the I and Q ports and to improve the impedance matching at these ports, the IF signals from the AWG are attenuated by 3 dBm (or sometimes by 10 dBm). If the amplitude of the microwave signal generated by the mixer is insufficient, it is amplified further by first attenuating it suitably (typically 13 dBm) and then amplifying it with a wideband amplifier ZVA-183+ from Mini-Circuits. If different microwave signals are to be fed into the same microwave line, they are combined using a splitter/combiner.

To correct for imperfections in the IQ-mixers, a DC offset ($\lesssim 20$ mV) is applied to the I and Q ports. To do so, the outputs of an analogue DC source (such as the NI 9264 module) are connected to the 'add input' ports of the AWG channels. Details on the operating principle of an IQ-mixer, as well as mixer calibration are given in app. A.

Table 2.1: Instruments for pulse generation and measurement. Abbreviations used in this table: sampling rate SR, gain G, noise figure NF, output one-dB compression point P_{1dB} , third-order intercept point IP_3 , isolation I. The numbers in the first column refer to the labels in Fig. 2.3.

no.	name & manufacturer	part number	specifications
1	DC source	National Instruments NI9264 (used in a NI chassis)	$\pm 10V$, 16 bit analogue output
-	AWG	Tektronix 5014C	4 channels, SR = 1.2GS/s, $\pm 2.25Vp$
-	Attenuator	Mini-Circuits BW-S3W2+	DC to 18GHz, IL = 3 ± 0.4 dB
-	Mixer	Marki Microwave IQ-4509MXP	LO and RF 4.5 to 9GHz, IF DC to 500 MHz IL ≤ 7.0 dB, Input CP = 6 dBm
-	Wideband amplifier	Mini-Circuits ZFL-ZVA-183+	700 MHz to 18 GHz, G = 26 dB NF = 3.0 dB, P_{1dB} = 24 dBm, IP_3 = 33 dBm
-	Power splitter/combiner	Mini-Circuits ZX10-2-98+	4.75 to 9.8 GHz, two-way 0° , IL = $3 + 0.3$ dB, I = 10 to 23 dB.
2	Analogue signal generator	Agilent E8257D	250 kHz to 20 GHz, -135 to +30 dBm
3	Digital delay generator	Stanford Research Systems DG645	4 channels, 10 MHz rep. rate, 5 ps resolution
4	Power supply	Agilent E3630A	3 channels, 0 to $\pm 20V$ sourcing 0.5A; 0 to 6V sourcing 1 to 2.5A
5	Isolated voltage source	Stanford Research Systems SIM900 (used in a SIM928 mainframe)	1 channel, $\pm 20V$ sourcing ± 10 mA
-	Rb frequency standard	Stanford Research Systems FS725	14 outputs of 10 MHz sine, phase noise < -130 dBc/Hz at 10 Hz, spurs < -100 dBc (100 kHz BW)

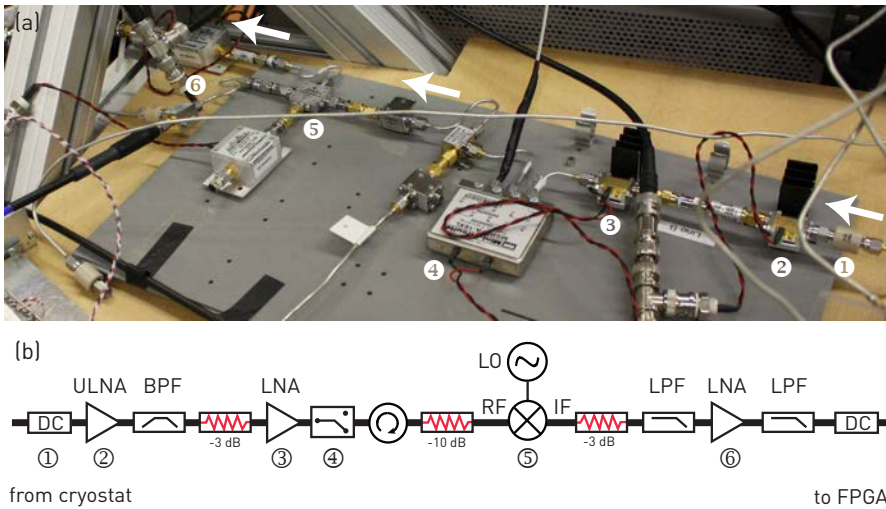


Figure 2.4: (a) Picture and (b) schematic of the downconversion board. See text and Tab. 2.2 for details.

All measurements are triggered. An AWG with a low sampling rate (such as the model 33250A from Agilent with a bandwidth of 80 MHz) produces a trigger which sets the repetition rate (typically 25 kHz) of the experiment. Usually, this trigger is given to an AWG with a larger sampling rate, which distributes it to the other instruments using the marker channels. Alternatively, the AWG with a low sampling rate triggers a digital delay generator, whose triggers can be timed on a ps timescale before being distributed further. This can serve to remove jitter in the AWG analogue outputs, which happens if the raising edge of the trigger arrives at the AWG at an unfortunate time.

To avoid phase drifts in between instruments, the clocks of all devices are phase-locked with a rubidium frequency standard (at 10 MHz). A schematic and a photograph of the instruments involved in signal generation are shown in Fig. 2.3.

2.4 Data acquisition

The microwave signal transmitted through the cryostat is amplified, filtered and down-converted to IF before it is digitized on a data acquisition board and forwarded to a field-programmable gate array (FPGA).

The amplification is achieved by cascading amplifiers, making sure that the output is not compressed by attenuating the signal judiciously. According to Friis' cascade law (Hill, 2008, ch. 6), the total noise figure of a chain of linear amplifiers is dominated by the first amplifier in the chain if its gain is large enough. Therefore, the amplifier with the lowest noise (the HEMT amplifier, or the parametric amplifier, when applicable) is placed at the beginning of the chain. The amplification stages are also interspersed with filters to filter out the noise at frequencies outside the relevant band (and also remove higher harmonics generated by the amplifiers).

Table 2.2: Components in the downconversion chain, and their main specifications. Abbreviations used in this table: gain G , noise figure NF , output one-dB compression point P_{1dB} , third-order intercept point IP_3 , isolation I . The numbers in the first column refer to the labels in Fig. 2.3.

no.	name & manufacturer	part number	specifications
1	DC block	Aeroflex Inmet 8039	$IL \leq 0.5 \text{ dB}$
2	Ultra low noise amplifier	Miteq AFS3-04000800-10-UJLN	4 to 8 GHz, $G = 28 \text{ dB}$, $NF = 1 \text{ dB}$, $P_{1dB} = 10 \text{ dBm}$, $IP_3 = 20 \text{ dBm}$
-	Band-pass filter	Mini-Circuits VHF-3800+	4.25 to 10 GHz, $IL \leq 2 \text{ dB}$ DC to 3.2 GHz, $IL \geq 20 \text{ dB}$
-	Attenuator	Mini-Circuits BW-S3W2+	DC to 18 GHz, $IL = 3 \pm 0.4 \text{ dB}$
3	Low noise amplifier	Miteq AFS3-00101200-42-LN	1 to 12 GHz, $G = 27 \text{ dB}$ $NF = 4.2 \text{ dB}$, $P_{1dB} = 10 \text{ dBm}$, $IP_3 = 20 \text{ dBm}$
4	Switch	Mini-Circuits MSP2TA-18XL	DC to 18 GHz, $IL \leq 0.5 \text{ dB}$, $I \geq 60 \text{ dB}$, failsafe
-	Isolator	Ditom D3I6012	6 to 12.4 GHz, $IL \leq 0.6 \text{ dB}$, $I \geq 17 \text{ dB}$
-	Attenuator	Mini-Circuits BW-S10W2+	DC to 18 GHz, $IL = 10 \pm 0.6 \text{ dB}$
5	Mixer	Marki Microwave IQ-4509MXP	LO and RF 4.5 to 9 GHz, IF from DC to 500 MHz $IL \leq 7.0 \text{ dB}$, input CP = 6 dBm
-	Low-pass filter	Mini-Circuits VLF-105+	DC to 105 MHz, $IL \leq 1 \text{ dB}$ 250 MHz to 4.750 GHz, $IL \geq 20 \text{ dB}$
6	Low noise amplifier	Mini-Circuits ZFL-500LN+	0.1 to 500 MHz, $G = 24 \text{ dB}$ $NF = 2.9 \text{ dB}$, $P_{1dB} = 5 \text{ dBm}$, $IP_3 = 14 \text{ dBm}$
-	Low-pass filter	Mini-Circuits SLP-50+	DC to 48 MHz, $IL \leq 1 \text{ dB}$ 70 to 200 MHz, $IL \geq 20 \text{ dB}$

Because the microwave signal cannot be digitized as is, a mixer identical to the up-conversion one serves as a downconverter. Heterodyne downconversion ($\nu_{\text{LO}} = \nu_{\text{RF}} \pm \nu_{\text{IF}}$) is favoured over homodyne downconversion ($\nu_{\text{LO}} = \nu_{\text{RF}}$, where the signal is converted to DC) because then DC offsets of either the mixer itself or the setup in general do not matter. Furthermore, there is less $1/f$ -noise of the electronics at higher frequencies.

The signal is thus downconverted to 25 MHz before being fed into the ADC of the data acquisition board Nallatech XtremeDSP, which samples the signal with 100 MS/s. On the FPGA (Xilinx Virtex 4), it is then digitally downconverted to DC and filtered to eliminate aliased components of the signal and the peak at DC. For details on the FPGA and the firmware developed at the Quantum Device Lab, see Lang et al. (2013).

More concretely, the microwave signal is processed as follows: it goes through a DC block, is amplified with an ultra low noise amplifier (ULNA), bandpass filtered (BPF), attenuated, amplified with a low noise amplifier (LNA). Then, it travels through a switch (used for mixer calibration, see app. A), an isolator and an attenuator, at which point it is downconverted. Finally, it is lowpass filtered (LPF), amplified and lowpass filtered again before it goes to the ADC of the FPGA board through a DC block. A picture and a schematic of the downconversion board (used in the experiments presented in part II) are shown in Fig. 2.4. The components of the downconversion chain are tabulated in order in Tab. 2.2.

2.5 Experimental basics

2.5.1 Dispersive readout & population reconstruction

The dispersive readout of the transmon is based on frequency shifts occurring between its transitions and the resonator because of their mutual coupling (see sec. 1.3.5 and e.g. Blais et al. (2004); Koch et al. (2007); Bianchetti et al. (2009)). If the transmon-resonator interaction is sufficiently weak (see eq. (1.19)) but not too weak, the resonance frequency of the resonator is shifted by the amount $2\chi_0 - \chi_1$ (in angular frequency), when the transmon is in $|1\rangle$, compared to when it is in $|0\rangle$. Experimentally, this shift is determined by measuring ω_r in a transmission measurement after preparing either $|0\rangle$ or $|1\rangle$. This generalizes to higher energy levels of the transmon, e.g. for $|2\rangle$, the shift amounts to $\chi_0 + \chi_1 - \chi_2$. Fig. 2.5(a) shows transmission spectroscopy of the resonator after preparing the transmon in either $|0\rangle$, $|1\rangle$ or $|2\rangle$. Note that because the excited states sequentially decay into the lower-lying states, there are three peaks in the transmission measurement for $|2\rangle$, and two peaks for $|1\rangle$.

The populations $p_i = \langle |i\rangle \langle i| \rangle$ of the various transmon states can be inferred by recording the averaged resonator response $s(t)$ as a function of time and comparing it to the responses $s_i(t)$ from the $|0\rangle$, $|1\rangle$ and $|2\rangle$ states. If the state to be measured is a superposition of $|0\rangle$ and $|1\rangle$ only, the first excited state population p_1 of any state ρ is proportional to the area enclosed between the time-traces $s_0(t)$ and $s_1(t)$. Similarly, if the state is a superposition of $|1\rangle$ and $|2\rangle$ only, p_2 is proportional to the area between $s_1(t)$ and $s_2(t)$ (Bianchetti et al., 2009).

It is important to note that this procedure assumes that the calibration measurements $s_i(t)$ are exact. This assumption is reasonable although in reality the transmon is $\approx 2\%$ thermally populated³ and the qubit preparation pulses are not perfect. The coupled dy-

³In a recent experiment (Jin et al., 2014), the residual population in the first excited state is shown to be 0.1% when the sample is cooled below 35 mK.

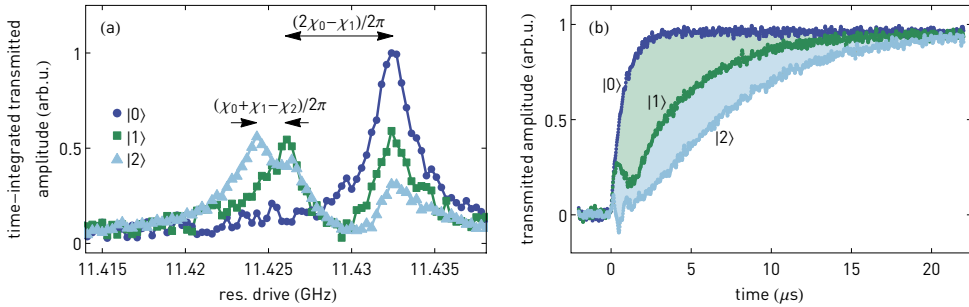


Figure 2.5: (a) Pulsed transmission spectroscopy and (b) time traces $s_0(t)$, $s_1(t)$ and $s_2(t)$ of the resonator with the qubit prepared in $|0\rangle$, $|1\rangle$ or $|2\rangle$.

namics of transmon, cavity and drive are captured by a set of coupled differential equations for the wanted expectation values (Bianchetti et al., 2009), e.g. $\langle a + a^\dagger \rangle$, which is proportional to the voltage in the cavity. These equations *do* account for imprecision in qubit preparation but also neglect thermal population. However, solving them is computationally more expensive than the area method outlined above; thus they were not consistently used in this thesis.

Here, the readout tone is applied at the frequency ω_r , the resonant frequency of the resonator with the transmon in $|0\rangle$. The optimal measurement frequency, allowing to maximize the distinguishability of a population of interest and minimizing the error, however, is different from ω_r . It depends in a complicated fashion on the decoherence rates and the dispersive shifts (Bianchetti, 2010, sec. 5.3). In the experiments presented in this thesis, the measurement frequency was not optimized.

2.5.2 Parametric amplifier

As mentioned in the section about data acquisition, sec. 2.4, in a chain of amplifiers the first one determines the most part of the noise figure. The HEMT amplifiers have a noise temperature of about 4 K and drown out the signal from the resonator. Josephson parametric amplifiers (JPA) operating at the quantum limit (Yurke et al., 1988) provide relief. For an introduction to the parametric amplifiers used here, see e.g. Castellanos-Beltran and Lehnert (2007), Bergeal et al. (2010), and also Eichler and Wallraff (2014) and the references therein. A JPA is a weakly non-linear LC circuit, where the nonlinearity is provided by Josephson junctions, and it works in reflection. Its nonlinearity implies that the phase of the reflected signal not only depends on the frequency, but also on the power of the input signal. Using a strong microwave signal as pump, the JPA is biased at a point where a small input signal detuned from the pump (the signal to be amplified) induces a large change in the output signal.

In this thesis, parametric amplification was used only for the experiments presented in ch. 5, in the form of a Josephson parametric dimer (JPD, Eichler et al. (2014)). The JPD amplifier is a development of the JPA which allows for an increased detuning between pump frequency and resonator frequency. It consists of two capacitively coupled lumped-element resonators with a series of SQUIDS providing a non-linearity, and it is integrated

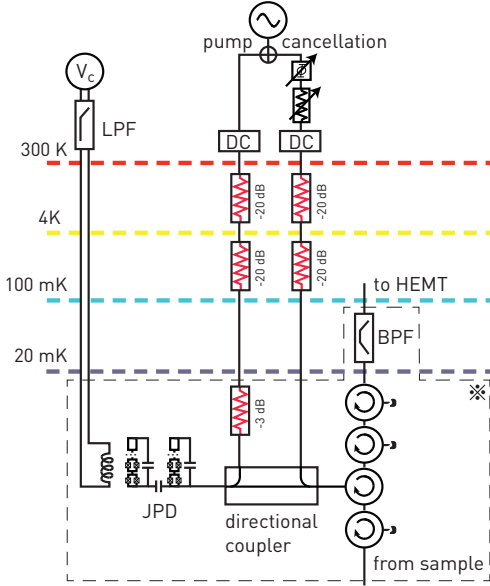


Figure 2.6: Setup of the parametric amplifier. When using the parametric amplifier, the portion in the box marked by * of Fig. 2.1(a) is to be replaced with the box in this figure. In addition, two microwave lines and two DC lines are needed. See text for details.

in the readout chain (see Fig. 2.6) as follows: the output signal from the sample goes to the JPD amplifier via two circulators and a directional coupler. The circulators prevent reflected signals in the output line from leaking into the cavity and separate the amplified signal reflected off the JPD amplifier from the input; the directional coupler is used to operate the JPD amplifier: a tone is split, the first half pumps the JPD amplifier and the second is phase-shifted and attenuated (with a variable phase shifter and a variable attenuator) so that it cancels the pump tone in the amplified signal. Two additional circulators terminated on one port and a band-pass filter (BPF) prevent noise from leaking back into the JPD amplifier. Tuning of the working frequency of the JPD is achieved by changing the static flux bias through the SQUIDS.

2.5.3 Microwave control

The transmon is controlled by microwave tones applied either indirectly via the resonator or directly via a charge gate line. For an optical image of these elements, refer to Fig. 3.2.

Hamiltonian of a driven two-level system

Considering only the lowest transition of the transmon at ω_{01} coupled to a single drive $\mathcal{E}(t) \cos(\omega_d t + \varphi)$, and going to a frame rotating at the drive frequency ω_d , we find (see Blais et al. (2007), or ch. 2 of Boissonneault (2007) for more details)

$$H = \frac{\hbar}{2} (\Omega_x X + \Omega_y Y + \Delta Z), \quad (2.1)$$

with the two quadratures of the drive

$$\Omega_x = \Omega \cos \varphi \quad \Omega_y = \Omega \sin \varphi$$

given in terms of the induced Rabi frequency $\Omega \propto \mathcal{E}$, and the detuning between the $|0\rangle \leftrightarrow |1\rangle$ -transition of the transmon and the drive,

$$\Delta = \omega_{01} - \omega_d.$$

The Hamiltonian eq. (2.1) describes a spin one-half particle in an effective magnetic field

$$H = \hbar \boldsymbol{\sigma} \cdot \mathbf{B}/2. \quad (2.2)$$

with components $\mathbf{B} = (\Omega_x, \Omega_y, \Delta)$ given in units of angular frequency. In the Bloch sphere picture of the $|0\rangle$ - $|1\rangle$ subspace, the two quadratures of the drive induce rotations around the X - and Y -axes, while the detuning induces rotations around the Z -axis. This is a key ingredient of the measurements of the Berry phase presented in part II of this thesis.

Operations on a single two-level system

A series of measurements are routinely performed to calibrate the basic operations on a two-level system (qubit). Pulse schemes and measurement data are shown in Fig. 2.7. All measurements start with a series of microwave pulses to manipulate the qubit, and end with a readout pulse to determine its excited state population. A more detailed discussion of these, and of qubit characterization in general can be found in Baur (2012) for a two-level system or in Bianchetti (2010) for a three-level system.

Rabi oscillations. Rabi flops of the qubit are measured by applying a resonant microwave pulse $\mathcal{E}(t) = \mathcal{E}_0(t) \cos(\omega_{01} t)$ for varying maximal amplitudes of the envelope function $\mathcal{E}_0(t)$. Typically, the envelope has the shape of a truncated Gaussian with a standard deviation of $\mathfrak{s} = 2$ to 5 ns and a duration of $4\mathfrak{s}$. To avoid populating the higher levels of the transmon, a technique called DRAG is used for short ($\lesssim 12$ ns) pulses (Motzoi et al. (2009), see also below in sec. 2.5.3). From this measurement, the amplitude required for a $\pi/2$ - and a π -pulse are extracted.

Ramsey interferometry. The Ramsey experiment is an interferometric measurement of the phase acquired by the qubit. It consists of two $\pi/2$ -pulses separated by a waiting time T . If the pulses are on resonance ($\Delta = 0$), we see an exponential decay of the population in $|1\rangle$ from 1 to 0.5 as T is increased. The decay constant is the decoherence time T_2^* of the two-level system in an ensemble measurement (here, read: temporal average of a single two-level system). If the pulses are off-resonant, the exponential decay in population appears to be modulated with a frequency Δ . Thus, in addition to determining T_2^* , this measurement enables us to determine the resonance frequency ω_{01} to within ~ 50 kHz.

Calibration of the scaling parameter q . The truncated Gaussians have frequency components with a spread inversely proportional to their standard deviation \mathfrak{s} . If the anharmonicity of the low-level system is low and \mathfrak{s} is small, the pulse not only drives the transition at ω_{01} , but also that at ω_{12} . The scheme known as derivative removal by adiabatic gate (DRAG, see Motzoi et al. (2009) and Gambetta et al. (2011)) avoids this spurious driving by

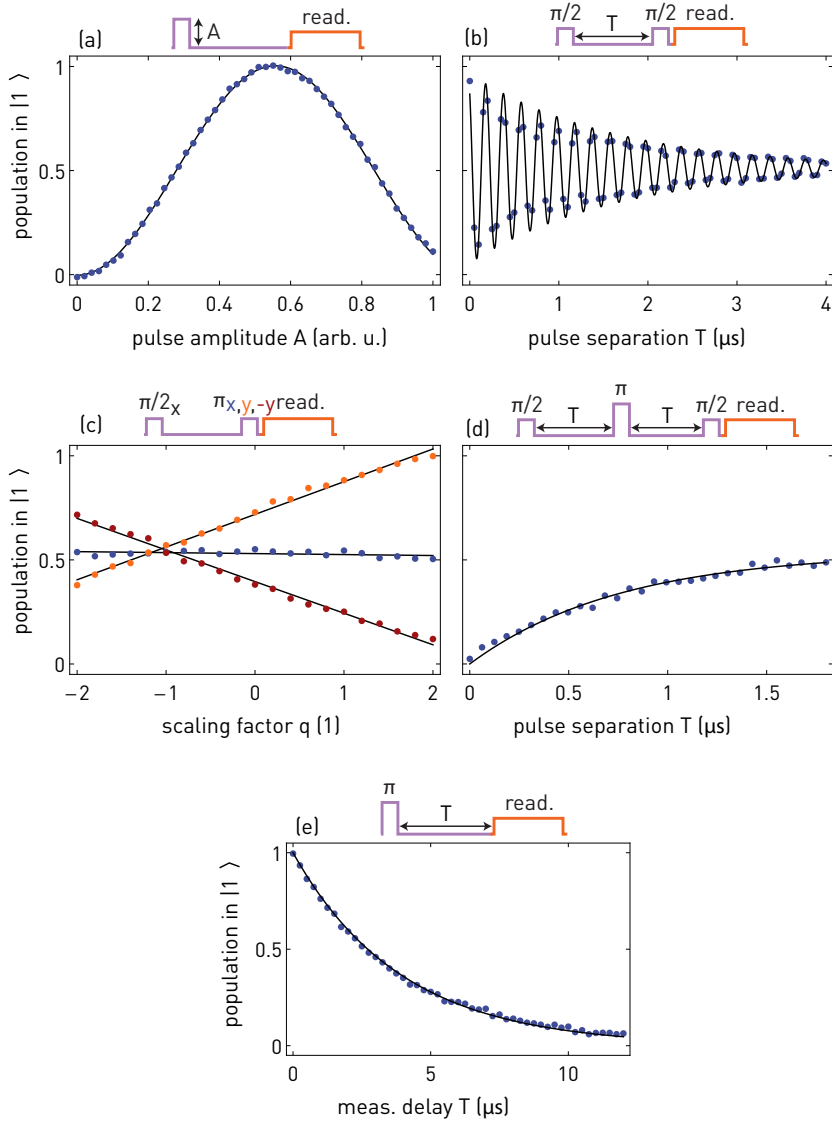


Figure 2.7: Characterization measurements (with fits) for the transition between $|0\rangle$ and $|1\rangle$. (a) Rabi oscillations, (b) Ramsey experiment to determine T_2^* , (c) Calibration of the scaling factor for DRAG compensation, (d) Spin-echo experiment to determine T_2^{echo} , (e) Delayed measurement to determine T_1 .

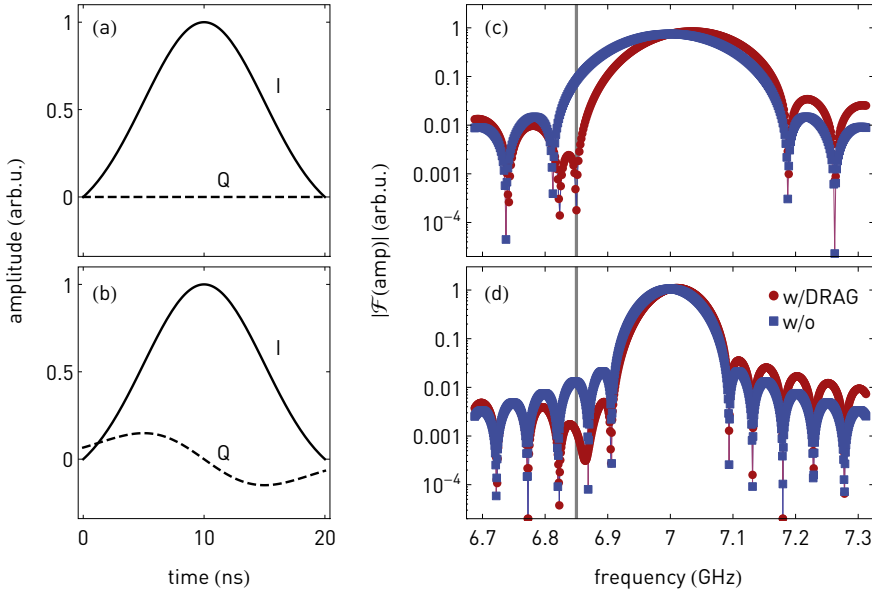


Figure 2.8: (a,b) Pulse envelopes of the I and Q quadratures of a pulse with the shape of a truncated Gaussian assuming $\varsigma = 5$ ns. The pulse in panel (a) is with DRAG compensation, the one in panel (b) without DRAG compensation. (c,d) Absolute value of the Fourier transform of pulses with the shape of a truncated Gaussian, assuming a modulation frequency of $\omega_{01} = 7$ GHz and sampled with 50 GS/s. The vertical grey line indicates ω_{12} . In panel (c), $\varsigma = 2.5$ ns while in panel (d), $\varsigma = 5$ ns.

burning a hole in the Fourier spectrum at ω_{12} . This is achieved by applying a compensation pulse with an envelope proportional to the derivative of the original pulse envelope. The compensation pulse is applied with a phase-shift of $\pi/2$ at the same time as the original pulse. The envelopes of the I and Q quadratures of an uncompensated pulse with $\varsigma = 5$ ns, duration $4\varsigma = 20$ ns is shown in Fig. 2.8(a). In panel (b), the same pulse with DRAG -compensation optimized for an anharmonicity of $\alpha/2\pi = -150$ MHz is shown. In panel (c), we plot the absolute values of the Fourier transform of a pulse with and without DRAG compensation assuming $\varsigma = 2.5$ ns. It is clear that the frequency component at $\omega_{12} = \omega_{01} + \alpha$ is suppressed when using DRAG compensation. In panel (d), $\varsigma = 5$ ns is assumed and as expected the fourier spectrum is narrower. Although the DRAG pulse suppresses the frequency components in the vicinity of ω_{12} , there is not as clear cut a dip at ω_{12} as in (c).

In principle, the amplitude of the compensation pulse is inversely proportional to the anharmonicity α . In practice however, the optimal value is somewhat off; it is $q\alpha$, with some scaling parameter q . The scaling parameter is determined by applying a $\pi/2$ -pulse followed by a π_a -pulse in quick succession for various values of q . This measurement is carried out with three different rotation axes $a = x, y, -y$ of the second pulse. If q is off, phase errors resulting from the first pulse will be mapped into population by the second pulse. For the optimal value of q , the excited state population is 0.5.

Spin-echo experiment. The spin echo experiment is, simply speaking, a Ramsey experiment with a π -pulse in the middle. If there is low-frequency noise in the transition frequency ω_{01} , this pulse will refocus the spins in an ensemble measurement and thus filter out the low-frequency noise. In that case, the observed decay time T_2^{echo} is larger than T_2^* . If there is no noise to be filtered out, $T_2^{\text{echo}} = T_2^*$.

Decay time measurement. The decay time T_1 describes how fast the two-level system decays from excited to ground state. It is determined by preparing the excited state and measuring the remaining excited state population for various measurement delays.

Calibration of a three level-system. When using the lowest three levels $|0\rangle, |1\rangle, |2\rangle$ of the transmon, one first calibrates the transition from $|0\rangle$ to $|1\rangle$. The transition from $|1\rangle$ to $|2\rangle$ is then calibrated similarly. The pulse sequences are identical to those shown in Fig. 2.7, but they are preceded by a π -pulse on ω_{01} to prepare $|1\rangle$, and all other pulses are applied at ω_{12} instead of ω_{01} . See Bianchetti (2010) for details.

PART II

EXPERIMENTS

BEYOND THE TWO-LEVEL APPROXIMATION

Geometric phases are commonly studied in *two-level* systems (see sec. 1.2 for examples). Here, we study the Berry phase in a transmon qubit, which is a weakly anharmonic and strongly driven *multi-level* system.

Recently, the geometric aspects of multi-level systems have attracted increased attention. The geometric phase has been observed in NMR interferometry in a three-level system (Chen et al., 2009). A superconducting phase qudit has been employed as an effective four-level system to show the symmetry of spinors under 2π -rotations, which can be interpreted as a geometric phase (Neeley et al., 2009). Schemes to perform non-adiabatic holonomic quantum computation have been studied theoretically (Sjöqvist et al., 2012) and experimentally (Abdumalikov et al., 2013; Zu et al., 2014).

In contrast to previous measurements in this group by Leek et al. (2007) of the Berry phase in superconducting circuits, where a CPB qubit was used, we now employ a transmon qubit (Koch et al., 2007), where the transition between $|1\rangle$ and $|2\rangle$ is in close vicinity to the transition between $|0\rangle$ and $|1\rangle$. Therefore, whereas the CPB qubit can safely be approximated as a two-level system, the transmon cannot. Higher transmon levels affect the qubit dynamics (see sec. 2.5.3), but can also be employed as a resource for quantum gates (DiCarlo et al., 2009; Fedorov et al., 2012), to improve single-shot readout (Mallet et al., 2009), or to implement a single-photon router (Hoi et al., 2011). Quantum optical experiments involving three levels have been carried out (Baur et al., 2009; Sillanpää et al., 2009; Abdumalikov et al., 2010) and their controlled preparation and tomography has been demonstrated (Bianchetti et al., 2010).

In the first part of this chapter, measurements of the geometric phase of a transmon are presented. It is found that the difference in the level structure between the transmon and an effective two-level system significantly affects the geometric phase. In the following theory section, time-independent perturbation theory is used to model the geometric

phase of a weakly anharmonic multi-level system. Finally, the dependence of the geometric phase on evolution time in both the adiabatic and non-adiabatic regime is analysed.

3.1 Experiment

3.1.1 Experimental idea

We consider the Hamiltonian of a driven n -level qubit in a frame corotating at the drive frequency ω_d ,

$$H(\varphi)/\hbar = \sum_{j=0}^n (j\Delta + \alpha_j)|j\rangle\langle j| + \frac{1}{2}\Omega \sum_{j=0}^{n-1} (\sqrt{j+1}e^{-i\varphi}|j+1\rangle\langle j| + \text{h.c.}), \quad (3.1)$$

where α_j is the anharmonicity defined through the energy of the j th qubit energy level $\omega_{0j} = j\omega_{01} + \alpha_j$ (with $\alpha_0 = \alpha_1 = 0$), Ω is the strength of the drive expressed in units of angular frequency and φ its phase. $\Delta = \omega_{01} - \omega_d$ denotes the detuning between the frequency ω_{01} of the $|0\rangle \leftrightarrow |1\rangle$ transition and the drive frequency ω_d . The increase of the coupling strength $\propto \sqrt{j+1}$ follows from the off-diagonal matrix elements of the charge operator (see eq. (1.18)). In the two-level approximation, we restrict the Hamiltonian to the computational subspace of the qubit spanned by $|0\rangle$ and $|1\rangle$:

$$H \approx \hbar(X\Omega_x + Y\Omega_y + Z\Delta)/2 = \hbar\boldsymbol{\sigma} \cdot \mathbf{B}/2,$$

with $\Omega_x = \Omega \cos \varphi$, $\Omega_y = \Omega \sin \varphi$, and the Pauli matrices X, Y, Z . We have thus recovered from eq. (3.1) the result from sec. 2.5.3: In an appropriate frame, a two-level system with a classical drive is effectively described by the Hamiltonian of a spin-half particle in an magnetic field $\mathbf{B} = (\Omega_x, \Omega_y, \Delta)$.

By tuning amplitude and phase of the microwave drive, the qubit is guided along a circular path C with constant detuning Δ . At first, the drive field is ramped up, tilting \mathbf{B} so that it forms an angle $\vartheta = \arctan(\Omega/\Delta)$ with respect to the B_z -axis. Then, the phase of the drive is swept by 2π , causing \mathbf{B} to rotate once around the B_z -axis, either clockwise or anticlockwise. Finally, the drive is ramped back to zero. The time evolution of both quadratures of the drive is plotted in Fig. 3.1(a), the path of the effective magnetic field in parameter space is shown in Fig. 3.1(b).

During this sequence, the solid angle subtended by the path as seen from the origin is $A = 2\pi(1 - \cos \vartheta)$. We then repeat the measurement for different driving strengths Ω , thereby changing the solid angle A . If qubit evolves adiabatically, the states $|0\rangle$ and $|1\rangle$ follow the instantaneous eigenstates of eq. (3.1.1), and A , the solid angle enclosed by \mathbf{B} in parameter space, is equal to the solid angle A' the states $|0\rangle$ and $|1\rangle$ enclose in the Hilbert space of the qubit (Fig. 3.1(c)). In the adiabatic case, the parameter space can be identified with the Hilbert space and therefore $A = A'$. However, in general the geometric phase is determined by A' , not A .

3.1.2 Sample and setup

For manipulation and readout, the transmon is coupled to a coplanar transmission line resonator of quality factor $Q = 2155$ via a gate capacitance C_g . An optical microscope

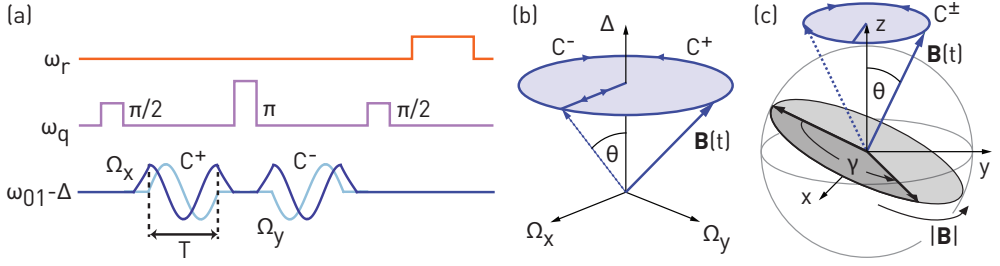


Figure 3.1: (a) Sketch of the microwave pulse sequence used in a geometric phase measurement, consisting of a series of resonant (ω_{01}) and off-resonant ($\omega_{01} - \Delta$) pulses applied either on the x-quadrature (dark blue) or the y-quadrature (light blue). The geometric phase is generated by the adiabatic evolution of the qubit between the resonant pulses. (b) Path of the effective magnetic field $\mathbf{B}(t)$ in parameter space ($\Omega_x, \Omega_y, \Delta$). When performing the loop C^+ or C^- , it forms an angle ϑ with the Δ -axis. (c) Evolution of the state vector of the qubit on the Bloch sphere as the effective magnetic field $\mathbf{B}(t)$ performs a loop C^\pm adiabatically in parameter space. In this illustration, the parameter space of the effective magnetic field and the projective Hilbert space of the qubit are overlaid. The state vector precesses around the instantaneous axis $\mathbf{B}(t)$ at a rate $|\mathbf{B}(t)|$, acquiring a total phase γ . During a loop C^\pm , $\mathbf{B}(t)$ traces out a loop C^\pm . The graphics in (b) and (c) are adapted from Leek et al. (2007).

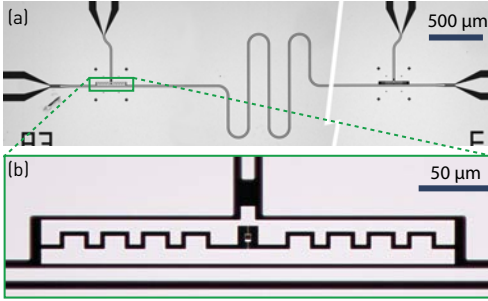


Figure 3.2: (a) Optical microscope image of the sample with two transmons coupled to a coplanar waveguide resonator with individual capacitively coupled microwave gate lines. (b) Close-up of the transmon used in the experiments.

image of the sample is shown in Fig. 3.2. The sample is mounted in a dilution refrigerator and operated at a temperature of 20 mK. The transition frequency of the transmon is tunable by externally applied magnetic flux Φ , generated using superconducting coils mounted underneath the sample. The transmon state is manipulated using resonant and off-resonant microwave tones (of frequency ω_{01} and $\omega_{01} - \Delta$, respectively) created by AC modulation of an in-phase/quadrature-mixer. This provides individual control of both quadratures (x and y) of the driving microwave signal, which couples capacitively to the transmon via a local charge gate line.

From spectroscopic measurements, we have determined a maximum Josephson energy $E_J/h = 13.96$ GHz and a charging energy $E_C/h = 0.36$ GHz, which corresponds to a maximum transition frequency $\omega_{01,\max}/2\pi = 5.95$ GHz, and a coupling strength $g/2\pi = 360$ MHz to the fundamental mode of the resonator. To reduce the Purcell effect and optimize coherence properties, $\omega_{01,\max}$ was designed to lie below the fundamental mode of the resonator (Houck et al., 2008). The experiment is carried out in the dispersive regime, where the transmon, biased at $\omega_{01,\max}$, is non-resonantly coupled to the resonator (at frequency $\omega_r/2\pi = 6.662$ GHz with the qubit in the ground state) and can be read out via a state-dependent change in the microwave tone of frequency ω_r transmitted through

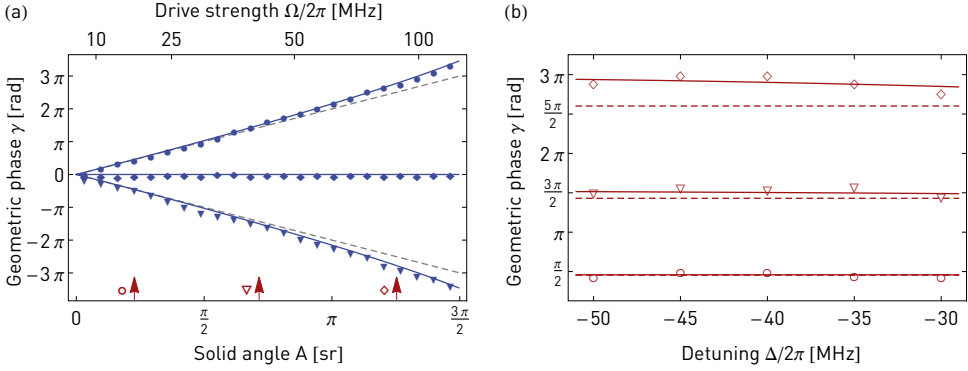


Figure 3.3: (a) Extracted phase γ as a function of solid angle A . Shown is the experimental data for C^{++} (circles), C^{+-} (triangles) and C^{--} (diamonds), as well as the geometric phase obtained with second-order perturbation theory (solid lines, eq. (3.5)) and the prediction for a two-level system (dashed lines). The off-resonant pulses were applied with detuning $\Delta/2\pi = -35$ MHz. (b) Extracted phase γ as a function of detuning Δ . The experimental data for solid angles $A \approx \pi/4, 3\pi/4$, and $5\pi/4$ (indicated by circles, triangles and diamonds, respectively, and also indicated by arrows in (a)) is shown alongside the geometric phase calculated using second-order perturbation theory (solid lines) and the prediction for a two-level system (dashed lines). In both panels, the measurement uncertainties are smaller than the size of the markers.

the resonator (see sec. 2.5.1). Since $E_J/E_C = 39 \gg 1$ and the anharmonicity is $\alpha_2/2\pi = -423$ MHz, our sample is operated well within the transmon regime. Charge dispersion is expected to amount to about 100 kHz for ω_{01} and about 2.9 MHz for ω_{12} . We have measured an energy relaxation time $T_1 = 0.84 \mu\text{s}$, a phase coherence time $T_2^* = 1.03 \mu\text{s}$ and a spin-echo phase coherence time $T_{2,\text{echo}} = 1.11 \mu\text{s}$.

3.1.3 Measurement of the geometric phase

To determine the geometric phase experimentally, we employ an interferometric measurement (see Fig. 3.1(a)). The leading and trailing resonant $\pi/2$ -pulses implement a Ramsey measurement, while the resonant spin-echo π -pulse in the centre serves to cancel the dynamic phase (Jones et al., 2000; Leek et al., 2007). After preparing an equal superposition of the $|0\rangle$ and $|1\rangle$ states, the qubit traverses the path C^- (see fig:phasepulsescheme(c)) and the relative phase $2(\gamma_d - \gamma_g)$ acquired between $|0\rangle$ and $|1\rangle$ comprises both a dynamic (γ_d) and a geometric (γ_g) contribution (see Fig. 3.4(a)). The spin-echo π -pulse then effectively flips the sign of the phase. As it traverses the second loop in the opposite direction, C^+ , the qubit acquires the phase $2(\gamma_d + \gamma_g)$ since the dynamic phase, unlike the geometric phase, is independent of the direction of evolution. Thus, after following the contours C^{++} , dynamic phase contributions cancel out and the qubit state has acquired a phase $\gamma = 4\gamma_g$ which is purely geometric. Tracing out the contours in opposite direction, C^{+-} , simply inverts the sign of the phase, while following the contours twice in the same direction, C^{++} or C^{--} , results in zero phase and serves as a control experiment (see Fig. 3.3(a)).

During the off-resonant pulse sequences C^\pm , the drive Ω is strong (corresponding to induced Rabi-frequencies $\lesssim 110$ MHz) and therefore the higher levels of the qubit are populated as well. In order to visualize this population leakage, we consider the Hilbert space of a three-level system. Neglecting a global phase, any three-level state can be written as

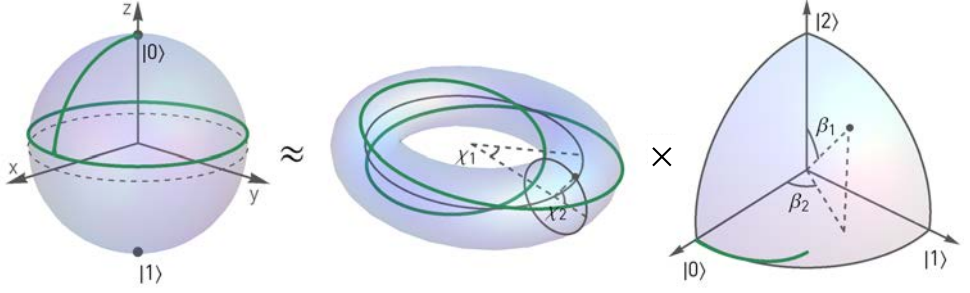


Figure 3.4: Simulated adiabatic evolution (green line) of the ground state subjected to the off-resonant drive along the path C^- , visualized in the Hilbert space of a three-level system and on the Bloch sphere, the approximate two-level equivalent (see text for details).

$|\psi\rangle = e^{i\chi_1} \sin \beta_1 \cos \beta_2 |0\rangle + e^{i\chi_2} \sin \beta_1 \sin \beta_2 |1\rangle + \cos \beta_1 |2\rangle$, where $\chi_{1,2} \in [0, 2\pi]$ are the phases of the ground and first excited state, respectively, relative to the phase of the second excited state, and $\beta_{1,2} \in [0, \pi/2]$ parameterize the populations. Therefore, every state can be represented as a point in the product manifold of a torus and an octant of a unit sphere (see sec. 1.1.4). Observing that $\beta_1 \neq \pi/2$ while the ground state is subjected to the off-resonant drive C^- (see Fig. 3.4), we conclude that the instantaneous ground state leaves the computational subspace. The population of second excited state reaches up to $\approx 12\%$, showing the necessity to consider the higher levels in our experiment. It is important to note that all resonant pulses effectively act in the subspace spanned by $|0\rangle$ and $|1\rangle$: in order to avoid exciting higher energy levels with the resonant pulses, we use DRAG-pulses (see sec. 2.5.3). Furthermore, to ensure that the second excited state $|2\rangle$ is depleted before the resonant pulses are applied, the off-resonant drive is adiabatically ramped down.

After qubit manipulation, which takes approximately 700ns, the population $p_z = (1 - Z)/2$ of the first excited state is extracted by a dispersive readout (see sec. 2.5.1). The phase γ the qubit has acquired during evolution is reconstructed with state tomography. The second $\pi/2$ -pulse of the Ramsey sequence rotates the qubit about either the x or y axis, and serves as tomography pulse. In the absence of decoherence, the phase γ is given by $\arctan(\langle Y \rangle / \langle X \rangle)$ with $\langle X \rangle = \cos \gamma$, $\langle Y \rangle = \sin \gamma$ and $\langle Z \rangle = 0$. The same expression approximates γ well even in the presence of decoherence, which reduces the size of the Bloch vector $(\langle X \rangle, \langle Y \rangle, \langle Z \rangle)$ to 0.47 in our experiments, while keeping the ratio $\langle Y \rangle / \langle X \rangle$ constant. Therefore, the geometric phase remains unaltered by the decoherence in our experimental setting.

In keeping with Berry's predictions for a two-level system, $\gamma = 2A$, we measure a phase γ which is approximately twice the solid angle A subtended by the path (see Fig. 3.3(a)). However, the data clearly shows that γ increasingly deviates from Berry's predictions as A (and therefore also the amplitude of the drive Ω) increases: the measured geometric phase is observed to be up to 15% larger than expected.

3.2 Theory

These deviations can be explained by the presence of higher transmon levels. In this section, the couplings between the levels $|2\rangle, |3\rangle, \dots$ are treated as a perturbation and an expression quantifying their effect on the geometric phase of a two-level-system is derived. The calculations are based on Pechal (2010).

3.2.1 Perturbative treatment of higher levels

Defining the operator $N = \sum_{j=0}^n j|j\rangle\langle j|$, the Hamiltonian in eq. (3.1) can be rewritten as $H(\varphi) = e^{-i\varphi N} H(0) e^{i\varphi N}$. It follows that, given an eigenvector $|\Phi(0)\rangle$ of $H(0)$, $|\Phi(\varphi)\rangle = e^{-i\varphi N} |\Phi(0)\rangle$ is an eigenvector of $H(\varphi)$. For the circular path C described above, the geometric phase $\gamma_{|\Phi(0)\rangle}$ acquired by the eigenvector $|\Phi(0)\rangle$ is then found to be via eq. (1.7)

$$\gamma_{|\Phi(0)\rangle} = i \int_0^{2\pi} \langle \Phi(\varphi) | \frac{d}{d\varphi} | \Phi(\varphi) \rangle d\varphi = 2\pi \langle \Phi(0) | N | \Phi(0) \rangle. \quad (3.2)$$

From eq. (3.2), one indeed recovers the expression $\gamma_{\pm}^{(0)} = \pi(1 \pm \cos \vartheta)$ for the geometric phase of a two-level system, where the sign \pm corresponds to the positive and negative eigenvalue of $H(0)$, respectively. To compute the geometric phase for a multi-level system, we divide the Hamiltonian $H(0) = H_0 + V$ into a block-diagonal part H_0 coupling the lowest two transmon levels, and a perturbative part V coupling the remaining levels:

$$\begin{aligned} H_0 &= \hbar \sum_{j=0}^n (j\Delta + \alpha_j) |j\rangle\langle j| + \frac{\hbar\Omega}{2} (|1\rangle\langle 0| + \text{h.c.}), \\ V &= \frac{\hbar\Omega}{2} \sum_{j=1}^{n-1} (\sqrt{j+1} |j+1\rangle\langle j| + \text{h.c.}), \end{aligned}$$

which is, pictorially,

$$H = H_0 + V = \begin{pmatrix} \star & \star & & & \\ \star & \star & \star & & \\ & \star & \star & \star & \\ & & \star & \star & \dots \\ & & & \dots & \dots \end{pmatrix} = \begin{pmatrix} \star & \star & & & \\ \star & \star & & & \\ & & \star & & \\ & & & \star & \\ & & & & \dots \end{pmatrix} + \begin{pmatrix} & & & & \\ & & \star & & \\ & & \star & & \\ & & & \dots & \\ & & & & \dots \end{pmatrix}.$$

Substituting the expansion of the eigenvectors in V , $|\Phi_j\rangle = |\Phi_j^{(0)}\rangle + |\Phi_j^{(1)}\rangle + |\Phi_j^{(2)}\rangle + \dots$, into eq. (3.2) and retaining terms up to second order, one finds

$$\gamma_j = 2\pi \left(\langle \Phi_j^{(0)} | N | \Phi_j^{(0)} \rangle + 2 \text{Re} \langle \Phi_j^{(0)} | N | \Phi_j^{(1)} \rangle + \langle \Phi_j^{(1)} | N | \Phi_j^{(1)} \rangle + 2 \text{Re} \langle \Phi_j^{(0)} | N | \Phi_j^{(2)} \rangle \right). \quad (3.3)$$

Considering that

$$\begin{aligned} |\Phi_-^{(0)}\rangle &= \cos(\vartheta/2) |0\rangle - \sin(\vartheta/2) |1\rangle, \\ |\Phi_+^{(0)}\rangle &= \sin(\vartheta/2) |0\rangle + \cos(\vartheta/2) |1\rangle, \\ |\Phi_j^{(0)}\rangle &= |j\rangle, \quad 2 \leq j \leq n \end{aligned}$$

the first term in eq. (3.3), $\langle \Phi_j^{(0)} | N | \Phi_j^{(0)} \rangle$, yields $\pi(1 \mp \cos \vartheta)$ for $n = \pm$ and $2\pi n$ for $2 \leq j \leq n$. In other words, it gives the two-level geometric phase for the two lowest energy levels and an unobservable contribution for the higher energy levels. The second term in eq. (3.3), vanishes for the following reasons: If $2 \leq j \leq n$,

$$\text{Re} \langle \Phi_j^{(0)} | N | \Phi_j^{(1)} \rangle = j \text{Re} \langle \Phi_j^{(0)} | \Phi_j^{(1)} \rangle = 0,$$

because of the normalization of the perturbed states, $\text{Re} \langle \Phi_j^{(0)} | \Phi_j^{(1)} \rangle = 0$. If, on the other hand, $j = \pm$, we notice that due to the form of V ,

$$|\Phi_{\pm}^{(1)}\rangle = \sum_{k \neq \pm} \frac{\langle \Phi_k^{(0)} | V | \Phi_{\pm}^{(0)} \rangle}{E_{\pm}^{(0)} - E_k^{(0)}} |\Phi_k^{(0)}\rangle \propto |2\rangle,$$

and that therefore the matrix elements $\langle \Phi_{\pm}^{(0)} | N | \Phi_j^{(1)} \rangle$ vanish.

In order to compute the remaining terms in eq. (3.3), we refer to the formulae for the first and second order corrections to the eigenvectors:

$$|\Phi_j^{(1)}\rangle = \sum_{k \neq j} \frac{V_{kj}}{E_{kj}} |\Phi_k^{(0)}\rangle, \quad (3.4a)$$

$$|\Phi_j^{(2)}\rangle = \sum_{k, l \neq j} \frac{V_{kl} V_{lj}}{E_{kj} E_{lj}} |\Phi_k^{(0)}\rangle - \sum_{k \neq j} \frac{V_{kj} V_{jj}}{E_{kj}^2} |\Phi_k^{(0)}\rangle - \frac{1}{2} |\Phi_j^{(0)}\rangle \sum_{k \neq j} \frac{V_{jk} V_{kj}}{E_{kj}^2}, \quad (3.4b)$$

where $V_{kj} = \langle \Phi_k^{(0)} | V | \Phi_j^{(0)} \rangle$ and $E_{kj} = E_j^{(0)} - E_k^{(0)}$. In this case, since V has no diagonal elements, the second term in eq. (3.4b) is zero.

The correction to the geometric phase now boils down to

$$\begin{aligned} \frac{\Delta\gamma_j}{2\pi} &\equiv \frac{\gamma_n - \gamma_n^{(0)}}{2\pi} = 2 \text{Re} \langle \Phi_j^{(0)} | N | \Phi_j^{(0)} \rangle + \langle \Phi_j^{(1)} | N | \Phi_j^{(1)} \rangle \\ &= 2 \text{Re} \sum_{k, l \neq j} \frac{V_{kl} N_{jk} V_{lj}}{E_{kj} E_{lj}} - \sum_{k \neq j} \frac{V_{kj} N_{jj} V_{jj}}{E_{kj}^2} + \sum_{l, k \neq j} \frac{V_{jl} N_{lk} V_{kj}}{E_{kj} E_{lj}} \end{aligned}$$

where $N_{kj} = \langle \Phi_k^{(0)} | N | \Phi_j^{(0)} \rangle$. Taking into account the matrix elements of V , and specializing for $j = \pm$, we find

$$\frac{\Delta\gamma_j}{2\pi} = \frac{V_{j2} V_{2j}}{E_{2n}^2} (N_{22} - N_{nn}) + 2 \text{Re} \frac{N_{n\bar{n}} V_{\bar{n}2} V_{2n}}{E_{\bar{n}n} E_{2n}},$$

where \bar{n} denotes the sign opposite to n . Substituting the matrix elements

$$V_{2-} = g_{12} \sin(\vartheta/2), \quad V_{2+} = g_{12} \cos(\vartheta/2)$$

$$N_{++} = \cos^2(\vartheta/2), \quad N_{--} = \sin^2(\vartheta/2), \quad N_{-+} = N_{+-} = \sin(\vartheta/2) \cos(\vartheta/2),$$

we obtain the expressions

$$\begin{aligned} \frac{\Delta\gamma_-}{2\pi} &= \frac{\hbar^2 \Omega^2 |g_{12}|^2}{4E_{2-}^2} \left(\sin^2(\vartheta/2) + \frac{2E_{2-} + E_{+-}}{E_{+-}} \sin^2(\vartheta/2) \cos^2(\vartheta/2) \right) \\ \frac{\Delta\gamma_+}{2\pi} &= \frac{\hbar^2 \Omega^2 |g_{12}|^2}{4E_{2+}^2} \left(\sin^2(\vartheta/2) + \frac{2E_{2+} + E_{-+}}{E_{-+}} \cos^2(\vartheta/2) \cos^2(\vartheta/2) \right). \end{aligned}$$

Finally, we want to express all quantities in terms of the angle ϑ . To this effect, we note that, because $\cos \vartheta = \Delta / \sqrt{\Delta^2 + \Omega^2}$, the energies can be written as

$$\begin{aligned} E_{-}^{(0)} &= -\hbar \sqrt{\Delta^2 + \Omega^2} \sin^2(\vartheta/2) = -\hbar \Delta \sin^2(\vartheta/2) / \cos \vartheta, \\ E_{+}^{(0)} &= +\hbar \sqrt{\Delta^2 + \Omega^2} \cos^2(\vartheta/2) = +\hbar \Delta \cos^2(\vartheta/2) / \cos \vartheta, \\ E_2^{(0)} &= \hbar(2\Delta + \alpha_2) = -\hbar \Delta / \cos \vartheta, \end{aligned}$$

and therefore

$$E_{2-} = E_{-}^{(0)} - E_2^{(0)} = -\hbar(\Delta + (2\alpha_2 + 3\Delta) \cos \vartheta) / 2 \cos \vartheta.$$

For the deviation in the geometric phase, we then find the central result of this section

$$\frac{\Delta\gamma_{\pm}}{2\pi} = \frac{k|g_{12}|^2 \sin^2 \vartheta}{4} \frac{2k(1 \pm \cos \vartheta) + (2k \mp (3k+2) \cos \vartheta) \sin^2 \vartheta}{(k \mp (3k+2) \cos \vartheta)^2}, \quad (3.5)$$

where $k \equiv \Delta/\alpha_2$ is the ratio of detuning to anharmonicity. We note that this deviations stems from the second excited state only. Due to the nature of the experimental measurement of the geometric phase, i.e. a Ramsey sequence including a spin-echo pulse, the measured geometric phase deviation is the quantity $\Delta\gamma \equiv 2(\Delta\gamma_{-} - \Delta\gamma_{+})$. Expanding eq. (3.5) to first order in k gives

$$\Delta\gamma \approx \frac{\pi \Delta |g_{12}^2| \sin^4 \vartheta}{\alpha_2 \cos \vartheta}$$

which vanishes for large α_2 as expected.

3.2.2 Applicability to experiment

Since in the experiment $k \approx 1/8$ is small and $|\Omega/\alpha_2| \ll 1$, the expansion coefficients of $|\Phi_j^{(1)}\rangle$ and $|\Phi_j^{(2)}\rangle$ are small, and perturbative treatment is justified. To verify the validity of the perturbative treatment, we simulated the qubit evolution for the pulse sequence in Fig. 3.1(a), retaining four energy levels in a quantum master equation simulation, thereby taking into qubit population decay, decoherence and non-adiabatic effects arising from finite evolution time (Ai et al., 2009). Also, the Hamiltonian in eq. (3.1) with $n = 4$ was numerically diagonalize to compute the geometric phase in the limit of perfect adiabaticity. We found that the perturbatively computed geometric phase γ using eq. (3.5) differs from both simulations and numerical results by less than 2%. Furthermore, we have measured γ for a range of detunings Δ and have found good agreement with the geometric phase computed using perturbation theory (see Fig. 3.3(b)).

It was also verified that the geometric phase does not depend on the dispersive coupling of the transmon to the resonator by tuning ω_{01} such that $\delta = \omega_r - \omega_{01} = 1.58$ GHz and comparing the data to the case shown in Fig. 3.3(a), where $\delta = 0.71$ GHz.

The quantities appearing in eq. (3.5), namely $k = \Delta/\alpha_2$, the angle ϑ and the coupling g_{12} can be determined with great accuracy (≈ 200 kHz for k and g_{12} , $\approx 2^\circ$ for ϑ). As a result, both the computed correction $\Delta\gamma$ to the Berry phase and the experimental data in Fig. 3.3 have small errors, and the observed deviation in geometric phase from Berry's prediction for a two-level system is meaningful despite its small size.

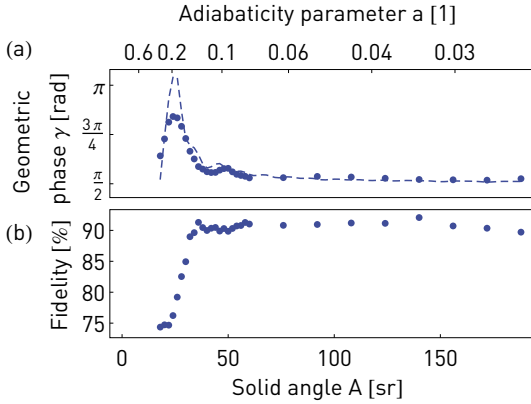


Figure 3.5: (a) Measured phase γ as function of precession period T for the solid angle $A = \pi/4$ at detuning $\Delta/2\pi = -45$ MHz. The dashed line is the phase obtained by numerically calculating the unitary time evolution of a four level transmon using the Schrödinger equation. The adiabaticity parameters a for a given T are indicated on the upper horizontal axis. (b) Fidelity of the geometric phase gates shown in (a) as a function of T .

3.3 Adiabaticity

Finally, the transition from the adiabatic regime to the non-adiabatic regime was examined by measuring the acquired phase γ at fixed solid angle $A = \pi/4$, changing only the phase precession period T (Fig. 3.1(a)) but keeping the duration of the total sequence constant. The data in Fig. 3.5(a) show that γ is constant, i.e., independent of evolution time for T larger than about 50 ns, or equivalently, for adiabaticity parameters $a = \dot{\varphi} \sin(\vartheta)/|\mathbf{B}| \lesssim 0.1$. The measured γ also agrees well with the result obtained by numerically solving the Schrödinger equation. For values of $a > 0.1$, when entering the non-adiabatic regime, we observe that γ oscillates and varies by more than 50%. In this regime, γ is a combination of dynamic and geometric phase because the spin-echo technique fails to cancel the dynamic phase: for non-adiabatic evolution, the state after the spin-echo π -pulse does not necessarily correspond to the initial state with $|0\rangle$ and $|1\rangle$ interchanged.

In the context of quantum information processing, the manipulation sequence could serve as a single qubit phase gate. Its performance can be assessed by computing the fidelity $F = \text{tr} \sqrt{\rho^{1/2} \sigma \rho^{1/2}}$, where ρ is the experimental density matrix processed with maximum likelihood (Ježek et al., 2003) and σ is the expected density matrix for perfectly adiabatic evolution. We find that the fidelity of the gate averages $F = 90\%$ in the adiabatic regime (Fig. 3.5(b)). There, about 8% of the loss in fidelity can be attributed to qubit decay, whereas inaccuracies in qubit preparation and qubit dephasing account for the remaining 2%. In the non-adiabatic regime a significant decrease in fidelity is observed, as expected.

3.4 Conclusion

In conclusion, we have measured the geometric phase in a multi-level system with small anharmonicity and observed that the two-level approximation breaks down for strong drives, as evidenced in our experiment by deviations of the geometric phase from the expected linear dependence on solid angle. We have modelled the contributions from the second excited state to the adiabatic geometric phase using time-independent perturbation theory. By examining Berry's phase in the adiabatic limit and going to the non-adiabatic regime, we have shown that it is independent of evolution time for adiabaticity

parameters $\lesssim 0.1$. The phase in the non-adiabatic limit could potentially inherit some of the adiabatic phase's noise resilience, suggesting further experimental tests on how it is affected by noise in the control parameters.

NOISE RESILIENCE OF THE BERRY PHASE

Noise is ubiquitous in physical systems—be it thermal noise in electrical circuits (Robinson, 1974), electronic shot noise in mesoscopic conductors (Blanter and Buttiker, 2000), vacuum noise of radiation fields (Glauber, 1963), or low-frequency ($1/f$) noise in solid state systems (Dutta and Horn, 1981; Bylander et al., 2011). Noise is troublesome, as it prevents quantum coherence to persist on long time scales and hinders the development of a large-scale quantum computer (Schlosshauer, 2007; Joos et al., 2003), and significant effort is needed to control and maintain fragile quantum superposition states (Ladd et al., 2010).

Quantum dissipative systems also call into question the nature of the Berry phase: noise may screen out geometric effects and makes defining adiabaticity difficult. Fortunately, there are many ways to address these concerns. For one, noise can be modeled by adding non-geometric dissipative rates to the equations of motion (see e.g. Ellinas et al. (1989)). Whitney and Gefen (2003) alleviate the latter concern—a gapless spectrum does not necessarily annul the Berry phase.

The Berry phase is a potential building-block for noise-resilient quantum operations (Sjöqvist, 2008). Although the effect of noise on the Berry phase has been well studied in theory, (Blais and Tremblay, 2003; De Chiara and Palma, 2003; Whitney et al., 2005; Whitney and Gefen, 2003; Carollo et al., 2003; Solinas et al., 2010; Villar and Lombardo, 2011; Solinas et al., 2012), so far there have been only a few experiments studying the dephasing it causes (Leek et al., 2007; Filipp et al., 2009; Cucchietti et al., 2010; Wu et al., 2013). Here, adiabatic artificial fluctuations in the path of the control field are introduced to induce dephasing in a two-level system. The measurements show that only fluctuations which distort the path lead to dephasing originating from fluctuations of the Berry phase. In a direct comparison with the dynamic phase we observe that the Berry phase is less affected by noise-induced dephasing.

The first part of this chapter introduces analytical expressions for noise-induced dephasing. The second part presents the experiments and compares data to calculations.

4.1 Analytical expressions

4.1.1 Noise-induced dispersion in phase

We derive the effect noise has on the phases of a two-level system along the lines of De Chiara and Palma (2003). The idea is to see how noise on the control parameters affects the Berry connection, and thus also the Berry phase.

The Hamiltonian of a spin-half particle in a magnetic field is (see also sec. 2.5.3)

$$H = \hbar \boldsymbol{\sigma} \cdot \mathbf{B}/2, \quad (4.1)$$

with \mathbf{B} expressed in units of angular frequency. When the magnetic field is varied adiabatically, the instantaneous energy eigenstates follow the direction of the magnetic field by virtue of the adiabatic theorem. They are

$$|+\rangle = \cos \frac{\vartheta}{2} |1\rangle + e^{i\varphi} \sin \frac{\vartheta}{2} |0\rangle, \quad |-\rangle = \sin \frac{\vartheta}{2} |1\rangle - e^{i\varphi} \cos \frac{\vartheta}{2} |0\rangle$$

where $|0\rangle$ and $|1\rangle$ are the eigenstates of the Pauli matrix Z . According to eq. (1.8), the Berry phase of $|+\rangle$ after a cyclic evolution is $\gamma_+ = \oint \mathbf{A}^+ \cdot d\boldsymbol{\lambda}$, where $\mathbf{A}^+ = i\langle + | \nabla_{\boldsymbol{\lambda}} | + \rangle$ is the Berry connection and $\boldsymbol{\lambda}$ are the control parameters. We consider a path in which the magnetic field has a constant magnitude and precesses around the B_z -axis at an angle ϑ . Thus, the control parameters are the angles ϑ and φ . The components of the connection are

$$A_\varphi^+ = -A_\varphi^- = i\langle + | \frac{\partial}{\partial \varphi} | + \rangle = \frac{1}{2} \cos \vartheta, \quad A_\vartheta^+ = -A_\vartheta^- = i\langle + | \frac{\partial}{\partial \vartheta} | + \rangle = 0,$$

and the geometric phase is

$$\gamma_+ = -\gamma_- = \int_0^{2\pi} A_\varphi^+ d\varphi = \pi \cos \vartheta.$$

We now add a fluctuating field \mathbf{K} to the magnetic field \mathbf{B} . The Hamiltonian eq. (4.1) becomes

$$H = \hbar \boldsymbol{\sigma} \cdot (\mathbf{B} + \mathbf{K})/2.$$

The noise \mathbf{K} modifies both the connection \mathbf{A} and the control parameters $\boldsymbol{\lambda}$. Expanding the connection around the polar angle ϑ_0 with no noise gives

$$A_\varphi(\vartheta) = A_\varphi(\vartheta_0) + \frac{\partial A_\varphi}{\partial \vartheta} \delta\vartheta = \frac{1}{2} (\cos \vartheta_0 - \delta\vartheta \sin \vartheta_0),$$

where $\delta\vartheta$ are the fluctuations caused by the noise. The change in the line element is expanded similarly:

$$d\boldsymbol{\lambda} = \dot{\boldsymbol{\varphi}} dt \approx (\dot{\boldsymbol{\varphi}}_0 + \delta\dot{\boldsymbol{\varphi}}) dt,$$

where $\dot{\varphi} = 2\pi/T$ is the average precession velocity. Combining both expansions yields an expression for the Berry phase:

$$\begin{aligned}\gamma &= \int_0^T (A_\varphi(\vartheta_0) + \delta A_\varphi)(\dot{\varphi}_0 + \delta\dot{\varphi}) dt \\ &\approx \gamma^{(0)} + \frac{2\pi}{T} \int_0^T \delta A_\varphi dt + A_\varphi(\vartheta_0) \delta\dot{\varphi}(T) \\ &= \gamma^{(0)} - \frac{\pi}{T} \int_0^T \sin \vartheta_0 \delta\vartheta dt + A_\varphi(\vartheta_0) (\delta\varphi(T) - \delta\varphi(0)).\end{aligned}$$

The last term gives a contribution if $K(T) \neq 0$. Then, the definition of the non-cyclic geometric phase by Samuel and Bhandari (1988) should be used. In this case, the last term vanishes under the assumption $K(0) = 0$. In order to compute the geometric phase $\gamma \equiv \gamma_0 + \delta\gamma$, we wish to express the fluctuations $\delta\vartheta$ in terms of the noise applied in radial direction $\delta\rho$ and in azimuthal direction $\delta\varphi$. To this effect, we go to cylindrical coordinates:

$$\mathbf{B} = (\rho_0 \cos \varphi_0, \rho_0 \sin \varphi_0, z_0),$$

and $\vartheta_0 = \arctan(\rho_0/z_0)$. Also,

$$\delta\vartheta = \frac{\partial\vartheta}{\partial\rho} \delta\rho = \frac{z}{B^2} \delta\rho \approx \frac{\cos\vartheta_0}{B} \delta\rho,$$

where we have defined $B = |\mathbf{B}|$. Then, assuming that the fluctuations in radial direction are described by an Ornstein-Uhlenbeck process with bandwidth Γ_ρ and variance σ_ρ (see app. B), the average of the fluctuations is

$$\langle \delta\vartheta \delta\vartheta' \rangle = \frac{\cos\vartheta_0}{B} \langle \delta\rho \delta\rho' \rangle = \frac{\cos\vartheta_0}{B} \sigma_\rho^2 e^{-\Gamma_\rho |t-t'|}.$$

Since $\langle \delta\gamma \rangle \propto \langle \delta\rho \rangle = 0$, the variance $\sigma_\gamma^2 = \langle (\delta\gamma)^2 \rangle - \langle \delta\gamma \rangle^2$ of the geometric phase is

$$\begin{aligned}\sigma_\gamma^2 &= \left(\frac{\pi \sin \vartheta_0}{T} \right)^2 \int_0^T dt \int_0^T dt' \langle \delta\vartheta \delta\vartheta' \rangle \\ &= 2\sigma_\rho^2 \left(\frac{\pi \cos \vartheta_0 \sin \vartheta_0}{B} \right)^2 \frac{\Gamma_\rho T - 1 + e^{-\Gamma_\rho T}}{(\Gamma_\rho T)^2}.\end{aligned}\quad (4.2)$$

From eq. (4.2), it appears that the variance vanishes for $\theta_0 \in \{0, \pi\}$, and that the geometric phase is insensitive to in-plane noise at these two points: when $\theta_0 = 0$, the geometric phase vanishes, and when $\theta_0 = \pi/2$, the solid angle is $A = 2\pi$, no matter the path.

The effect of noise on the dynamic phase is found in a similar way. To compute the dynamic phase, we assume $\mathbf{B} = (0, 0, B_0)$ and write $\mathbf{K} = (K_x, K_y, K_z)$. Seeing that

$$\langle H \rangle_{|1\rangle} = B/2 + \mathbf{B} \cdot \mathbf{K}/2B$$

and that $\langle H \rangle_{|0\rangle} = -\langle H \rangle_{|1\rangle}$, the dynamical phase is

$$\delta = \delta_0 + \delta\delta = \int_0^T (\langle H \rangle_{|1\rangle} - \langle H \rangle_{|0\rangle}) dt = BT + \int_0^T \frac{\mathbf{B} \cdot \mathbf{K}}{B} dt.\quad (4.3)$$

To compute $\delta\delta$ for the noise here, we compute $K_i = \frac{\partial B_i}{\partial \varphi} + \frac{\partial B_i}{\partial \rho} + \frac{\partial B_i}{\partial z}$ for $i = \varphi, \vartheta, \rho$ and find $\mathbf{K} = (-\rho \sin \varphi d\varphi + \cos \varphi d\rho, \rho \cos \varphi d\varphi + \sin \varphi d\rho, 0)$. Thus,

$$\delta\delta = \int_0^T \sin \vartheta_0 d\rho dt.$$

The variance $\sigma_\delta^2 = \langle (\delta\delta)^2 \rangle - \langle \delta\delta \rangle^2$ evaluates to

$$\begin{aligned} (\sigma_\delta)^2 &= (\sin \vartheta_0)^2 \int_0^T dt \int_0^T dt' \langle \delta\rho \delta\rho' \rangle \\ &= 2\sigma_\rho^2 (\sin \vartheta_0)^2 \frac{\Gamma_\rho T - 1 + e^{\Gamma_\rho T}}{\Gamma_\rho^2}. \end{aligned} \quad (4.4)$$

Note that while $\sigma_\gamma^2 \propto 1/T$, σ_δ^2 is proportional to T . With longer evolution times, the geometric phase rids itself of the influence of noise, while the dynamic phase completely decoheres.

4.1.2 Noise-induced dephasing

The density matrix of a qubit state allows us to see what dephasing is induced by the variance in the acquired phase during a Ramsey-type interferometric experiment (see also sec. 3.1. Starting with an arbitrary state $|\Psi\rangle = a|0\rangle + b|1\rangle$, the state after the adiabatic and cyclic evolution is $|\Psi'\rangle = ae^{i\alpha}|0\rangle + be^{-i\alpha}|1\rangle$, with α being the acquired phase (geometric and/or dynamic). Depending on whether there is noise or not, the phase is distributed differently.

Phase in absence of noise

When there is no noise, the phase is peaked at a value α_0 :

$$P(\alpha) = \delta(\alpha - \alpha_0). \quad (4.5)$$

The density matrix describing the state is found by averaging $|\Psi'\rangle\langle\Psi'|$ weighted with the distribution $P(\alpha)$:

$$\rho = \int_{-\infty}^{\infty} |\Psi'\rangle\langle\Psi'| P(\alpha) d\alpha = \begin{pmatrix} |b|^2 & e^{2i\alpha_0} a\bar{b} \\ e^{-2i\alpha_0} \bar{a}b & |a|^2 \end{pmatrix}.$$

Therefore, the expectation values of the Pauli operators are

$$\langle X \rangle = 2 \operatorname{Re} \left(e^{2i\alpha_0} a\bar{b} \right), \quad \text{and} \quad \langle Y \rangle = -2 \operatorname{Im} \left(e^{2i\alpha_0} a\bar{b} \right),$$

and the coherence is

$$v_0 = \sqrt{\langle X \rangle^2 + \langle Y \rangle^2} = 2|ab|. \quad (4.6)$$

Phase in presence of noise

When there is noise, the phase is gaussian distributed

$$P(\alpha) = \frac{1}{\sqrt{2\pi\sigma^2}} \exp\left(-\frac{(\alpha - \alpha_0)^2}{2\sigma^2}\right).$$

with a variance σ^2 (given by eq. (4.4) or eq. (4.2)) around a mean α_0 . The density matrix follows as

$$\rho = \int_{-\infty}^{\infty} |\Phi'\rangle \langle \Phi'| P(\alpha) d\alpha = \begin{pmatrix} |b|^2 & e^{-2\sigma^2} e^{2i\alpha_0} a\bar{b} \\ e^{-2\sigma^2} e^{-2i\alpha_0} \bar{a}b & |a|^2 \end{pmatrix}$$

because $\int_{-\infty}^{\infty} e^{2i\alpha} P(\alpha) = e^{-2\sigma^2} e^{2i\alpha_0}$. With

$$\langle X \rangle = 2e^{-2\sigma^2} \operatorname{Re}\left(e^{2i\alpha} a\bar{b}\right), \quad \text{and} \quad \langle Y \rangle = -2e^{-2\sigma^2} \operatorname{Im}\left(e^{2i\alpha} a\bar{b}\right),$$

the coherence is

$$\nu = e^{-2\sigma^2} \cdot 2|ab| = e^{-2\sigma^2} \nu_0. \quad (4.7)$$

It is thus reduced by a factor $e^{-2\sigma^2}$ in comparison to the phase not affected by noise, eq. (4.6). Note that eq. (4.6) can also be obtained from eq. (4.7) in the limit $\sigma \rightarrow 0$. From eq. (4.6), it also appears that the coherence is maximal when one chooses $a = \pm 1/\sqrt{2}$ and $b = \pm 1/\sqrt{2}$. Then, $\nu = 1$.

When performing a spin-echo experiment, where the evolution is repeated a second time mirrored around the π -pulse, the standard deviation is doubled due to the second exposition to noise, $\sigma \rightarrow 2\sigma$ (Filipp, 2006, ch. 5.3). Therefore

$$\nu = e^{-2(2\sigma)^2} \cdot 2|ab| = e^{-8\sigma^2} \nu_0. \quad (4.8)$$

Comparing eq. (4.8) and eq. (4.7), it appears that the ratio of the coherences after a Ramsey experiment (with one exposition to noise) and a spin-echo experiment (with two expositions to noise) is $e^{-6\sigma^2}$.

4.2 Experiments

4.2.1 Experimental idea

To study the influence of noise on the Berry phase and on the dynamic phase of a spin one-half particle, we use a scheme similar to the experiments presented in ch. 3: the two lowest energy levels of a transmon dispersively coupled to a resonator serve as a qubit, and a classical drive provides an effective magnetic field (see sec. 2.5.3). However, our findings are independent of the specific implementation, and apply to any system in which Berry phases can be observed. The system is effectively described by the familiar Hamiltonian of a spin one-half particle in a magnetic field,

$$H = \hbar \boldsymbol{\sigma} \cdot \mathbf{B}/2, \quad (4.9)$$

As in ch. 3, we consider an effective field evolving along a circular path with radius $B_\rho = \sqrt{B_x^2 + B_y^2}$ at constant B_z and with precession period T (Fig. 4.1). This path encloses a

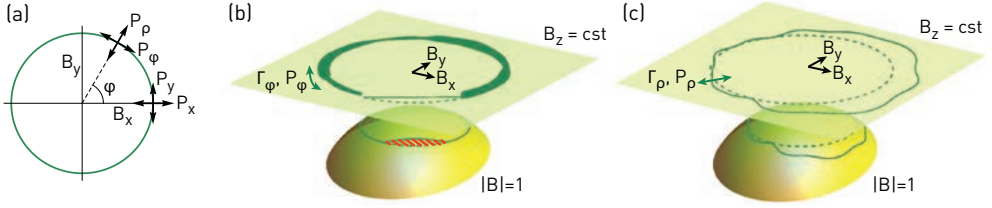


Figure 4.1: Fluctuating magnetic fields. (a) The path of the effective magnetic field (green line) describes a circle in the B_x - B_y -plane at constant B_z . Noise in x and y directions with noise powers P_x and P_y can be decomposed into noise in ρ and φ directions with noise powers P_ρ and P_φ . (b,c) The path of the effective field without noise (dashed green lines lying in the plane with constant B_z) is drawn alongside the same path exposed to two kinds of noise (solid green lines): angular noise in (b), where the velocity of precession is proportional to line thickness, and radial noise in (c). The projection of the paths on the unit sphere $|\mathbf{B}| = 1$ is also shown. In (b), the difference in solid angle due to non-cyclic evolution is highlighted in red.

solid angle $A = 2\pi(1 - \cos \vartheta)$, with the polar angle $\vartheta = \arctan(B_\rho/B_z)$, so the ground $|0\rangle$ and excited $|1\rangle$ state of the qubit acquire a Berry phase $\gamma_0 \approx \pm A/2$ if the evolution is adiabatic.

In experimental situations, the field components fluctuate about their mean values and these fluctuations induce dephasing. Changes in field strength will cause dynamic dephasing, while modifications in solid angle will cause dephasing due to fluctuations in the Berry phase¹. Clearly, noise directed in azimuthal direction (angular noise, Fig. 4.1(b)) does not modify the solid angle and thus, no such dephasing is expected. In contrast, noise directed in radial direction (radial noise, Fig. 4.1(c)) will induce such dephasing. By artificially adding noise in radial (or azimuthal) direction to the field in our experiment, we are thus able to maximize (or minimize) dephasing originating in fluctuations of the Berry phase and investigate its properties for different angles ϑ and noise powers.

To model realistic uncorrelated noise with a given bandwidth, we generate fluctuations conforming to Ornstein-Uhlenbeck processes, i.e. stationary, gaussian and Markovian noise processes with a Lorentzian spectrum of bandwidth Γ_i and noise power P_i ($i = \rho, \varphi$). See app. B for details.

In the experiment, the precession frequency and the noise bandwidth are chosen to be small compared to the amplitude $B = |\mathbf{B}|$ of the effective field, i.e. $1/T, \Gamma_i \ll B$, to study adiabatic processes. In this case, the derivation in sec. 4.1 of the variance of the geometric phase from a perturbative treatment is valid. From eq. (4.2), it is clear that to first order only variations $\delta\rho$ in radial direction contribute to σ_γ^2 .

4.2.2 System parameters

The qubit is manipulated using microwave fields applied via a capacitively coupled charge bias line. Using spectroscopic measurements, we have determined the maximum Josephson energy $E_{J,\max}/h = 11.4\text{GHz}$, the charging energy $E_C/h = 0.26\text{GHz}$ and the coupling strength $g/2\pi = 360\text{MHz}$ of the qubit to the resonator. The experiments are performed at a qubit transition frequency $\omega_{01}/2\pi = 4.68\text{GHz}$, with an energy relaxation time $T_1 = 2.65\mu\text{s}$, a phase coherence time $T_2 = 1.35\mu\text{s}$ and a spin-echo phase coherence time

¹Although this kind of dephasing stems from fluctuations in the Berry phase, it is itself not geometric. We discuss geometric dephasing in ch. 5.

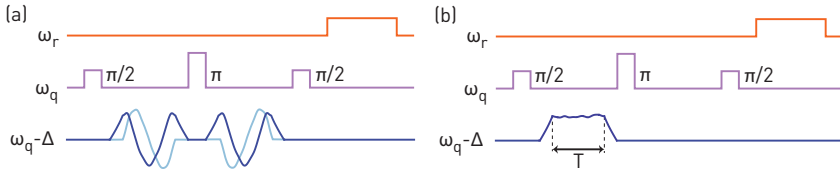


Figure 4.2: Sketches of the pulse schemes (amplitude vs. time) used to measure (a) Berry and (b) dynamic phases with radial noise. Detuned pulses applied along the X - and Y -axis are shown in blue and light blue, respectively. The readout pulse concludes the sequence after $t \approx 400$ ns.

$T_{2,\text{echo}} = 2.15 \mu\text{s}$. The sample is operated in a dilution refrigerator at a base temperature of 20 mK. The fundamental mode of the resonator being at $\omega_r/2\pi = 6.600$ GHz, the qubit is in dispersive regime and the Hamiltonian eq. (4.9) is applicable. The effective magnetic field is $\mathbf{B} = (\Omega \cos \varphi, \Omega \sin \varphi, \Delta)$. It is determined by amplitude Ω , phase angle φ and detuning $\Delta = \omega_{01} - \omega_d$ of the drive.

4.2.3 Measurement scheme

As in ch. 3, a Ramsey-type interferometric sequence containing a spin-echo pulse to cancel the dynamic phase is employed to measure the Berry phase acquired by the two-level system (Fig. 4.2(a)). A series of resonant pulses (of frequency ω_{01}) implement the spin-echo sequence, while off-resonant pulses (of frequency $\omega_d = \omega_{01} - \Delta$) guide its state adiabatically along the paths shown in Fig. 4.1(b,c).

All presented Berry phases are measured at a detuning $\Delta = -50$ MHz. The acquired Berry phase is varied from 0 rad to 6.9 rad by increasing the solid angle A via the drive amplitude Ω . The strength of the noise is quantified by the normalized noise amplitude $s_\rho = \sqrt{P_\rho}/B_\rho$ for radial noise and by $s_\varphi = \sqrt{P_\varphi}$ for angular noise. These definitions ensure that fluctuations in radial or azimuthal directions have identical amplitudes if $s_\rho = s_\varphi$.

The phases with noise are obtained by repeating the experiment with different noise patterns. Identical noise patterns are used before and after the spin echo pulse to ensure cancellation of the dynamical phase. The pulse sequences, consisting of two intermediate-frequency quadratures x and y , are numerically created: noise conforming to an Ornstein-Uhlenbeck process is generated and added to the pulses describing the noiseless evolution of the field (see app. B for details). An arbitrary waveform generator synthesizes these quadratures, which are upconverted to a microwave-frequency signal using an in-phase/quadrature mixer. After the manipulation sequence, the state of the qubit is determined in a dispersive readout (see sec. 2.5.1) through the resonator and reconstructed using state tomography (Paris and Řeháček, 2004). To overcome noise in the detection, each individual noise realization is measured 10^6 times.

4.2.4 Histograms

Histograms of the measured Berry phases for four solid angles are shown in Fig. 4.3(a,c). For radial noise, the Berry phases of the individual noise realizations have—as discussed above—a gaussian distribution with a mean equal to the Berry phase γ_0 without noise. For angular noise, we observe that the widths of the phase distributions are, as expected, almost zero. The expectation values of the Bloch-vector components $\langle X \rangle$ and $\langle Y \rangle$ for

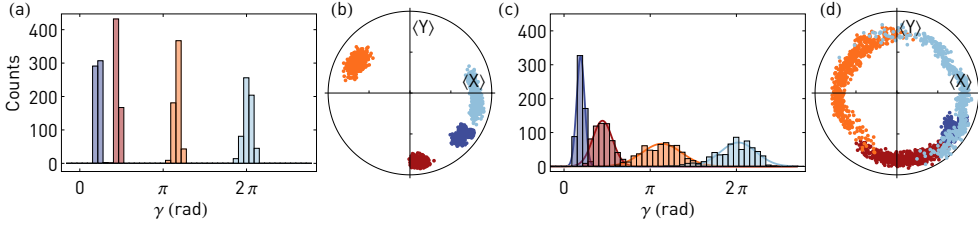


Figure 4.3: Measurements of the geometric phase in the presence of noise. (a) Histograms of Berry phases and (b) measured expectation values $\langle X \rangle$, $\langle Y \rangle$ of 600 realizations of angular noise for each solid angle $A = \pi/16, 3\pi/16, 8\pi/16$ and $15\pi/16$ (indicated in blue, red, orange, light blue). Fits of a gaussian to the measured histograms are also shown in (a). The circle in (b) indicates unit coherence. (c,d) Measurements analogous to panels (a,b) for radial noise.

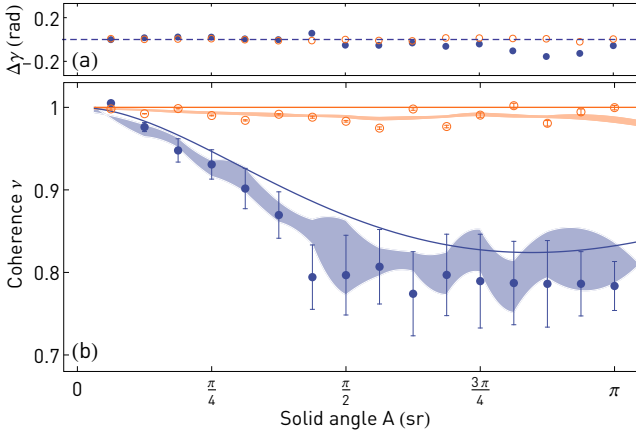


Figure 4.4: Measurements of the geometric phase in the presence of noise. (a,b) Coherence ν and phase difference $\Delta\gamma$ as a function of solid angle A for radial noise (blue dots) and angular noise (orange circles). The experimental data points are shown alongside the theory curve (solid lines) and the results from numerical simulations (the shaded area indicates the standard deviation about the mean). Parameters: noise bandwidth $\Gamma_i = 10\text{MHz}$, normalized noise amplitudes $s_i = 1/15$ and evolution time $T = 100\text{ns}$.

individual noise realizations are distributed on the equatorial plane of the Bloch sphere (Fig. 4.3(b,d)), reflecting the spread of the measured phases. They lie on a circle with radius $\nu_0 \approx 0.80 < 1$, which is a result of the intrinsic noise present in the system.

4.2.5 Dependence of coherence on solid angle

Distributions akin to those shown in Fig. 4.3(b,d) are used to compute the coherence eq. (4.8) $\nu = \sqrt{\langle X \rangle^2 + \langle Y \rangle^2} = e^{-8\sigma_\gamma^2}$ as a function of solid angle (Fig. 4.4(b)). Intrinsic noise is present, but not relevant for discussing the influence of the fluctuating effective magnetic field. How to eliminate its effect on the measured coherences? Assuming that intrinsic noise causes a reduction in coherence by a factor ν_{int} , the coherence measured after a spin-echo sequence is $\nu \nu_{\text{int}}$ with applied noise and ν_{int} without applied noise. By taking the ratio of these, the effect of the added noise can be isolated. Therefore, for every data point of coherence shown, a reference measurement without noise is performed, and the intrinsic noise is divided out.

We observe that for radial noise the coherence decreases and then stabilizes as a function of solid angle, while it is approximately unity for angular noise. This is an immediate

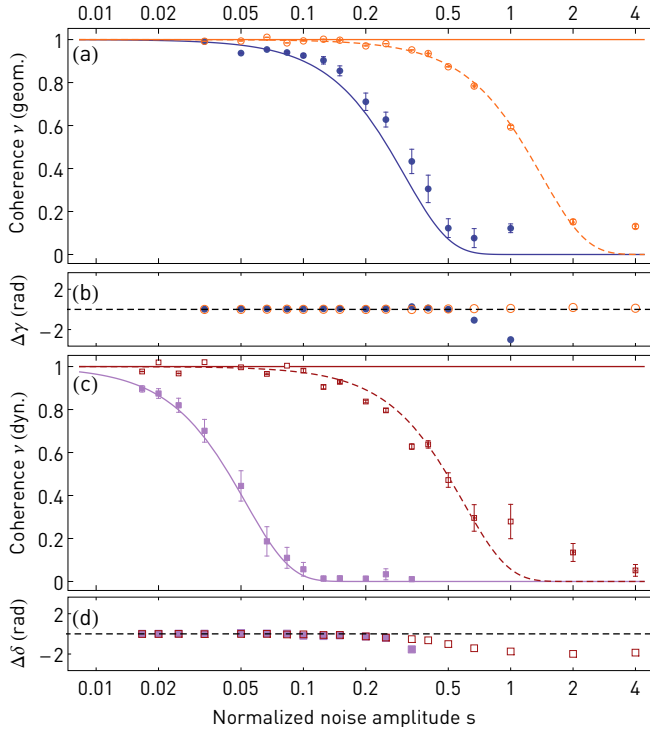


Figure 4.5: Experimentally measured coherence ν of the Berry phase and phase difference $\Delta\gamma = \gamma - \gamma_0$ as a function of normalized noise amplitude s for radial noise (filled blue circles) and angular noise (open orange circles), plotted on a logarithmic scale. For every value of s , 300 noise realizations were measured with noise bandwidth $\Gamma = 10\text{MHz}$ at solid angle $A = 7\pi/16$ and evolution time $T = 100\text{ns}$. The continuous line is computed from eq. (4.2). The dashed line is a fit to the function $\exp(-(4as)^2/2)$ with fitting parameter $a = 0.25 \pm 0.01$. (c,d) Quantities analogous to panels (a,b) but for the dynamic phase, with $\Delta\delta = \delta - \delta_0$ and fitting parameter $a = 0.60 \pm 0.03$.

consequence of the nature of the Berry phase: radial noise modifies the solid angle A causing dephasing and a decrease in coherence. In contrast, angular noise hardly affects A .

For both kinds of noise, the difference $\Delta\gamma = \gamma - \gamma_0 \lesssim 0.2$ rad in the mean Berry phase with and without noise is very small (Fig. 4.4(a)). The measured coherences agree well with equation (4.2) and numerical results obtained by solving the unitary dynamics of the Hamiltonian in eq. (4.9). The measured Berry phase γ_0 itself (not shown) agrees well with the prediction for a transmon-type qubit (see ch. 3), with a discrepancy of 0.20 rad across all solid angles for the data in Fig. 4.4(a,b).

4.2.6 Varying the noise amplitude

To illustrate the effects of noise quantitatively, both the Berry phase and the dynamic phase are measured for varying noise amplitudes s . For the Berry phase, we observe that the coherence follows the expected dependence $e^{-(4as)^2/2}$ for radial noise (Fig. 4.5(c,e)) and that angular noise has a lesser effect on the coherence than radial noise. For both types of noise, and for normalized noise amplitudes $\lesssim 0.5$, the Berry phase with and without noise have the same value.

4.2.7 Coherence of the dynamic phase

Just as for the Berry phase, the coherence of the dynamic phase σ_δ^2 in eq. (4.4) only depends on radial variations if the noise amplitude is small. Due to these fluctuations, the

dynamic phase is gaussian distributed around the noiseless dynamic phase δ_0 . Noise in azimuthal direction does not change the magnitude of the field and hence does not cause fluctuations in the dynamic phase.

The coherence of the dynamic phase was recorded using a spin-echo sequence containing a single off-resonant pulse (Fig. 4.2b), and therefore its variance was scaled by a factor to allow for direct comparison with the Berry phase. From Fig. 4.5(c), it is evident that the coherence of the dynamic phase starts decreasing at weaker noise amplitudes than the Berry phase, demonstrating the superior noise resilience of the Berry phase. It is also observed that the mean dynamic phase δ starts deviating from δ_0 already at $s \approx 0.2$. The measured coherences for both dynamic and Berry phase are in very good agreement with the predictions based on eq. (4.2) and eq. (4.4) for radial noise. For angular noise, fits to $e^{-(4as)^2/2}$ agree with the observed behaviour of the coherences. Indeed, while according to eqs. (4.2) and (4.4) the coherences are expected to be insensitive to angular noise to first order, non-adiabatic and higher-order effects (Lupo and Aniello, 2009) still affect the coherences. In particular, the evolution of the field can be non-cyclic (Samuel and Bhandari, 1988), which adds a small contribution to dephasing (see Fig. 4.1(b) and De Chiara and Palma (2003)).

4.2.8 Comparison of dynamic and geometric phase

Finally, we directly compare the coherence of dynamic and Berry phases in the presence of radial noise. The Berry phase γ is recorded at a solid angle $A = 0.37\pi$, where the effect of noise on γ is strongest. For long evolution times T , the Berry phase is more resilient against radial noise than the dynamic phase because its variance σ_γ^2 decreases with evolution time (Filipp et al., 2009), whereas the variance of the dynamic phase σ_δ^2 grows linearly in evolution time (cf. eq. (4.2) and eq. (4.4), as well as Fig. 4.6). Both phases have equal coherences when $\sigma_\gamma^2 = \sigma_\delta^2$, i.e.

$$T = \pi \cos(\vartheta) / B, \quad (4.10)$$

and the dynamic phase is more coherent than the Berry phase only for even shorter evolution times ($T < 13$ ns according to equation (4.10) and $T < 20$ ns according to the experimental data in Fig. 4.6). Note that the variance of the dynamic phase is independent of the value of the dynamic phase. This is why it was recorded using the same drive amplitudes as for the Berry phase gates. The data in Fig. 4.6 agrees with calculations. The standard deviation σ_δ of the dynamic phase starts differing significantly from computed predictions at evolution times $T \gtrsim 100$ ns, when the recorded phases are spread across 2π and their variance saturates.

4.3 Conclusion

In conclusion, we have demonstrated that the Berry phase is less affected by noise along the path in parameter space than by noise perpendicular to it. Given a system with known noise properties, this can potentially be exploited to realize noise-resilient geometric operations. Both kinds of noise leave the mean of the geometric phase unchanged. Shifts of the mean Berry phase are theoretically expected (Whitney et al., 2005), but are beyond

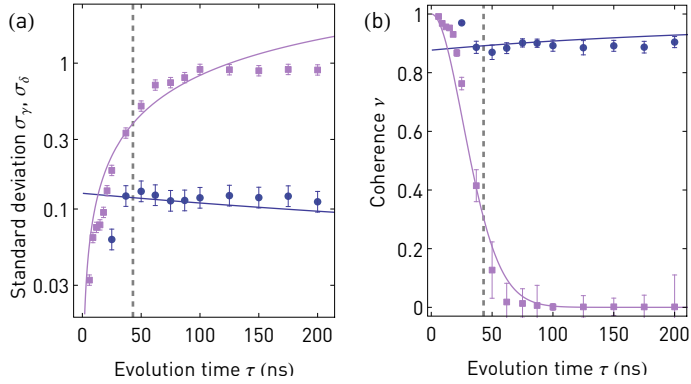


Figure 4.6: (a) Standard deviation σ_γ of the Berry phase (blue circles) and σ_δ of the dynamic phase (purple squares) as a function of evolution time T , based on 300 noise realizations with $\Gamma = 10\text{MHz}$ and $s_\rho = 1/15$. The solid lines result from calculations based on eq. (4.2) and eq. (4.4). The dashed grey line approximately separates the non-adiabatic from the adiabatic regime. (b) Coherence ν versus evolution time T of the Berry phase (blue circles) and the dynamic phase (purple squares).

current experimental precision. We have also shown that the geometric phase is less affected by decoherence than the dynamic phase when evolving adiabatically (evolution times $\gtrsim 1/B$). Our results illustrate fundamental properties of the geometric phase and serve as a stepping-stone for further investigations of geometric phases as a resource for quantum computation (Rong et al., 2011) or for precision measurements (Mur-Petit et al., 2012; Martín-Martínez et al., 2013).

The analysis presented here, as well as the work by De Chiara and Palma (2003), consider a quantum system evolving unitarily. Lombardo and Villar (2014) study the Berry phase under the influence of noise in the case of nonunitary evolution. In keeping with literature (Leek et al., 2007; Filipp et al., 2009), they find that the effect of weak noise on the geometric phase is almost imperceptible. Li and Shi (2013) consider the more general case of non-Markovian noise and find that, as in the Markovian case, the coherence of the Berry phase is not lowered for adiabatic high-frequency noise.

GEOMETRIC DEPHASING

Although the dephasing observed in the previous chapter originates from fluctuations in the Berry phase, it is itself *not* geometric. The concept of geometric dephasing has been introduced by Whitney et al. (2005). Indeed, decoherence in quantum systems stems not only from the stochastic evolution of the dynamical phase of the system's wave function (dynamical dephasing), but also from geometric effects.

In this chapter, we consider a qubit in a noisy environment and find that the measured dephasing is partly of geometric nature. As in ch. 4, the two lowest energy levels of a transmon dispersively coupled to a resonator serve as a qubit, and a microwave tone provides an effective magnetic field $\mathbf{B} = (\Omega_x, \Omega_y, \Delta)$ precessing at a rate $\omega_B > 0$ slow enough for the qubit to evolve adiabatically. The Hamiltonian of the driven qubit in the rotating frame is, as usual,

$$H = \hbar \boldsymbol{\sigma} \cdot \mathbf{B}/2. \quad (5.1)$$

where $\boldsymbol{\sigma} = (X, Y, Z)$ are the Pauli matrices.

We find that with stochastic Gaussian noise on the effective magnetic field, the length $v = \sqrt{\langle X \rangle^2 + \langle Y \rangle^2 + \langle Z \rangle^2}$ of the qubit state vector is given by

$$v = \exp \left\{ -D(T) \left(a + b \operatorname{sgn}(n) \omega_B + c \omega_B^2 + \dots \right) / 2 \right\}. \quad (5.2)$$

In this equation, $T \equiv 2\pi|n|/\omega_B$ is the duration of the time evolution, $n \in \mathbb{Z}$ is the oriented number of loops of the magnetic field, $2\pi/\omega_B$ is the time needed for a single loop, and $D(T)$ characterizes the spectral properties of the noise. The first term in eq. (5.2) is independent of ω_B and represents dynamic dephasing. The second term is proportional to $\operatorname{sgn}(n)\omega_B$ and represents geometric dephasing. The third term goes as ω_B^2 and stands for non-geometric non-adiabatic dephasing. It is especially noteworthy that the second term can either increase or decrease the total dephasing, depending on the sign of n . This

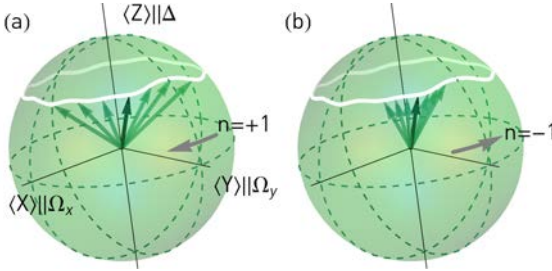


Figure 5.1: Bloch vectors (green arrows) describing the qubit state after evolving adiabatically in an precessing noisy magnetic field. When the qubit state evolves adiabatically, its Hilbert space can be identified with the parameter space of the Hamiltonian, viz. the three-dimensional effective magnetic field. The magnetic field (white line) follows a closed loop n times. In (a), the number of loops is $n = +1$, in (b) it is $n = -1$. Due to geometric dephasing, the Bloch vectors are fanned out more in (a) than in (b).

makes the geometric nature of this term explicit (see Fig. 5.1). The contributions to dephasing stemming from the first and the third term are independent on the sign of n and are therefore not geometric.

5.1 Experiment

5.1.1 System and setup

The sample (Fig. 5.2) is an artificial atom of the transmon type coupled to a coplanar waveguide resonator (CPW; Koch et al. (2007)). A miniature coil mounted below the sample is used to set the lowest transition of the transmon to a frequency $\omega_{01} = 7.0335$ GHz. Its coupling to the resonator can be tuned using a static bias current applied to a flux line (Srinivasan et al., 2011). Here, it is tuned to $g/2\pi = 38$ MHz at the outset of the experiment and then kept constant. The artificial atom has an anharmonicity of $\alpha/2\pi = 90$ MHz.

The fundamental mode of the resonator is at a frequency $\omega_r/2\pi = 7.347$ GHz and has a loaded quality factor of $Q = 3600$, so we can readily dispersively read out the quantum state of the artificial atom by monitoring the transmission of a rf-signal at frequency ω_r through the resonator ($g/\Delta = 0.12$; see Bianchetti et al. (2009) and also sec. 2.5.1). The input port of the resonator is coupled less strongly to the transmission line than the output port to increase the SNR of the readout.

Via two circulators and a directional coupler, the output signal of the resonator goes to an amplifier based on a Josephson parametric dimer (JPD, see Eichler et al. (2014) and also sec. 2.5.2), with a gain of 18.4 dB at a bandwidth of 28 MHz centred around 7.348 GHz. The first circulator prevents reflected signals in the output line from leaking into the cavity; the second circulator separates the output of the JPD amplifier from the input. The directional coupler is used to operate the JPD amplifier: a tone is split, the first half pumps the JPD and the second is phase-shifted and attenuated to cancel the pump tone in the amplified signal. The pump tone was at $\omega_p = 7.564$ GHz, detuned 217 MHz from the resonator.

The signal is then bandpass filtered (4 to 8 GHz) and amplified with a high-electron-mobility transistor (HEMT) amplifier providing 35 dB of gain. At room temperature, the signal is amplified further, filtered and downconverted to 25 MHz before it is digitized at a rate of 100 MS/s and analysed with a field-programmable gate array (FPGA).

We use direct modulation of an in-phase/quadrature mixer to generate the microwave pulses for qubit state manipulation. The pulses are applied through a capacitively coupled

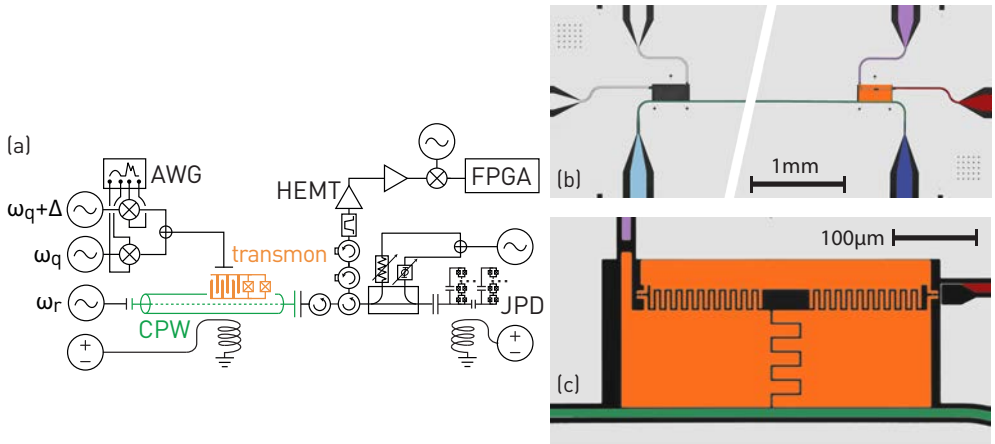


Figure 5.2: (a) Micrograph of the sample. Resonator input (dark blue), resonator output (light blue), resonator (green), charge line (red), flux line (violet) and artificial atom (orange), and zoom on the artificial atom (inset). (b) Schematic of the measurement setup. See text for details.

charge bias line. The I and Q quadratures are synthesized with an arbitrary waveform generator (AWG). The pulses resonant with the qubit transition have a gaussian envelope with a standard deviation of $\epsilon = 10$ ns. They are symmetrically truncated to a length of 4σ . Measuring Rabi oscillations allows us to extract the amplitudes of π - and $\pi/2$ -pulses. We perform Ramsey interferometry experiments to calibrate the frequency of these pulses, and also serve to extract the dephasing time $T_2^* = 770$ ns and echo-decay-time $T_2^{\text{echo}} = 1520$ ns of the ω_{01} -transition. Its lifetime is found to be $T_1 = 1330$ ns.

5.1.2 Experimental idea

To get rid of the large dynamical phase the qubit acquires during evolution, a spin-echo technique is employed. Note that geometric dephasing can be present as soon as the qubit state traverses a path in its projective Hilbert space—the spin-echo is merely a tool used in our measurement. We consider two alternative echo protocols. In the first protocol, which is often used to observe the Berry phase (Jones et al. (2000), Leek et al. (2007); see also ch. 3 and ch. 4), the direction of the conical motion of the magnetic field is reversed in the second half of the echo sequence. We therefore call this protocol R (for ‘reversed’). From now on, n denotes the number of loops in the first half of the echo sequence. The second protocol is a ‘total’ spin echo, in which the direction of precession of the magnetic field is preserved in the second half of the spin echo sequence. We refer to it as protocol P (for ‘preserved’). To illustrate the protocols, schematics of the pulse sequences are shown in Fig. 5.3.

As in ch. 4, artificial noise conforming to an Ornstein-Uhlenbeck process (see app. B) with intensity σ^2 and correlation time $1/\Gamma$ is added to the drive to mimic noise in the magnetic field. We consider fluctuations $\delta\varphi$ in angular direction $\delta\Omega$ and in radial direction, so that $\Omega(t) = \Omega_0 + \delta\Omega$ and $\varphi(t) = (n/|n|)\omega_B t + \delta\varphi$. In our setup, these correspond to amplitude and phase noise in the signal driving the qubit. The time correlations of the artificial

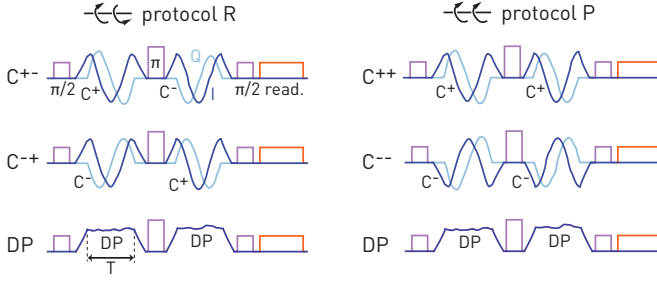


Figure 5.3: Pulse sequences for protocols R and P. The π - and $\pi/2$ -pulses implementing the spin-echo are on resonance with the qubit transition frequency ω_{01} (purple). At the end of the sequence, the state of the qubit is read out by applying a tone at frequency ω_r (orange). The components Ω_x and Ω_y of the magnetic field are shown in dark and light blue. Δ is kept constant and is not shown. The labels ‘+’ and ‘-’ in C^+ and C^- denote $\text{sgn}(n)$, the orientation of the loops of the magnetic field, i.e. its direction of precession. The label D.P. denotes a magnetic field which does not precess ($\omega_B = 0$). In protocol R, the direction of precession is inverted during the second window of the echo, leading to pulse sequences C^{+-} or C^{-+} . In protocol P, the direction of precession is preserved, giving C^{++} or C^{--} . In the pulse sequences ‘R, D.P.’ and ‘P, D.P.’ (which are identical), the qubit acquires only dynamic phase during the off-resonant evolution. In all other sequences, the qubit acquires both dynamic and geometric phase.

noise may be controlled, in particular those between the first time window, $0 < t < T$, and the second time window, $T < t < 2T$. For convenience, we let $\delta\Omega_1(t) \equiv \delta\Omega(t)$ and $\delta\Omega_2(t) \equiv \delta\Omega(t + T)$.

Four types of time-correlations of the noise are considered. First, perfectly correlated noise ($\delta\Omega_1(t) = \delta\Omega_2(t)$), when the correlation time is much larger than the time-scale of the experiment. Second, anticorrelated noise ($\delta\Omega_1(t) = -\delta\Omega_2(t)$). Third, uncorrelated noise, when correlation times are shorter than the spin-echo timescale ($\langle \delta\Omega_1(t_1)\delta\Omega_2(t_2) \rangle = 0$ and $\langle \delta\Omega_1(t_1)\delta\Omega_1(t_2) \rangle = \langle \delta\Omega_2(t_1)\delta\Omega_2(t_2) \rangle$), typical e.g. for white noise (Ithier et al., 2005; Paladino et al., 2014). Fourth, the case with noise in the first window of the echo only ($\delta\Omega_2(t) \equiv 0$), to measure the dephasing experienced by the qubit in a Ramsey experiment.

5.1.3 Experimental results

We now present the experimental results. Phase and coherence of the qubit after the echo sequence have been recorded as a function of solid angle for both protocols. In every measurement, the solid angle is swept from $\pi/16$ sr to $3\pi/4$ sr in steps of $\pi/16$ sr, the normalized noise amplitude is $\sigma / (\Omega_x^2 + \Omega_y^2)^{1/2} = 0.1$, the noise bandwidth $\Gamma = 10$ MHz, the winding number $n = 1$, the precession period $T = 100$ ns (or $T = 160$ ns). There are 400 realizations of noise per data point. The off-resonant pulses have a detuning of $\Delta/2\pi = -35$ MHz, intrinsic dephasing due to a finite decoherence rate of the qubit is calibrated out as in ch. 4, and care is taken that the magnetic field evolves adiabatically (see sec. 5.2.6).

After the pulse sequences of protocol R, the qubit has acquired some geometric phase if $\omega_B \neq 0$. When there is no noise, the measured geometric phases (top row of Fig. 5.4) agree with the theoretical predictions for a weakly anharmonic multi-level system (see ch. 3). Even with noise (middle row of Fig. 5.4), the phases agree, showing that as expected the mean of the geometric phase is not affected if the noise is weak enough (normalized

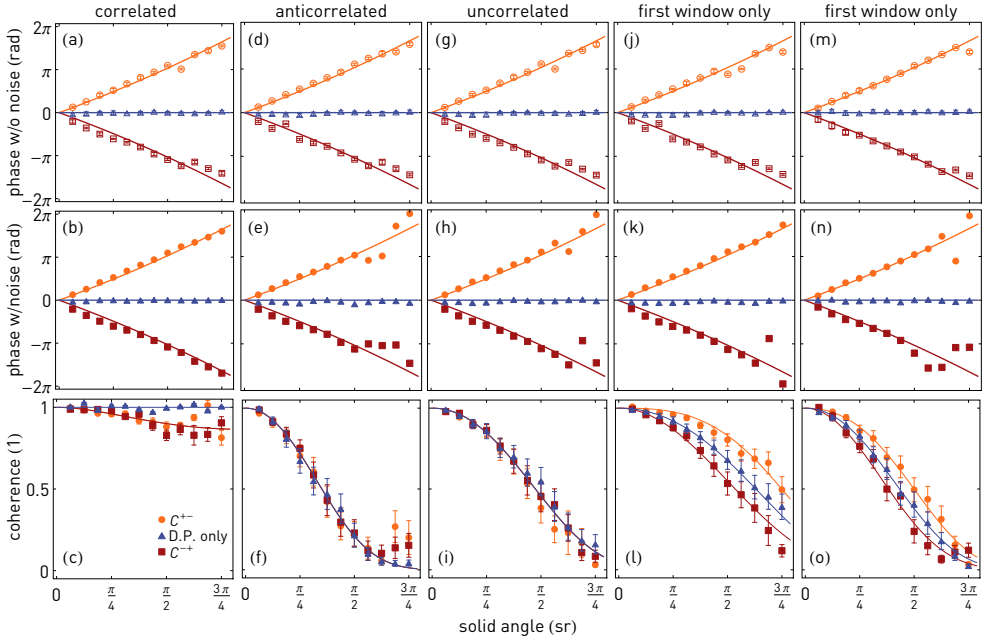


Figure 5.4: (a,b,c) Measured coherence and phase as a function of solid angle for protocol R with correlated noise ($T = 100$ ns). The solid lines are theory curves in panels (a,b) and fits in panel (c). The phase measured without noise in the magnetic field is shown in panel (a). The one with noise is shown in panel (b). (d,e,f) Ditto, but with anticorrelated noise. (g,h,i) Ditto, but with uncorrelated noise. (j,k,l) Ditto, but with noise in the first window only. (m,n,o) Ditto, but with noise in the first window only and $T = 160$ ns.

noise amplitude $\sigma/(\Omega_x^2 + \Omega_y^2)^{1/2} = 0.1 < 0.5$; see ch. 4 for details). However, when noise-induced dephasing becomes so strong that the coherence drops below ≈ 0.2 , the phase can no longer be extracted reliably. At this point, the measured geometric phase starts to deviate from the model. We also note that noise-induced corrections to the geometric phase (Whitney et al., 2005) are small with respect to systematic errors in the measured phase and cannot be resolved.

The bottom row of Fig. 5.4 displays the coherence ν of the qubit as a function of solid angle for protocol R. When there is noise in the first window only (panels (l) and (o)), geometric dephasing is clearly present: depending on the direction of precession $\text{sgn}(n)$, geometric dephasing reinforces or counteracts dynamic dephasing. For other noise correlations (panels (c), (f) and (i)), the observed coherences for C^{+-} and C^{-+} are independent of $\text{sgn}(n)$ and coincide with those for $D.P.$, meaning that the dephasing is purely dynamic. For correlated noise (panel b), non-geometric non-adiabatic dephasing is present as expected for C^{+-} and C^{-+} only. Comparing the measurements with noise in the first window only for different evolution times ($T = 100$ ns in panel h and $T = 160$ ns in panel j), we see that dynamic dephasing is stronger for larger T and that geometric dephasing is present for both cases.

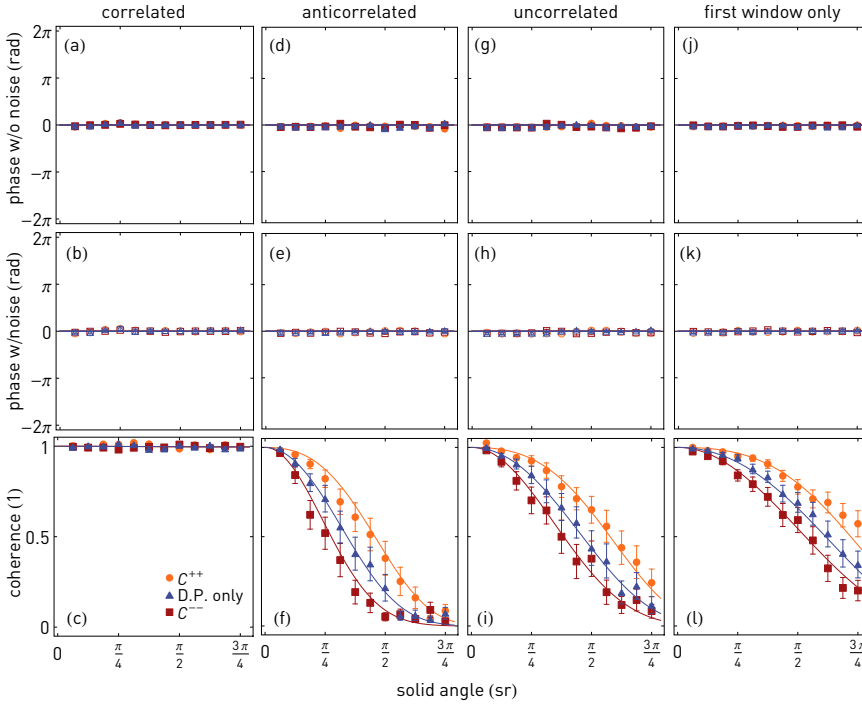


Figure 5.5: This figure is as Fig. 5.4(a-l), but for protocol P. (a,b,c) Measured coherence and phase as a function of solid angle with correlated noise ($T = 100$ ns). The solid lines are theory curves in panels (a,b) and fits in panel (c). The phase measured without noise in the magnetic field is shown in panel (a). The one with noise is shown in panel (b). (d,e,f) Ditto, but with anticorrelated noise. (g,h,i) Ditto, but with uncorrelated noise. (j,k,l) Ditto, but with noise in the first window only.

As for the phase acquired during protocol P, it vanishes not only when there is no noise in the effective magnetic field and but also when there is noise, as supported by the data in the upper and middle rows of Fig. 5.5. Indeed, as far as the phase is concerned, protocol P is a complete echo and no deterministic phase (neither dynamic nor geometric) is acquired.

The data for protocol P (bottom row in Fig. 5.5) show that both dynamic and geometric dephasing is present for all types of noise correlations except for correlated noise. It is noteworthy that there is dephasing even when no phase is acquired. For correlated, the protocol is a perfect spin echo because the effective magnetic field and the noise are identical in both halves. Provided the evolution is adiabatic, no decoherence is to be expected.

5.2 Theory

In this section, the various contributions of the dephasing observed in Fig. 5.4 are quantified. It generalizes the results from sec. 4.2.1, where the coherence of the qubit is studied

for noise perfectly correlated in both halves of the echo. To derive an expression for the coherence ν of the qubit after the echo sequence, we go to a frame rotating at $\omega_d + \omega_B$ by applying the transformation $R = \exp(i\omega_B Z/2)$ to the Hamiltonian eq. (5.1):

$$\tilde{H} = RHR^\dagger + i\dot{R}R^\dagger = \hbar(\Delta - \text{sgn}(n)\omega_B - \delta\dot{\phi})Z/2 + \hbar(\Omega + \delta\Omega)X/2. \quad (5.3)$$

This equation shows that angular noise enters only via $\delta\dot{\phi}$. Its effect on dephasing is suppressed by ω_B^2 at low frequencies and it therefore induces dephasing less efficiently than the radial noise. We have therefore only considered radial fluctuations $\delta\Omega$.

5.2.1 Ramsey experiment

From eq. (5.3) with $\delta\dot{\phi} = 0$, the total relative phase acquired by the eigenstates of the qubit in a Ramsey interferometric experiment in the time interval $[0, T]$ is

$$\gamma = \int_0^T dt \sqrt{(\Delta - \text{sgn}(n)\omega_B)^2 + (\Omega_0 + \delta\Omega(t))^2}. \quad (5.4)$$

Expanding this phase to first order in $\delta\Omega$ and in ω_B gives

$$\gamma = \int_0^T dt \left[\sqrt{\Delta^2 + \Omega_0^2} - \text{sgn}(n)\omega_B \cos\theta - \delta\Omega \sin\theta + \delta\Omega \frac{\text{sgn}(n)\omega_B}{\sqrt{\Delta^2 + \Omega_0^2}} \cos\theta \sin\theta + \dots \right]. \quad (5.5)$$

In the experiment, we measure the expectation value $\langle e^{i\gamma} \rangle$, whose argument is the relative phase between $|0\rangle$ and $|1\rangle$, and whose modulus is the coherence of qubit state vector. Making use of the fact that the phase in the presence of noise follows a gaussian distribution

$$P(\gamma) = \frac{1}{\sqrt{2\pi\langle(\delta\gamma)^2\rangle}} \exp\left(-\frac{(\gamma - \gamma_0)^2}{2\langle(\delta\gamma)^2\rangle}\right)$$

with mean γ_0 and variance $\langle(\delta\gamma)^2\rangle$, we find

$$\langle e^{i\gamma} \rangle = \int_{-\infty}^{\infty} d\gamma P(\gamma) e^{i\gamma} = e^{i\gamma_0} e^{-\frac{1}{2}\langle(\delta\gamma)^2\rangle}.$$

The expectation value of the phase $\langle\gamma\rangle$ is thus equal to

$$\langle\gamma\rangle = \gamma_0 = \int_0^T dt \left(\sqrt{\Delta^2 + \Omega_0^2} - \text{sgn}(n)\omega_B \cos\theta \right),$$

the sum γ_0 of dynamic and geometric phase in absence of noise, viz. the first two terms in eq. (5.5). The coherence is

$$\nu = e^{-\frac{1}{2}\sigma^2}. \quad (5.6)$$

In a next step, the variance $\langle(\delta\gamma)^2\rangle$ is evaluated by squaring $\delta\gamma$ from eq. (5.5), giving

$$\begin{aligned} \langle(\delta\gamma)^2\rangle &= \int_0^T dt_1 \int_0^T dt_2 C_{\Omega_1}(t_1 - t_2) \left[a(\sin\theta)^2 + b \frac{2}{\sqrt{\Delta^2 + \Omega^2}} \cos\theta(\sin\theta)^2 \right. \\ &\quad \left. \cdot \text{sgn}(n)\omega_B + c \frac{1}{\Delta^2 + \Omega^2} (\cos\theta \sin\theta)^2 \omega_B^2 \right] \end{aligned} \quad (5.7)$$

where $C_{\Omega_1}(t_1 - t_2) = \langle \delta\Omega_1(t_1)\delta\Omega_1(t_2) \rangle$ is the correlation function of the noise. The coefficients a, b, c are all equal to one in a Ramsey experiment, but in a spin-echo experiment they reflect the time-correlations of the noise. Defining the integrated time-correlator of the noise as

$$D(T) = \int_0^T dt_1 \int_0^T dt_2 C_{\Omega_1}(t_1 - t_2), \quad (5.8)$$

and combining eqs. (5.6) and (5.7), we recover the expression of eq. (5.2) for the coherence of the qubit to first order in the noise $\delta\Omega$,

$$v = \exp\{-D(T)(a + b \operatorname{sgn}(n)\omega_B + c\omega_B^2)/2\} \quad (5.9)$$

describing the length $v = \sqrt{\langle X \rangle^2 + \langle Y \rangle^2 + \langle Z \rangle^2}$ of the state vector of the qubit. The functions

$$\begin{aligned} a &= a(\sin\theta)^2, \\ b &= b \frac{2}{\sqrt{\Delta^2 + \Omega^2}} \cos\theta(\sin\theta)^2, \\ c &= c \frac{1}{\Delta^2 + \Omega^2} (\cos\theta \sin\theta)^2 \end{aligned} \quad (5.10)$$

appear in the three first terms in eq. (5.7), which represent dynamic dephasing, geometric dephasing, and non-geometric non-adiabatic corrections, respectively. The dimensionless universal decoherence factors a, b, c in eqs. (5.10) serve to accommodate different types of experimental protocols. We point out that geometric dephasing is present ($b \neq 0$) in the limits of fast noise (short correlation time compared to evolution time) and slow noise (long correlation time compared to evolution time; see sec. 5.2.2). Most notably, geometric dephasing is not due to imperfect adiabaticity of the qubit evolution: it does *not* vanish in the extreme adiabatic limit $T \rightarrow \infty$.

For a specific type of noise, $D(T)$ can be explicitly evaluated. Considering for instance an Ornstein-Uhlenbeck process with intensity σ^2 and correlation time $1/\Gamma$, the correlation function is $C_{\Omega_1}(t_1 - t_2) = \sigma^2 e^{-\Gamma|t_1 - t_2|}$. It follows that

$$D(T) = 2 \left(\frac{2\pi\Gamma}{\omega_B} - 1 + e^{-\frac{2\pi\Gamma}{\omega_B}} \right) / \Gamma^2.$$

Thus, we find that Ornstein-Uhlenbeck noise suppresses the qubit coherence by a factor

$$v = \exp \left\{ -\sigma^2 (a + b \operatorname{sgn}(n)\omega_B + c\omega_B^2) \frac{\frac{2\pi\Gamma}{\omega_B} - 1 + e^{-\frac{2\pi\Gamma}{\omega_B}}}{\Gamma^2} \right\}, \quad (5.11)$$

where a, b, c are defined in eqs. (5.10).

5.2.2 Short and long correlation-time limits

A priori, it cannot be ruled out that $D(T)$ introduces a time-dependence in eq. (5.9) so that there is no geometric dephasing. In the following, an arbitrary noise process is considered,

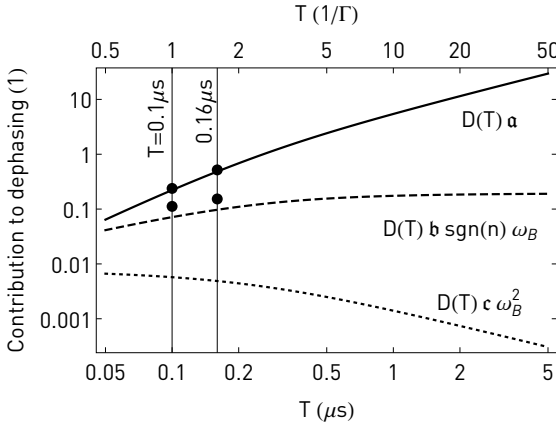


Figure 5.6: Dynamic (solid line), geometric (dashed line) and non-geometric non-adiabatic (dotted line) contributions to dephasing, as they appear in the exponent of ν in eq. (5.11), as a function of precession period T in the case of an Ornstein-Uhlenbeck process. The curves are computed with the parameters of protocol R with noise in the first window only and correspond to the data shown in Fig. 5.4(1,o) for $A = \pi/2$. The values for dynamic and geometric dephasing extracted from the fits in Fig. 5.4 are indicated by dots. The vertical lines indicate the periods $T = 0.1, 0.16 \mu\text{s}$ used there.

characterized by its intensity σ^2 (the integral of its power spectral density) and its correlation time τ . We show that only the second term $\propto (\omega_B)^1$ represents geometric dephasing by estimating the coherence suppression factor ν in two limiting cases: noise with short correlation time, $\Gamma T \gg 1$ and noise with long correlation time, $\Gamma T \ll 1$.

For a short correlation time, $\Gamma T \gg 1$ and therefore $D(T) \propto \sigma^2 T/\Gamma$. We thus obtain

$$\nu = \exp \left\{ -\text{const} \cdot \frac{2\pi\sigma^2}{\Gamma} \left(\frac{a}{\omega_B} |n| + b n + c \omega_B |n| + \dots \right) \right\} \quad (5.12)$$

and see that only the second term depends on the sign of n and represents geometric dephasing.

For a long correlation time, $\Gamma T \ll 1$, and we obtain $D(T) \propto \sigma^2 T^2$, leading to

$$\nu = \exp \left\{ -\text{const} \cdot (2\pi\sigma)^2 \left(\frac{a}{\omega_B^2} |n|^2 + \frac{b}{\omega_B} |n|n + c |n|^2 + \dots \right) \right\}. \quad (5.13)$$

Again, only the second term contributes to geometric dephasing. To sum up, there is a geometric contribution to dephasing regardless of the correlation time of the noise (or, put differently, regardless of the duration of the evolution).

The three contributions to dephasing appearing in the coherence suppression factor from eq. (5.11) are plotted in Fig. 5.6 as a function of precession period T for an Ornstein-Uhlenbeck process. The factors a, b, c are specified in eqs. (5.10) and $T = \frac{2\pi|n|}{\omega_B}$ is the duration of one half of the echo. Fig. 5.6 shows that the dynamic contribution ($\propto a$) grows with T , while the geometric contribution ($\propto b$) saturates in the limit of short correlation times $\Gamma T \gg 1$. The non-geometric non-adiabatic contribution ($\propto c$) vanishes in this limit.

In the experiment the noise amplitude and evolution time are carefully chosen so that geometric dephasing remains visible in the observed coherences: For long evolutions or strong noise, dynamical dephasing becomes too important and geometric dephasing cannot be resolved.

Table 5.1: Computed values for the coefficients a, b, c determining the dynamic, geometric and non-adiabatic non-geometric contributions to dephasing. For the measurements where the qubit acquires only dynamical phase, $\omega_B = 0$ and therefore b and c do not contribute to dephasing.

correlation of noise	protocol R			protocol P		
	a	b	c	a	b	c
correlated, $\delta\Omega_1 = \delta\Omega_2$	0	0	4	0	0	0
anticorrelated, $\delta\Omega_1 = -\delta\Omega_2$	4	0	0	4	4	4
uncorrelated, $\langle\delta\Omega_1\delta\Omega_2\rangle = 0$	2	0	2	2	2	2
1 st window, $\delta\Omega_2 = 0$	1	1	1	1	1	1

5.2.3 Protocol R: ‘geometric’ echo

Similarly to the above section, where the expectation value of the phase and the coherence were computed for a Ramsey-type experiment, these quantities can be computed for the two protocols used in this experiment. The total phase accumulated by the qubit in protocol R is

$$\gamma_R = \int_0^T dt \sqrt{(\Delta - \text{sgn}(n)\omega_B)^2 + (\Omega_0 + \delta\Omega(t))^2} - \int_T^{2T} dt \sqrt{(\Delta + \text{sgn}(n)\omega_B)^2 + (\Omega_0 + \delta\Omega(t))^2}. \quad (5.14)$$

Expanding eq. (5.14) to first order in ω_B , $\delta\Omega_1$ and $\delta\Omega_2$ gives

$$\gamma_R \approx \int_0^T dt \left[-2\text{sgn}(n)\omega_B \cos\theta - (\delta\Omega_1 - \delta\Omega_2) \sin\theta + (\delta\Omega_1 + \delta\Omega_2) \frac{\text{sgn}(n)\omega_B}{\sqrt{\Delta^2 + \Omega^2}} \cos\theta \sin\theta \right]. \quad (5.15)$$

The variance $\langle(\delta\gamma_R)^2\rangle$ is evaluated by squaring $\delta\gamma_R$ from eq. (5.15), giving

$$\begin{aligned} \langle(\delta\gamma_R)^2\rangle &= \int_0^T dt_1 \int_0^T dt_2 \left[\langle(\delta\Omega_1(t_1) - \delta\Omega_2(t_1))(\delta\Omega_1(t_2) - \delta\Omega_2(t_2))\rangle (\sin\theta)^2 \right. \\ &\quad + \langle(\delta\Omega_1(t_1) - \delta\Omega_2(t_1))(\delta\Omega_1(t_2) + \delta\Omega_2(t_2))\rangle \frac{2}{\sqrt{\Delta^2 + \Omega^2}} \cos\theta (\sin\theta)^2 \text{sgn}(n)\omega_B \\ &\quad \left. + \langle(\delta\Omega_1(t_1) + \delta\Omega_2(t_1))(\delta\Omega_1(t_2) + \delta\Omega_2(t_2))\rangle \frac{1}{\Delta^2 + \Omega^2} (\cos\theta \sin\theta)^2 \omega_B^2 \right]. \quad (5.16) \end{aligned}$$

Which of the three ensemble averages $\langle\dots\rangle$ in eq. (5.16) vanish and which ones do not depends on the correlations between $\delta\Omega_1$ and $\delta\Omega_2$. For instance, if the noise in the two halves of the echo is perfectly correlated, $\delta\Omega_1(t) = \delta\Omega_2(t)$ and the first and the second ensemble average vanish. The third one is $4\langle\delta\Omega_1(t_1)\delta\Omega_1(t_2)\rangle = 4C_{\Omega_1}(t_1 - t_2)$. Comparing eq. (5.16) with eqs. (5.7) and (5.10), we can read off the universal decoherence factors a, b, c . They are tabulated in the left half of Tab. 5.1.

Note that if one defines an effective z -component of the magnetic field $\tilde{\Delta} = \Delta - \omega_B$ in eq. (5.3), it is possible to re-interpret all geometric manipulations as dynamic phenomena (ac-stark shifts) in the frame of reference of eq. (5.3). Both this description and the one in the frame of eq. (5.1) are equally valid. Choosing one or the other rests with the reader.

5.2.4 Protocol P: ‘complete’ echo

In protocol P, the magnetic field follows the same path in both windows of the echo. Therefore this protocol is a complete echo. The phase acquired by the qubit is found from eq. (5.14) by flipping the sign of ω_B under the second square root,

$$\gamma_P = \int_0^T dt \sqrt{(\Delta - \text{sgn}(n)\omega_B)^2 + (\Omega_0 + \delta\Omega(t))^2} - \int_T^{2T} dt \sqrt{(\Delta - \text{sgn}(n)\omega_B)^2 + (\Omega_0 + \delta\Omega(t))^2}.$$

Again, expanding the above equation to first order in ω_B , $\delta\Omega_1$ and $\delta\Omega_2$ gives

$$\gamma_P \approx \int_0^T dt (\delta\Omega_1 - \delta\Omega_2) \sin\theta \left(1 + \frac{\text{sgn}(n)\omega_B}{\sqrt{\Delta^2 + \Omega^2}} \cos\theta \right). \quad (5.17)$$

There is no term to zeroth order in the noise, implying that all average phases $\langle \gamma_P \rangle$ are cancelled out by the echo pulse. However, because $\langle (\delta\gamma_P)^2 \rangle \neq 0$ dephasing is still there. Carrying out the same steps as for protocol R leads to eq. (5.11) with coefficients a, b, c given in the right half of Tab. 5.1.

5.2.5 Discussion of parameter estimates for a, b, c

For correlated noise, neither dynamic nor geometric dephasing is present ($a = b = 0$) and non-adiabatic contributions only play a role in protocol R ($c \neq 0$). In the complete spin echo (protocol P), all fluctuations cancel out ($a = b = c = 0$). The effect of correlated noise has been observed by Filipp et al. (2009) (the term in c in eq. (5.7)) and in ch. 4 (terms in a and c). For the other types of noise correlations (anticorrelated noise, uncorrelated noise and noise in the first window), there is dynamic dephasing ($a \neq 0$) in protocols R and P, and there is geometric dephasing ($b \neq 0$) in protocol P. In protocol R, geometric dephasing is only present when there is noise in the first window.

Fig. 5.7 shows parameter estimates for a and b (quantify dynamic and geometric dephasing, respectively) extracted from the data shown in Fig. 5.4 and Fig. 5.5. The observed dynamic dephasing agrees well with eq. (5.2), and the observed geometric dephasing (quantified by b) is somewhat larger than predicted. For those measurements of protocol R and P where only dynamic phase is measured, b is not extracted from a fit but rather set to zero. The fitting procedure is described in detail in sec. 5.2.7. Note that as predicted, dynamic and geometric dephasing is present in protocol P as well, that is, even when the qubit does not acquire any deterministic phase.

The time-dependence in eq. (5.2) describes the experimental data in Fig. 5.4 well. Fits to the measurements of coherences for protocol R with noise in the first window for $T = 160$ ns (Fig. 5.4(o)) give $a = 1.13 \pm 0.02$ and $b = 1.46 \pm 0.05$. These are similar to what is obtained for $T = 100$ ns (Fig. 5.4(l)), namely $a = 1.14 \pm 0.02$ and $b = 1.46 \pm 0.05$. In addition, the data support the fact that dephasing is largest for anticorrelated noise, smaller for uncorrelated noise, even smaller for noise in the first window only, and smallest for correlated noise (Fig. 5.7).

In the measurements presented, the influence of the parameter c is very small. It is therefore only fitted for the protocols with correlated noise, where $a = b = 0$. For protocol R, $c = 2$ is expected and $c = 2.25 \pm 0.25$ is found, while for protocol P, $c = 0$ is expected and $c = 0.24 \pm 0.54$ is found. In all other measurements, c is neglected. We refer to De Chiara and Palma (2003), Filipp et al. (2009) and ch. 4 for detailed studies.

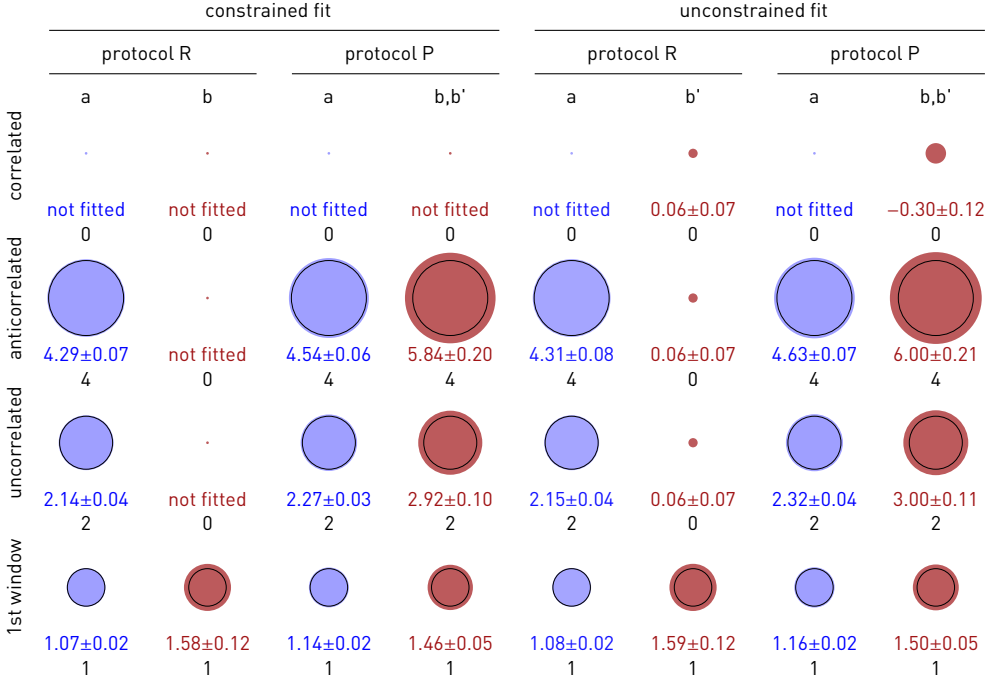


Figure 5.7: Left half: parameters estimates for a and b extracted from both fits to data in Fig. 5.4 under the constraint $a, b, c > 0$. The area is proportional to the number; theory (black circles & numbers) and fit parameter (coloured disks & numbers). Right half: same, without constraints. For the unconstrained fit to the data of protocol R with D.P., $b'' = -0.08 \pm 0.08$ is found.

5.2.6 Considerations about adiabaticity

The adiabaticity parameter is defined according to Solinas et al. (2010). The Hamiltonian being $H(t)$, we can define an instantaneous (adiabatic) basis such that $H(t)|\psi_n(t)\rangle = E_n(t)|\psi_n(t)\rangle$. Writing $D(t)$ for the transformation from a fixed basis (given e.g. by $H(0)$) to the instantaneous basis, the Hamiltonian in the instantaneous basis is $D^{-1}(t)H(t)D(t) + \hbar w$, with $w = -iD^{-1}(t)\dot{D}(t)$. In the adiabatic case, w vanishes. The adiabatic parameter is defined as $s(t) = \hbar \|w(t)\| / \sqrt{\Omega_0^2 + \Delta^2}$, where $\|w(t)\| = \text{tr} \sqrt{w^\dagger(t)w(t)}$ is the trace norm of $w(t)$. Evolution is adiabatic if $s \ll 1$.

The off-resonant pulses are shaped such that s is constant over time and independent of the solid angle when the drive Ω is increased or decreased (that is, beginning and end of the pulses). For larger solid angles, the pulses need to be longer to keep s constant across solid angles. When the magnetic field precesses (central part of the pulses), s varies from solid angle to solid angle because ω_B is kept constant. The data in Fig. 5.8 show that $s(t)$ is always smaller than 0.28 and thus adiabaticity is maintained during the whole off-resonant pulse-sequence, even when noise is applied. As expected, s is smaller for $\omega_B/2\pi|n| = T = 160$ ns than for $T = 100$ ns.

Going to the extreme adiabatic limit $s \rightarrow 0$ is not desirable. Although geometric dephasing is still present in this limit, it cannot be resolved experimentally because dynamic

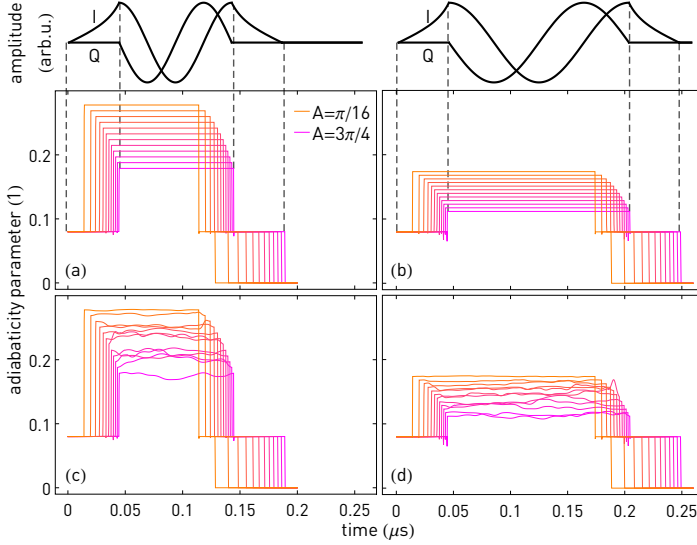


Figure 5.8: Adiabaticity parameter during the offresonant part of the pulse sequence for $\omega_B/2\pi = T = 100\text{ns}$ (a) and 160ns (b), without applied noise. Graphs for a pulse sequence with applied noise are shown in panels (c) and (d). In each panel, the adiabaticity parameter is shown for solid angles $A = \pi/16$ (orange) to $3\pi/4$ (pink) in steps of $\pi/16$. The pulse envelopes for $A = 3\pi/4$ are shown on top of the plots. Note that the curves are not offset in time; the pulses have different lengths.

Table 5.2: Fitting functions used to obtain the fit estimates for a and b presented in Fig. 5.7. The upper half of the table is for the constrained fit, the lower half for the unconstrained fit. Reading example: When the fit is unconstrained, the coherences for protocol R with correlated noise and C^{+-} are fitted using the function v from eq. (5.2) with coefficients $a \rightarrow 0$, $b \rightarrow -b'$ and $c \rightarrow 4c$.

	protocol R			protocol P		
	C^{+-}	D.P.	C^{-+}	C^{++}	D.P.	C^{--}
correlated	$(0, 0, 4c)$	$(0, 0, 0)$	$(0, 0, 4c)$	$(0, 0, c')$	$(0, 0, c')$	$(0, 0, c')$
anticorrelated	$(4a, 0, 0)$	$(4a, 0, 0)$	$(4a, 0, 0)$	$(4a, -4b, 0)$	$(4a, 0, 0)$	$(4a, 4b, 0)$
uncorrelated	$(2a, 0, 0)$	$(2a, 0, 0)$	$(2a, 0, 0)$	$(2a, -2b, 0)$	$(2a, 0, 0)$	$(2a, 2b, 0)$
1 st window	$(a, -b, 0)$	$(a, 0, 0)$	$(a, b, 0)$	$(a, -b, 0)$	$(a, 0, 0)$	$(a, b, 0)$
correlated	$(0, -b', 4c)$	$(0, b'', 0)$	$(0, b', 4c)$	$(0, b', c')$	$(0, b', c')$	$(0, b', c')$
anticorrelated	$(4a, -b', 0)$	$(4a, b'', 0)$	$(4a, b', 0)$	$(4a, -4b, 0)$	$(4a, b', 0)$	$(4a, 4b, 0)$
uncorrelated	$(2a, -b', 0)$	$(2a, b'', 0)$	$(2a, b', 0)$	$(2a, -2b, 0)$	$(2a, b', 0)$	$(2a, 2b, 0)$
1 st window	$(a, -b, 0)$	$(a, b', 0)$	$(a, b, 0)$	$(a, -b, 0)$	$(a, b', 0)$	$(a, b, 0)$

dephasing increases linearly with time (see sec. 5.2.2).

5.2.7 Fitting the measured coherences

This section describes the fit models used to extract the parameters a , b and c quantifying dynamic and geometrical dephasing.

In the fitting procedure, first the effective normalized noise amplitude is found by fitting the function eq. (5.2) describing the coherence v to the data from protocol R with noise in the first window and dynamic phase (D.P.) only, assuming $a = 1$, $b = 0$, $c = 0$ and with the normalized noise amplitude as only fit parameter. In this way, a normalized noise amplitude of $\sigma/\Omega_0^2 = 0.085$ was determined, which is slightly smaller than the set value 0.1.

Second, all data from protocol R are fitted simultaneously for coefficients a and b of the functions a and b . Where the theory predicts $b = 0$, we do not constrain the fitting

function by setting $b = 0$; rather, the same fitting function with a separate variable is used. For example, according to Fig. 5.7 no geometric dephasing ($b = 0$) is expected for protocol R with anticorrelated noise and C^{-+} . Therefore, a fitting function with $b \rightarrow b'$ is used and the fit ideally produces $b' = 0$. Moreover, a similar variable b'' is introduced for protocol R, D.P. to avoid conflating b' with it, as this would prevent b' from taking values other than zero in the fits to protocol R, C^{+-} and C^{-+} . Finally, the proportionality factors of a and b in the fitting functions are fixed across the measurements. For instance, protocol R with anticorrelated noise uses $4a$ and protocol R with uncorrelated noise uses $2a$. The data from protocol P is fitted similarly.

Third, the parameter c is only fitted for protocol R, correlated noise, C^{\pm} , where a and b vanish. This is the only measurement where it is relevant,

Fourth, the fitting parameters b' and b'' are set to zero in the fit we call ‘constrained’. When dropping this constraint, the fitted values for a and b increase slightly (by maximally 6%, see Fig. 5.7); in turn, b' and b'' become negative. Simply put, the ‘unconstrained’ model (where b' and b'' are free parameters) trades off some fitting parameters against each other in order to obtain the best fit. If theory was in perfect agreement with experimental data (no noise, no systematic errors), this trade-off would not be possible. However, due experimental imperfections the fit produces an unphysical result, namely ‘negative’ dynamic dephasing ($b', b'' < 0$). To avoid this effect, we have opted for presenting the constrained model in the main text. Comparing the parameter estimates in Fig. 5.7, it becomes apparent that both models yield similar parameter estimates. In addition, as discussed in the following paragraphs, both models (constrained and unconstrained) have empirical support.

The normal probability plots (Chambers et al., 1983) of the residues of the models, Fig. 5.9, show that the residues fall near the line describing the identity function, with the exception of a few residues which are larger than expected. Therefore, they are normally distributed. This holds for protocols R and P in both models (constrained and unconstrained). The underlying normal probability distributions of the residuals assume a mean 0 and use the standard deviation computed from the residuals:

$$\sigma_{\text{unc.}}^{(R)} = 0.0425, \quad \sigma_{\text{con.}}^{(R)} = 0.0427, \quad \sigma_{\text{unc.}}^{(P)} = 0.0319, \quad \sigma_{\text{con.}}^{(P)} = 0.0326. \quad (5.18)$$

To estimate if constrained and unconstrained models fit similarly well, we consider the Akaike information coefficient (AIC) (Burnham and Anderson, 2002). The number of fitting parameters is

$$K_{\text{unc.}}^{(R)} = 6, \quad K_{\text{con.}}^{(R)} = 4, \quad K_{\text{unc.}}^{(P)} = 5, \quad K_{\text{con.}}^{(P)} = 4, \quad (5.19)$$

where we taken into account the fact that the variance of the residuals eq. (5.18) is estimated from the model. Since the number of fitting parameters K is not very small compared to the sample size $N = 3 \cdot 4 \cdot 12 = 144$ (the number of measured coherences), we use AIC_c , the finite-sample-corrected AIC. Because the residuals are normally distributed, and assuming the variance of the residuals is constant, AIC_c takes on the simple form

$$\text{AIC}_c = N \ln(\text{RSS}/N) + 2K + \frac{2K(K+1)}{N-K-1}, \quad (5.20)$$

with the residual sum of squares RSS. When comparing two models, the better model has the smaller AIC_c value. As a rough rule of thumb (Burnham and Anderson, 2002), if the

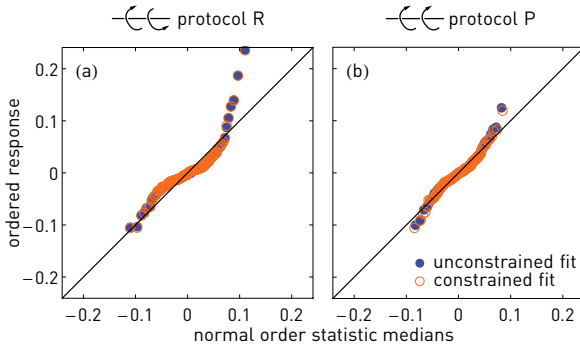


Figure 5.9: Normal probability plots of the residues of the fits from protocol R and P. The line indicates what is expected for a perfect normal distribution.

difference in AIC_c with the second model lies between 0 and 2, that model has substantial empirical support, if between 4 and 7, it has less support, and if larger than 10 it should not be considered. Here, for protocol R the unconstrained model is the better model and the difference in AIC_c with the constrained model is 2.41. For protocol P, the converse is true: The constrained model is a better model and the difference in AIC_c with the unconstrained model is 4.31. To sum up, for both protocols the constrained model and the unconstrained one have some empirical support.

In addition, a t -test has been performed to assess the significance of the parameters a, b, b', c, c' in the unconstrained model. With a sample size of $N = 144$ and $k_{\text{unc}}^{(R)} = 5$, respectively $k_{\text{unc}}^{(P)} = 4$ degrees of freedom, we find (for both) a threshold $t = 1.97$ at which a parameter value has a non-zero value with 95% of significance in a two-sided t -test. Given that

$$t_a^{(R)} = 55.53, \quad t_b^{(R)} = 12.79, \quad t_{b'}^{(R)} = 0.88, \quad t_c^{(R)} = 9.18, \quad (5.21)$$

and

$$t_a^{(P)} = 65.22, \quad t_b^{(P)} = 28.14, \quad t_{b'}^{(P)} = -2.56, \quad t_{c'}^{(P)} = 2.56, \quad (5.22)$$

it can be asserted that in both protocols the parameters a quantifying the dynamic dephasing and b quantifying the geometric dephasing are significant. Furthermore, the t -values for the parameter b' are close to zero (as it should be, since we expect $b' = 0$), indicating that in this measurement there is no geometric dephasing. Finally, the value $t_c^{(R)}$ indicates significance of the parameter c in protocol R, where non-geometric non-adiabatic dephasing is present. In protocol P, where $c' = 0$ is expected, it is only weakly significant.

We note that fitting for the parameters a, b and c for individual data sets with $n = 12$ (such as protocol R with correlated noise and C^{-+}) or groups of data sets with $n = 36$ (such as protocol R with correlated noise and either C^{-+}, C^{+-} or D.P.) does not produce useful parameter estimates. The same phenomenon as described above, the trading off of some geometric dephasing against dynamic dephasing, is exacerbated and the fit values are not significant.

5.3 Conclusion

In conclusion, we have reported on the first observation of geometric dephasing. The experiment is carried out on a qubit efficiently isolated from the environment, whose cou-

pling to an artificial noise source is under full control. In order to eliminate the dynamic phase, two different echo protocols are employed. Measurements of a variety of noise correlations show good agreement with theoretical predictions.

Typically, geometric dephasing will accompany the Berry phase. We have shown that the dependence on the *sign* of the trajectory's winding number implies that geometric dephasing may either reinforce dynamic dephasing or partially suppress it.

Given the broad spectrum of systems whose time evolution involves geometric phases, the presence of geometric dephasing is expected to be commonplace. A particularly intriguing aspect is the effect of geometric dephasing on the effective braiding phase of topological excitations, when the separation of the braiding particles is similar to the noise amplitude.

CONCLUDING REMARKS

In this thesis, three experiments on the adiabatic geometric phase have been presented. In the following, instead of summing these up once again, I will suggest a few ideas and list some proposals for experiments which could be implemented in a circuit QED setup. Some of them are within easy reach, others require more effort.

Considering the current limits set by the coherence times of superconducting qubits, quantum computation based on adiabatic geometric phases (holonomic quantum computation) is too slow to be attractive. The efforts by Abdumalikov et al. (2013), Feng et al. (2013), and Zu et al. (2014), where non-Abelian non-adiabatic geometric gates have been realized based on a proposal by Sjöqvist et al. (2012), are the first step towards implementing universal geometric quantum computation. Using non-adiabatic gates speeds up algorithms, but one question: ‘how do non-adiabatic gates fare experimentally in the presence of noise?’ remains open and decidedly deserves further attention. The developments by Johansson et al. (2012) suggest that non-adiabatic gates become noise resilient when the pulses are short enough, but this is yet to be tested *in vivo*. From this point of view—fast evolution leading to better coherence—the non-adiabatic gates are uncannily similar to the dynamical phase, pressing an investigation on their relationship and possibly their equivalence in an appropriately chosen frame of reference. In passing, we note that in addition to the aforementioned article by Sjöqvist et al. (2012), where non-Abelian non-adiabatic geometric phases are investigated in a generic three-level Λ configuration, there are schemes for quantum dots and single-molecule magnet devices (Mousolou et al., 2014), and for a cyclic chain of four qubits with tunable interactions (Mousolou and Sjöqvist, 2014).

Another approach to deal with noise in non-adiabatic holonomic quantum computation is to employ decoherence-free subspaces (Lidar et al., 1998) or its generalization, noiseless subsystems (Knill et al., 2000). Xu et al. (2012) propose a set of universal gates for decoherence-free subspaces, and Zhang et al. (2014) extend this to noiseless subsystems so that collective decoherence can be tackled. There, at least four physical qubits are needed to implement a logical qubit in a noiseless subsystem. Logical two-qubit gates can be implemented with eight physical qubits.

Putting considerations about algorithm speed and limitations due to coherence times aside, holonomic quantum computation based on non-Abelian adiabatic geometric gates is also worth investigating. The universal single qubit gates implemented by Toyoda et al. (2013) are proven to be noise-resilient. They are based on a tripod system, which consists of a state coupled to three others (Unanyan et al., 1999; Duan et al., 2001). Similar proposals for two-qubit gates exist for trapped ions (Duan et al., 2001), superconducting circuits

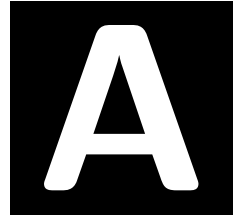
(Faoro et al., 2003) and semiconductor quantum dots (Solinas et al., 2003), but they have not been realized yet. Kamleitner et al. (2011) have developed a scheme tailored to circuit QED, where the tripod Hamiltonian allowing to implement universal single qubit gates is recovered in a system consisting of a resonator mode coupled to three flux-driven qubits.

Geometric phases themselves are a lively research field in fundamental physics. Many of types of phase have never been observed in superconducting circuits or even never been observed at all. The extension of geometric phases to mixed states can be defined in terms of purifications (Uhlmann, 1986) or operationally (Sjöqvist et al., 2000), and these definitions are equivalent under certain conditions (Rezakhani and Zanardi, 2006). Although the Uhlmann phase has been observed in NMR (Zhu et al., 2011), and the Sjöqvist phase in NMR (Du et al., 2003) as well as in optics (Ericsson et al., 2005), neither has been measured in superconducting qubits. However, its generalization to nonunitary evolution (Tong et al., 2004) has been observed by Cucchietti et al. (2010) in NMR by simulating a qubit coupled to a bath (another qubit). The authors find that the Berry phase is significantly affected if the environment is quantum critical (Quan et al., 2006).

Finally, geometric phases can also be used for metrological applications: Rong et al. (2011) use the Aharonov-Anandan phase in a phase-estimation protocol. Martín-Martínez et al. (2013) have thought up an interferometric experiment where an atom flies in one branch through a known hot source and in the other branch through an unknown cold source. From the Berry phase it acquires, the unknown temperature can be extracted. At the frontier between quantum mechanics and gravitation, there are some more proposals. For instance, Pikovski et al. (2012) suggest an optomechanical experiment to set a bound on a correction to the Heisenberg uncertainty relation due to quantum gravity, whereby a displaced resonator acquires a geometric phase. Martín-Martínez et al. (2011) propose to detect the Unruh effect (Unruh, 1976) by comparing the Berry phase acquired by an inertial detector to the phase of an accelerated one.

PART III

APPENDICES



ASPECTS OF MICROWAVE MIXERS

Microwave mixers are an important component of a circuit QED setup. They are used for upconverting IF signals to microwave frequency and for downconverting the readout signal before it is digitized and analysed. In this appendix, after a brief theoretical description of the operating principle of IQ mixers and of their imperfections, we show measurements of the higher harmonics created during upconversion and measurements of the linearity of IQ mixers. We also give a detailed description of the mixer calibration procedure.

For further details, the interested reader may refer to ch. 13 of Pozar (2012) and the references therein, or to ch. 12 of Collin (2000). Belov et al. (2012) give an overview of the commercially available products in chapters 8 and 9.

A.1 Operating principle of a mixer

A.1.1 Three-port mixer

A ideal frequency mixer is a three-port non-linear device which combines two input signals so that the output signal is the product of the two input signals. The ports are named local oscillator (LO), radio frequency (RF) and intermediate frequency (IF) port. A schematic is shown in Fig. A.1(a). The LO port serves exclusively as an input port and acts as a on/off switch: the mixer is on when the LO signal is on, and off otherwise. The other two ports are for information-bearing signals and can serve both as input and output port, depending on the intended use. For upconversion, also called modulation, the RF port outputs two microwave-frequency signals at frequencies symmetric around ν_{LO} , that is, $\nu_{\text{RF}} = \nu_{\text{LO}} \pm \nu_{\text{IF}}$. This can be seen as follows. The mixer multiplies the LO signal $s_{\text{LO}} = \cos(\omega_{\text{LO}} t)$, which acts as a carrier wave, with the signal on the IF port, $s_{\text{IF}} = I \cos(\omega_{\text{IF}} t)$. The output signal on the RF port is

$$s_{\text{RF}} = s_{\text{LO}} s_{\text{IF}} = I(\cos\omega_+ t + \cos\omega_- t)/2.$$

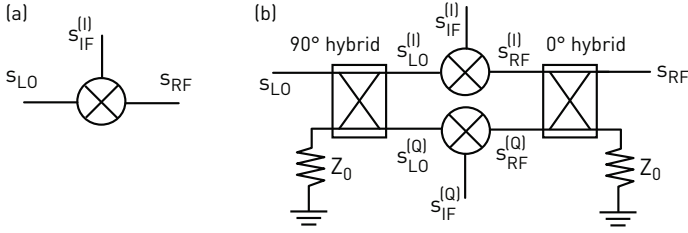


Figure A.1: (a) Schematic of a three-port mixer. (b) Schematic of an IQ mixer. See text for details.

The component with the higher frequency $\omega_+ = \omega_{LO} + \omega_{IF}$ is called the right sideband (RSB), while the component with the lower frequency $\omega_- = \omega_{LO} - \omega_{IF}$ is called the left sideband (LSB). The left and right sidebands are sometimes referred to as lower and upper sidebands. Double sideband modulation retains both sidebands, while single sideband modulation (SSB) eliminates one of the sidebands. A realistic frequency mixer is based on a non-linear element, such as a transistor or a diode (Pozar, 2012). In addition to the desired sidebands, it also generates spurs, that is, unwanted signals created during the mixing process with frequencies $\omega_{LO} \pm j\omega_{IF}$ ($j = 2, 3, \dots$), $2\omega_{LO}$, etc.

The mixer can be operated by applying either AC pulses on the IF port ($\omega_{IF} > 0$, ‘sideband modulation’) or by applying DC pulses ($\omega_{IF} = 0$, ‘direct modulation’). In the latter operating mode, the frequency of the RF signal will be equal to the LO frequency and there will be no sidebands.

When using the mixer for downconversion, or demodulation, the roles of the RF and IF ports are interchanged. The downconverted signal, which is on the IF port, has a frequency $\omega_{IF} = |\omega_{LO} - \omega_{RF}|$, since

$$s_{IF} = s_{LO} s_{RF} = I \left[\cos((\omega_{RF} + \omega_{LO})t) + \text{sgn}(\omega_{RF} - \omega_{LO}) \cos((\omega_{RF} - \omega_{LO})t) \right] / 2.$$

and the component with the higher frequency $\omega_{RF} - \omega_{LO}$ are usually filtered out.

A.1.2 IQ mixer

When using a mixer for upconversion with sideband modulation, e.g. to create pulses for qubit manipulation, it is desirable to retain solely one sideband, say with frequency $\nu_{RF} = \nu_{LO} + \nu_{IF}$, and to do away with the image response (the unwanted sideband) at frequency $\nu_{RF} = \nu_{LO} - \nu_{IF}$. The frequency difference between the two responses being $2\nu_{IF}$, the image response can easily be filtered out when ν_{IF} is large. If the IF frequency is small and filtering is difficult, an IQ mixer can be used. It produces only one of the two sidebands and also allows for controlling the phase of the upconverted signal without adjusting the phase of the LO signal. An IQ mixer consists of two three-port mixers, a 0° hybrid and a 90° hybrid. A 3 dB 90° hybrid (also called quadrature hybrid) is a directional coupler with a 90° phase difference in the two output ports and a coupling factor of 3 dB, meaning that the power at the input port will be equally distributed to the two output ports. The 0° hybrid acts like the 90° hybrid, but without phase shift—it is an in-phase power combiner.

The circuit of an IQ mixer is shown in Fig. A.1(b). The LO signal is split by the 90° hybrid and routed to the LO ports of the three-port mixers. The two upconverted signals

are combined in the 0° hybrid. In mathematical terms, the inputs at the LO ports are

$$s_{\text{LO}}^{(I)} = K \cos(\omega_{\text{LO}} t) \quad \text{and} \quad s_{\text{LO}}^{(Q)} = K \cos(\omega_{\text{LO}} t - \pi/2). \quad (\text{A.1})$$

At the three-port mixers, $s_{\text{LO}}^{(I)}$ is mixed with the IF signal $s_{\text{IF}}^{(I)} = I \cos(\omega_{\text{IF}} t + \varphi_I)$ and $s_{\text{LO}}^{(Q)}$ is mixed with $s_{\text{IF}}^{(Q)} = Q \cos(\omega_{\text{IF}} t + \varphi_Q)$. This yields

$$\begin{aligned} s_{\text{RF}}^{(I)} &= s_{\text{LO}}^{(I)} s_{\text{IF}}^{(I)} = KI [\cos(\omega_+ t + \varphi_I) + \cos(\omega_- t + \varphi_I)] / 2, \\ s_{\text{RF}}^{(Q)} &= s_{\text{LO}}^{(Q)} s_{\text{IF}}^{(Q)} = KQ [\cos(\omega_+ t + \varphi_Q - \pi/2) + \cos(\omega_- t + \varphi_Q + \pi/2)] / 2. \end{aligned}$$

The in-phase power combiner adds these signals to form the output signal of the IQ mixer,

$$\begin{aligned} s_{\text{RF}} &= s_{\text{RF}}^{(I)} + s_{\text{RF}}^{(Q)} = KI [\cos(\omega_+ t + \varphi_I) + \cos(\omega_- t + \varphi_I)] / 2 \\ &\quad + KQ [\cos(\omega_+ t + \varphi_Q - \pi/2) + \cos(\omega_- t + \varphi_Q + \pi/2)] / 2. \end{aligned} \quad (\text{A.2})$$

Looking at eq. (A.2), we observe that it is possible to eliminate the image response by choosing

$$I = Q \quad \text{and} \quad \varphi_I - \varphi_Q = -\pi/2 \quad (\text{A.3a})$$

in case the RSB of frequency $\omega_+ = \omega_{\text{LO}} + \omega_{\text{IF}}$ is desired, and by choosing

$$I = Q \quad \text{and} \quad \varphi_I - \varphi_Q = \pi/2 \quad (\text{A.3b})$$

in case the LSB of frequency $\omega_- = \omega_{\text{LO}} - \omega_{\text{IF}}$ is desired. In brief, it is possible to perform SSB modulation with an IQ mixer by applying to the I and Q ports two pulses of identical amplitude with a relative phase shift of $\pi/2$.

With eqs. (A.2) and eq. (A.3a), the upconverted signal (when utilizing the RSB) is found to be

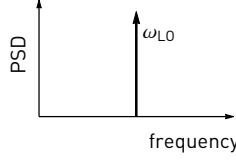
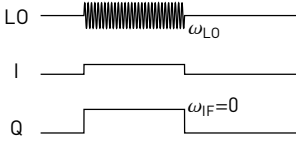
$$\begin{aligned} s_{\text{RF,RSB}} &= KQ [\cos(\omega_+ t + \varphi_Q - \pi/2)] / 2 + KQ [\cos(\omega_+ t + \varphi_Q - \pi/2)] / 2 \\ &= KQ \cos(\omega_+ t + \varphi_Q - \pi/2). \end{aligned}$$

It has amplitude KQ and phase φ_Q . In other words, both amplitude and phase of the signal s_{RF} can be set by adjusting the amplitudes I, Q and the phases φ_I, φ_Q of the signals $s_{\text{IF}}^{(I)}$ and $s_{\text{IF}}^{(Q)}$. The same holds for the LSB: combining eqs. (A.2) and eq. (A.3b) gives

$$\begin{aligned} s_{\text{RF,LSB}} &= KQ [\cos(\omega_- t + \varphi_Q + \pi/2)] / 2 + KQ [\cos(\omega_- t + \varphi_Q + \pi/2)] / 2 \\ &= KQ \cos(\omega_- t + \varphi_Q + \pi/2). \end{aligned}$$

Note that when DC-modulating the mixer, $\omega_{\text{IF}} = 0$, $\varphi_I = \varphi_Q - \pi/2$ and therefore $s_{\text{RF}} = KQ \cos(\omega_{\text{LO}} t + \varphi_Q)$.

(a) direct modulation



(b) sideband modulation

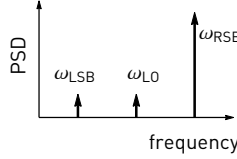
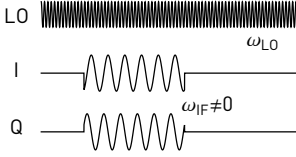


Figure A.2: (a) Scheme of the pulses as they arrive at the mixer on the LO, I and Q ports for direct modulation (left); scheme of the power spectral density (PSD) of the output spectrum of the mixer (right). The frequency of the up-converted signal is $\omega_{RF} = \omega_{LO}$. (b) The same, but for single sideband modulation when using the right sideband. The frequency of the upconverted signal is $\omega_{RSB} = \omega_{LO} + \omega_{IF}$. The mirror image is at $\omega_{LSB} = \omega_{LO} - \omega_{IF}$

A.2 Mixer calibration for sideband modulation

The relations (A.3) assume an ideal mixer consisting of ideal components. Real devices however show some imperfections. For instance, when doing downconversion, due to imperfections in the hybrid couplers the I and Q quadratures are not perfectly orthogonal and their amplitudes do not match, giving rise to what is called quadrature imbalance. These imperfections not only distort the signal, but also affect the cancellation of the mirror image. In addition, there is LO leakage, meaning that some of the signal s_{LO} is transmitted to the RF port even when no voltage is applied to the I and Q ports.

Schematics of pulses implementing single sideband modulation and direct modulation are shown in Fig. A.2. In this example, the phases are set to $\varphi_Q = \pi/8$ and $\varphi_I = -3\pi/8$ so that $\varphi_I - \varphi_Q = -\pi/2$. Therefore, when $\omega_{IF} \neq 0$ the RSB is used and the LSB is cancelled. The upconverted signal has a phase of $\pi/8$ with respect to the LO. For direct modulation, the signal applied to the LO port is pulsed to avoid LO leakage, that is, leakage of the signal from the the LO port through the mixer to the RF port. Because the pulses applied to the I and Q ports have a finite duration, their frequency spectrum (see Fig. A.2) is not a delta-peak at a certain frequency. It follows a sinc function if the pulses have a square envelope. For sideband modulation, the frequency spectrum contains not only the desired upconverted signal at ω_{RSB} but also LO leakage at ω_{LO} and a spur at the frequency of the mirror image ω_{LSB} .

A.2.1 Removing the mirror image

To model the imperfections of the mixer, we consider I and Q inputs which are offset in amplitude (by additive terms ΔI and ΔQ) and phase shifted (by $\Delta\varphi_I$ and $\Delta\varphi_Q$) compared to the ideal I and Q inputs in eq. (A.1),

$$\begin{aligned} s_{LO}^{(I)} &= K(1 + \Delta I) \cos(\omega_{LO} t + \Delta\varphi_I) \\ s_{LO}^{(Q)} &= K(1 + \Delta Q) \cos(\omega_{LO} t + \Delta\varphi_Q - \pi/2). \end{aligned}$$

The output of the mixer s_{RF} then becomes (and should be compared with eq. (A.2)),

$$s_{\text{RF}} = KI(1 + \Delta I) \left[\cos(\omega_+ t + \varphi_I + \Delta\varphi_I) + \cos(\omega_- t + \varphi_I - \Delta\varphi_I) \right] / 2 \\ + KQ(1 + \Delta Q) \left[\cos(\omega_+ t + \varphi_Q + \Delta\varphi_Q - \pi/2) + \cos(\omega_- t + \varphi_Q - \Delta\varphi_Q + \pi/2) \right] / 2.$$

Cancelling the LSB is achieved by choosing

$$I = Q \frac{1 + \Delta Q}{1 + \Delta I} \quad \text{and} \quad \varphi_I - \varphi_Q = -\pi/2 + \Delta\varphi_I - \Delta\varphi_Q \quad (\text{A.4a})$$

while the RSB is eliminated by letting e.g.

$$I = Q \frac{1 + \Delta Q}{1 + \Delta I} \quad \text{and} \quad \varphi_I - \varphi_Q = +\pi/2 + \Delta\varphi_Q - \Delta\varphi_I \quad (\text{A.4b})$$

Note that eqs. (A.4) indeed reduce to eqs. (A.3) in the limit of an ideal mixer, viz. $\Delta I, \Delta Q, \Delta\varphi_I, \Delta\varphi_Q \rightarrow 0$. When using the RSB, the resulting signal is, via eq. (A.2.1) and eq. (A.4a),

$$s_{\text{RF,RSB}} = Q(1 + \Delta Q) \cos(\Delta\varphi_I - \Delta\varphi_Q) \cos(\omega_+ t + \varphi_Q - \pi/2 + \Delta\varphi_I).$$

For the LSB, eq. (A.2.1) together with eq. (A.4b) give

$$s_{\text{RF,LSB}} = Q(1 + \Delta Q) \cos(\Delta\varphi_I - \Delta\varphi_Q) \cos(\omega_- t + \varphi_Q + \pi/2 + \Delta\varphi_I).$$

In the experiment, we most often use mixers IQ-4509MXP or IQ-0714MXP from Marki Microwave. Their bandwidth is $\omega_{\text{RF,LO}}/2\pi \in [4.5, 9]$ GHz and $\omega_{\text{RF,LO}}/2\pi \in [7, 14]$ GHz, respectively, with an IF bandwidth of 500 MHz. The signals for the I and Q ports are usually generated with an arbitrary waveform generator (AWG) Tektronix 5014, allowing to generate signals with a bandwidth of 500 MHz.

The optimal parameters eq. (A.4) to cancel the mirror image are determined by minimizing the signal measured at its frequency. This is achieved by sweeping the relative amplitude and phase of the I and Q channels (ideally being 1 and $\pm\pi/2$) when generating the patterns for the AWG. Typically, when not calibrated, the mixers have an image rejection of 20 to 25 dB. Calibrating the mixer increases the image rejection to about 40 dB. Note that the optimal parameters gained in the calibration procedure depend strongly on ω_{LO} and ω_{IF} .

A.2.2 Suppressing LO leakage

Typically, the mixers IQ-4509MXP or IQ-0714MXP provide an isolation from LO to RF of about 25 dB. When doing sideband modulation and operating with IF frequencies of 100 MHz to 200 MHz, the leakage is somewhat detuned from the RF output of the mixer (coinciding with e.g. a qubit transition), but still drives the transition off-resonantly. This is undesirable, but crude experiments, such as measurements of the coherence time of the qubit, still work out. However, this constant off-resonant driving makes experiments impossible when doing direct modulation—see below in sec. A.4.

LO leakage can be suppressed by adding a small DC bias voltage to signals of the I and Q ports of the mixer. Normally, a bias of a few millivolt is sufficient. The bias is applied

either by using a bias tee to combine the IF signal from the AWG with a DC signal, or by feeding a DC signal to the ‘add input’ port on the back panel of the Tektronix 5014 AWG (see sec. 2.3), which adds it to the IF output of the AWG. When doing sideband modulation, both implementations perform equally well. When doing direct modulation, one must use the ‘add input’ port because the RF port of the bias tee filters out the step-like signal from the AWG.

A.3 Higher harmonics of sideband mixing

As mentioned above, the output spectrum of an IQ mixer used to upconvert a DC IF signal displays not only the desired upconverted signal, but also spurious higher harmonics created during the upconversion process. In this paragraph, the output spectrum of a mixer IQ-0714MXP is analysed in typical conditions for circuit QED experiments. The upconversion setup is as shown in Fig. 2.3. The Tektronix AWG 5014 generates two continuous sine waves I and Q with a frequency $\nu_{\text{IF}} = 100$ MHz, which are input to the I and Q ports of the IQ mixer in order to use the right sideband. The frequency of the local oscillator (operated in c.w. mode) is set to $\omega_{\text{LO}} = 7$ GHz. The mixer is driven at ≈ 15 dBm (for a recommended driving level 13 dBm to 16 dBm). Measurements at other LO frequencies (which provide similar results) can be found in Abadal (2014). The mixer IQ-0714MXP supports IF frequencies as large as 500 MHz. However, the larger the IF frequency, the larger the conversion loss. This is why usually IF frequencies between 100 MHz and 300 MHz are used.

The calibration for DC offsets and mirror image removal is carried out for using the RSB at $\nu_{\text{RSB}} = 7.1$ GHz with a peak-to-peak voltage $V_{\text{pp}} = 400$ mV_{pp} on the AWG analogue outputs (equivalent to a peak voltage $V_{\text{p}} = 200$ mV_p). The mixer is only calibrated for this voltage, where it is expected to still behave linearly; it is not recalibrated when other, smaller voltages are applied to the I and Q ports. Before looking at the output frequency spectrum of the mixer, the voltages at the AWG need to be converted into voltage at the IF ports of the mixer. The AWG outputs sinusoidal waveforms with a certain peak voltage V_{p} . The corresponding rms voltage is

$$V_{\text{rms}} = V_{\text{p}} / \sqrt{2}.$$

The RG-58 BNC cable connecting the AWG outputs to the mixer has a length of 2 m and a loss of about 0.33 dB at 100 MHz. Losses at connectors can be ignored. Then, we have installed 10 dB of attenuation at the IF port. Therefore, a single IF port sees a rms voltage¹

$$V = V_{\text{rms}} - 10.33 \text{ dB} = V_{\text{p}} / \sqrt{2} - 10.33 \text{ dB}. \quad (\text{A.5})$$

Assuming that the quadratures are more or less balanced, the voltage applied to the IF ports I and Q is about the same. The total power delivered to the mixer is then doubled, and therefore the total voltage is $\sqrt{2}$ times the voltage in eq. (A.5)²:

$$V = \sqrt{2} \left(V_{\text{p}} / \sqrt{2} - 10.33 \text{ dB} \right). \quad (\text{A.6})$$

¹To do the conversion between voltage and power, a resistance of 50 Ω is assumed. To compute the voltage V , V_{rms} must first be expressed in the unit of dB assuming a resistance of 50 Ω , before the losses and the attenuation can be subtracted.

²In the following equation, one must first compute the bracket and then multiply by $\sqrt{2}$.

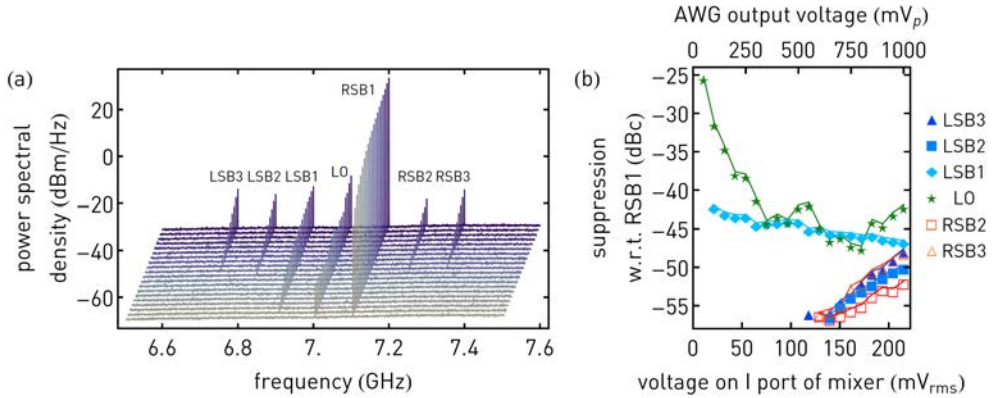


Figure A.3: (a) Power spectral density of the upconverted sinusoidal signal as a function of frequency for total voltages input to the mixer ranging from $15\text{ mV}_{\text{rms}}$ (brown curve in front) to $304\text{ mV}_{\text{rms}}$ (purple curve at the back) in steps of 15 mV_{pp} . The curves are offset horizontally and vertically for better legibility. (b) Relative power of the sideband peaks compared to the power of the RSBs as a function of the voltage applied to the I port of the mixer.

The voltage used for calibration $V_p = 200\text{ mV}_p$ corresponds to a total input voltage of $61\text{ mV}_{\text{rms}}$.

The output spectrum of the mixer is recorded by connecting a spectrum analyser (Agilent E4407) to the RFport of the mixer. At the input port of the spectrum analyser, there is a DC-block. The spectrum analyser is used to record the power spectrum of the mixer output in the frequency range $\nu_{\text{LO}} \pm 500\text{ MHz} = [6.5, 7.5]\text{ GHz}$. A power spectrum is recorded for AWG output voltages from $100\text{ mV}_{\text{pp}}$ to $2000\text{ mV}_{\text{pp}}$ in steps of 100 mV , corresponding to total mixer input voltages from $15\text{ mV}_{\text{rms}}$ to $304\text{ mV}_{\text{rms}}$. The maximal mixer input voltage exceeds the voltage at which it is calibrated—this is because we calibrate the mixer at a low input voltage so that it is linear, but here exceptionally wish to apply higher voltages to test its linearity. The data in Fig. A.3(a) clearly shows higher harmonics, placed at integer multiples of ν_{IF} around ν_{LO} . At the maximal AWG output voltage, third-order harmonics can be seen. Their amplitude increases with the AWG output voltage.

The suppression of the different higher harmonics with respect to the RSBs are plotted as a function of the voltage on the I port of the mixer in Fig. A.3(b). The suppression of the higher harmonics is at least 40 dBm . The suppression of the LO is lowest when the carrier signal is weak, that is, for low voltages on the I port (-15 dBc or equivalently -57 dBm). At higher voltages, it improves to about 40 dBc .

A.4 Mixer calibration for direct modulation

Fig. A.3 shows that the spectrum of a signal created by upconversion with an IQ mixer displays various spurs. As described above in sec. A.2, there are two types of spurs when performing sideband modulation: the higher harmonics created during the upconversion process, as well as leakage of the LO signal. To avoid off-resonant driving of the qubit or any other system under investigation, two things are done: the mirror image is minimized

by optimizing the relative amplitude and phase of the signals applied to the I and Q ports, and the LO leakage is minimized by adding a DC bias to these.

For direct modulation, there is no sideband mixing and therefore no higher harmonics. However, there still is quadrature imbalance, that is, the amplitude of the upconverted RF signal depends on its phase φ . For the experiment this is bothersome because, say, the amplitude of a π_x -pulse ($\varphi = 0$) and the amplitude of a π_y -pulse ($\varphi = \pi/2$) are different. In addition, the LO leakage is on resonance with the transition of the system under investigation, always slightly driving the transition even when the mixer is closed and thus making measurements of the geometric phase impossible. The solution is to gate the LO, that is, using pulse modulation³ of the signal generator so that the LO signal is on only when the mixer opens and switched off as soon as the mixer is closed. Typically, gating times of 20 ns to 40 ns are chosen. This procedure has the drawback that the mixer DC bias cannot be calibrated with the standard routine (applying a small DC offset on the I and Q ports of the mixer while leaving the LO on, and measuring the RF signal using the FPGA) because the FPGA acquires only a few tens of nanoseconds of signal, and the signal-to-noise ratio is too low.

A.4.1 Mixer calibration procedure

It is possible to calibrate both the LO leakage and the quadrature imbalance of the mixer operated in the DC regime by using the qubit as a calibration tool. The idea is to determine the amplitude of the signal needed to induce a π -flip in the qubit for different quadrature phase angles φ . To do so, Rabi oscillations between the ground and first excited state of the qubit, as presented in sec. 2.5.3, are recorded by applying pulses with increasing amplitude for various φ . In the following we present the protocol and experimental data.

1. Set the mixer calibration to default: no DC bias voltage, and relative phase and amplitude of I and Q not optimized.
2. Choose the length of the LO gating pulse (typically 20 ns) and use an oscilloscope to time the arrival of the LO gating pulse at the mixer with the arrival of the I and Q pulses from the AWG. The length of these pulses should be equal to the length of the LO gating pulse. When using a Tektronix 5014 AWG with a signal generator Agilent E8257, the gating pulse should typically arrive at the signal generator ≈ 80 ns before the AWG starts outputting the pulses for I and Q.
3. Record Rabi oscillations by applying pulses on the I quadrature (quadrature phase angle $\varphi = 0$) with increasing amplitude. The pulse duration is to be kept constant. Repeat this measurement for $n \geq 5$ different values of φ . It is preferable, albeit not strictly necessary, to distribute the values equally in the IQ plane, that is, choose $\varphi_j = 2\pi j/n, 0 \leq j \leq n-1$.

For an ideal mixer, when drawing the excited state population p_e of the qubit as a function of the pulse amplitude along I and Q, the maxima of p_e (the π -pulse amplitudes r_π) describe a circle centred at the origin of the IQ plane. LO leakage shifts the center of the circle, while quadrature imbalance squeezes the circle into an ellipse.

³All signal generators Agilent E8257 come with narrow pulses modulation (minimal modulation time 20 ns) for frequencies above 3.2 GHz. Between 10 MHz and 3.2 GHz the option 1E6 is required.

4. An ellipse in a plane is completely defined by five parameters. (This is why at least five measurements r_π are needed.) In polar coordinates, these parameters are the centre of the ellipse (a_0, φ_0) , the semidiameters a and b , and the angle φ' between the axis a and the line defined by $\varphi \equiv 0$. The ellipse is thus parameterized as $r(\varphi) = (P(\varphi) + Q(\varphi))/R(\varphi)$, where $0 \leq \varphi \leq 2\pi$ and

$$\begin{aligned} P(\varphi) &= a_0 [(b^2 - a^2) \cos(\varphi + \varphi_0 - 2\varphi') + (a^2 + b^2) \cos(\varphi - \varphi_0)] \\ Q(\varphi) &= \sqrt{2}ab\sqrt{R(\varphi) - 2a_0^2 \sin^2(\varphi - \varphi_0)} \\ R(\varphi) &= (b^2 - a^2) \cos(2\varphi - 2\varphi') + a^2 + b^2. \end{aligned} \tag{A.7}$$

The ellipse describing the quadrature imbalance of the mixer is found by fitting the parametrization in eqs. (A.7) to the measured points $r_\pi(\varphi_j)$.

5. Use the parameter estimates for a_0 and φ_0 to determine what DC bias voltages on I and Q are required in order to recentre the ellipse. Apply the DC bias voltages needed to centre the ellipse on the origin of the IQ plane. Roughly speaking, +100 mV applied in front of a 1 : 10 voltage divider shift the origin by +3 mV with 10 dB of attenuation at the I and Q ports.
6. Repeat the Rabi measurements. With eqs. (A.7), determine the ellipse defined by the π -pulse amplitudes $r_\pi(\varphi_j)$. The ellipse should now be centred on the origin. If not, repeat the previous step until the ellipse is centred with desired accuracy. This completes the calibration of the DC bias voltage.
7. From the centred ellipse, extract its tilt φ' and its semimajor and semiminor axes a and b . In order to balance the quadratures (read: map the ellipse to a circle) the relative amplitude of the signals applied to the I and Q ports must be adjusted. We thus rescale these signals by a factor $s = s(\varphi)$. As a reference point where $s = 1$, we choose the amplitude $r(\varphi = 0)$ of the π -pulse applied on the I quadrature. Then, the scaling factor is $s(\varphi) = r(\varphi)/r(0)$, the fitted π -amplitude $r(\varphi)$ divided by $r(0)$.
8. After integrating the scaling function $s(\varphi)$ into the pattern generation routine, repeat the Rabi measurements once again and extract the ellipse defined by the π -pulse amplitudes. The calibration is successful if the amplitudes $r_\pi(\varphi_j)$ of the π -pulses define a circle centred at origin of the IQ plane.

We illustrate such a calibration procedure with three sets of Rabi oscillations ($j = 8$, see Fig. A.4) recorded with a mixer IQ-4509 MXP at a frequency of 4.944 GHz. The extracted parameters are listed in Tab. A.4.1. There, the eccentricity $\epsilon = \sqrt{1 - (a/b)^2}$ of the ellipse and the 'amplitude imbalance' $AI = 20 \log_{10} a/b$ are also indicated.

The first set is recorded with default mixer calibration (step 2, Fig. A.4(a)). The quadrature imbalance as well as the LO leakage are immediately apparent: The points $r_\pi(\varphi)$ define an off-centre ellipse. The amplitude imbalance is $AI = 1.89$ dB, which is much larger than the typical 0.3 dB given in the data sheet of the mixer. From the ellipse, the DC bias voltage required to minimize the LO leakage is determined to be about 3 mV. The measured qubit populations p_e , which were computed by solving the Cavity-Bloch equations,

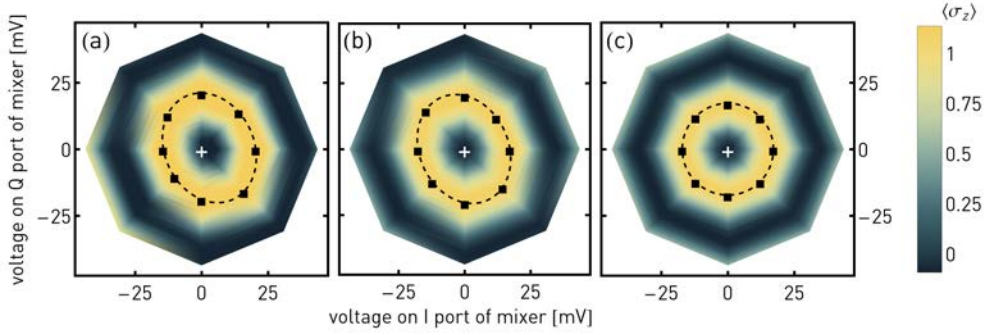


Figure A.4: Resonant mixer calibration. First excited state population $\langle p_e \rangle$ as a function of the voltage applied to mixer I and Q ports. $\langle p_e \rangle$ is extracted from amplitude Rabi measurements along fixed phase angles φ . The voltages $r_\pi(\varphi_j)$ corresponding to a π -pulse are marked by black squares, the ellipse fitted to the $r_\pi(\varphi_j)$ is also shown (dashed line). The point where zero voltage is applied on both the I and Q ports of the mixer is indicated by a white cross. (a) Populations measured with zero DC bias voltage and relative amplitude/phase of signals on I and Q not optimized. (b) Populations measured with DC bias voltage and optimized amplitude and phase of signals on I and Q.

Table A.1: Parameter estimates for the ellipses shown in Fig. A.4 during the various stages of mixer calibration, as well as the parameters for an ideal mixer.

calibration	a_0 [mV]	φ_0 [rad]	a [mV]	b [mV]	ϵ	φ' [rad]	AI [dB]
none	2.98	0.10	21.3	16.8	0.61	2.00	1.89
only DC bias	0.29	-0.32	21.3	16.8	0.61	2.00	1.89
fully calibrated	0.01	-0.53	17.1	17.2	0.11	0.17	-0.18
ideal mixer	0	—	—	—	0	—	—

are not always between 0 and 1. This is because the calibration pulses used to compute the populations are off since at this point the mixer is not calibrated.

The second set of Rabi measurements, with optimal DC bias (steps 5 and 6, Fig. A.4(b)), shows an almost centred ellipse with an amplitude imbalance $AI = 1.89$ dB. The DC bias is almost optimal ($a_0 = 0.29$ mV instead of 2.98 mV before calibration). The third set of Rabi oscillations, taken with a fully calibrated mixer, shows fully balanced I and Q quadratures with minimized LO leakage (step 8, Fig. A.4(c)). The amplitude imbalance is now only $AI = -0.18$ dB. The calibrated mixer compares favourably with an ideal mixer with $a_0 = 0$ and vanishing amplitude imbalance $\epsilon = 0$. It should be pointed out that the quality of the calibration achieved in this example is representative of this calibration procedure—the level of accuracy reached here can routinely be achieved (e.g. at different qubit frequencies or with a different mixer). Furthermore, assuming that the transition frequency of the qubit is stable, the qubit itself does not affect the calibration of the mixer.

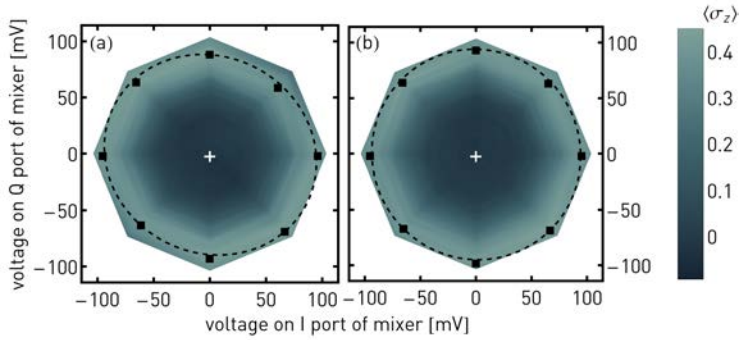


Figure A.5: Off-resonant mixer calibration. First excited state population $\langle p_e \rangle$ as a function of the voltage applied to mixer I and Q ports. Scale for $\langle p_e \rangle$ and symbols are as in Fig. A.4. (a) Populations measured with calibrated DC bias voltage. (b) Populations measured with full calibration.

A.4.2 Off-resonant mixer calibration

The above calibration protocol can also be used when the mixer is not operated at the transition frequency ω_{01} of the qubit, but at some slightly detuned frequency, $|\omega_{\text{LO}} - \omega_{ge}| \lesssim 80\text{MHz}$ —for instance when generating the off-resonant pulses in the geometric phase measurements presented in part II of this thesis. The main difference between the off-resonant and the resonant calibration is the fitting function. When driving a two-level system off-resonantly with constant drive Ω and detuning Δ , the excited-state population is (Foot, 2007, ch. 7)

$$p_e = \frac{\Omega^2}{\Omega^2 + \Delta^2} \sin\left(\frac{1}{2}\sqrt{\Omega^2 + \Delta^2}t\right), \quad (\text{A.8})$$

which for $\Delta = 0$ reduces to the familiar function used to fit resonant Rabi oscillations

$$p_e = \sin\left(\frac{1}{2}\Omega t\right). \quad (\text{A.9})$$

Because eq. (A.8) assumes constant amplitudes, square pulses have to be used for off-resonant mixer calibration. For a finite detuning Δ , $p_e < 1$ and points other than the $r_\pi(\varphi_j)$ have to be used to fit the ellipse describing the mixer. Using a local maximum reached by the function $p_e(\Omega)$ in eq. (A.8) is a good choice. Otherwise, the calibration protocol is unchanged: Record Rabi oscillations using pulses with different phases φ , extract an ellipse describing the LO leakage and quadrature imbalance, correct for it by adding a DC bias voltage and scaling the pulses on I and Q.

To illustrate that this protocol works, data from an off-resonant mixer calibration performed at a detuning of $\Delta/2\pi = -50\text{MHz}$ is shown in Fig. A.5. A mixer IQ-4509 is used, with $\omega_{\text{LO}} = 7.084\text{GHz}$ and $\omega_{01} = 7.034\text{GHz}$. In Fig. A.5(a), the LO leakage has already been corrected for. From the parameter estimates of the ellipse we find $a_0 = 1.15\text{mV}$ and $\epsilon = 0.42$. In panel (b), where the mixer is fully calibrated, $a_0 = 0.76\text{mV}$ and $\epsilon = 0.19$.

A.5 Linearity of mixer

Ideally, mixers obey a linear input-output relation, i.e. the power measured at the RF port is linear in the power fed on the I and Q ports. For small input powers, this is the case, but for large input powers the output signal is compressed. The mixer models IQ-4509 or IQ-0714MXP have an input 1 dB compression point lying between 4 dBm and 6 dBm. To quantify how linear the response is and what voltages can be applied before the mixer starts to compress, we use the power spectral density measurements similar to those in Fig. A.2. When doing experiments, it is preferable to work in the linear regime far below the 1 dB compression point. For instance, in part II of this thesis, the solid angle enclosed by the effective magnetic field is a function of the amplitude Ω of an upconverted signal, which is calibrated using a Rabi measurement. If the mixer response is non linear, the effectively enclosed solid angle differs from the desired solid angle.

The device under test is an IQ-0714MXP mixer, driven continuously at $\omega_{\text{LO}} = 7$ GHz with a power of 16 dBm. There are 10 dB of attenuation at each of the IF ports. The mixer is sideband-modulated with $\omega_{\text{IF}} = 100$ MHz and calibrated as described in sec. A.2 for use of the RSB at $400 \text{ mV}_{\text{pp}}$. Thirty-two power spectra are recorded, one for each AWG output voltage from $100 \text{ mV}_{\text{pp}}$ to $3200 \text{ mV}_{\text{pp}}$ in steps of 100 mV . The voltages at ω_{RSB} extracted from these are shown in Fig. A.6. Although these measurements are performed at the edge of the band of the mixer, the results are very similar to what is obtained at frequencies lying in the center of the band Abadal (2014).

To assess how linear the mixer is, thirty-two linear fits f_i are made to data sets consisting of the i lowest voltages, $i = 1, \dots, 32$. For each f_i the coefficient of determination r^2 is computed (Draper and Smith, 1998, ch. 5). The coefficients plotted in Fig. A.6(a) show that r^2 -value starts dropping at $i = 8$ ($121 \text{ mV}_{\text{rms}}$ of total voltage on the IF ports, 400 mV_p at the AWG outputs with the configuration used here). This somewhat arbitrarily sets the point where we say the mixer response becomes nonlinear. In the same figure, we also show a linear fit to the lowest eight voltages, extrapolated to cover the whole voltage range, and an empirical fit of all voltages to a quadratic function.

Fig. A.6(b) shows the same information on a doubly logarithmic scale. This allows us to determine the input 1 dB compression point $P_{1\text{dB}}$ by looking at the difference between these two fits. We extrapolate $P_{1\text{dB}} = 8.42 \text{ dBm}$ (equivalently $590 \text{ mV}_{\text{rms}}$ on the IF ports, or 1936 mV_p at the AWG output). The specifications of the mixer indicate a typical value of $P_{1\text{dB}} = 6 \text{ dBm}$ which is slightly lower than what is found here. Defining a ‘0.5 dB compression point’, we locate it at -2.29 dBm ($172 \text{ mV}_{\text{rms}}$ on the IF ports, 564 mV_p at the AWG output).

For an ideal mixer (linear, no conversion loss), the function describing the relation between output power and input power is the identity function. In a doubly logarithmic plot such as Fig. A.6(b), non-zero conversion loss simply vertically offsets the identity function. Here, a conversion loss of 5.1 dB is found. This is somewhat better than the typical performance of such a mixer (6 dB at 7 GHz) but still plausible.

In principle, a characterization of the linearity of the mixer response may be used to extend the useful range of the mixer: one can correct the voltages output by the AWG as a function of the desired RF output voltage according to the mixer response. However, the mixer response needs to be measured anew at for every mixer and for every operating

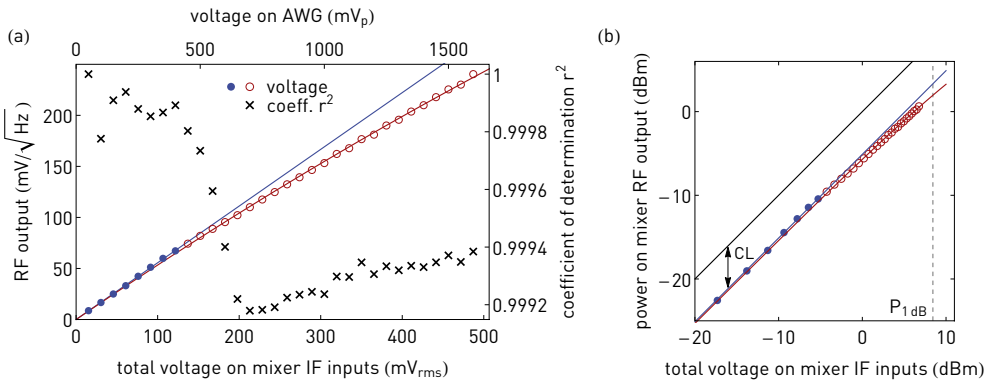


Figure A.6: Linearity of mixer response. (a) Voltage measured at the RF port of the mixer at the frequency of the RSB as a function of the rms voltage applied to the IF ports. The blue line is a linear fit to the full dots, the red line a quadratic fit to the empty dots. The crosses show the coefficient of determination r^2 of a linear fit to the lowest voltage up to the given voltage. (b) The same, but with powers on a logarithmic scale instead of voltages. The black line is a linear mixer with no conversion loss (CL). The extrapolated input 1 dB compression point $P_{1\text{dB}}$ is marked by a dashed line.

frequency of the mixer, which is rather time-consuming. It is preferable to use a mixer with a high 1 dB compression point.

NOISE GENERATION

In ch. 4 and ch. 5, synthesized noise is applied to the effective magnetic field used to guide the qubit. In this appendix, we describe the mathematics behind the generation of the noise and provide calibration data.

B.1 Ornstein-Uhlenbeck process

The noise considered is a continuous Markov process $X(t)$. For a pedagogical introduction to this type of noise, see the article by Gillespie (1996). In the following, we lean on this article to provide a minimum of definitions.

A random variable X has a *density function* P if $P(x)dx$ is equal to the probability that a sampling of X gives a value in the interval between x and $x + dx$. In other words, the density function P specifies the shape of the histogram one obtains by sampling X many times. The density function fully specifies a random variable. The *average* of a function f with respect to a random variable X (characterized by a density function P) is defined as

$$\langle f(X) \rangle = \int_{-\infty}^{\infty} f(x)P(x)dx.$$

The expression $\langle X^k \rangle$ is the k th *moment* of X . The first moment $\langle X \rangle$ is called the *mean* of X . The *variance* of X is defined as $\langle (X - \langle X \rangle)^2 \rangle = \langle X^2 \rangle - \langle X \rangle^2$. The square root of the variance is called the *standard deviation* of X . The *normal* (or *Gaussian*) random variable N has a density function given by

$$P(n) = \frac{1}{\sqrt{2\pi\sigma^2}} \exp\left(-\frac{(n - m)^2}{2\sigma^2}\right).$$

This random variable has mean m , standard deviation σ and variance σ^2 . A normal random variable with $m = 0$ and $\sigma = 1$ is called *unit random variable*.

A *stochastic process* is a random variable whose density function P depends on time t . A stochastic process is a *memoryless* (or *Markov*) process if at any time t , $X(t + dt)$ depends only on the time t , the infinitesimal time increment dt and the value of X at time t . Assuming that the increment $X(t + dt) - X(t)$ depends smoothly on t , dt and $X(t)$, and that the increment vanishes in the limit $dt \rightarrow 0$, it can be shown (Gillespie, 1996) that any Markov process takes on the analytical form

$$X(t + dt) = X(t) + A(X(t), t)dt + \sqrt{D(X(t), t)}N(t)\sqrt{dt}. \quad (\text{B.1})$$

The above equation, called the *Langevin equation* for the process X , is an update formula: it can be used to compute $X(t + dt)$ given $X(t)$. In eq. (B.1), $N(t)$ is a unit random variable which is temporally uncorrelated. The function $A(x, t)$ is called the *drift function* of the process. $D(x, t)$, which has to be nonnegative, is called the *diffusion function*.

A continuous Markov process with drift and diffusion functions of the form

$$A(x, t) = -\frac{1}{\tau}x \quad \text{and} \quad D(x, t) = c \quad \text{with} \quad \tau, c > 0$$

is called *Ornstein-Uhlenbeck* process with *relaxation time* τ and *diffusion constant* c . Its solution is a normal random variable with mean and variance

$$m = x_0 e^{-(t-t_0)/\tau} \quad \text{and} \quad \sigma^2 = \frac{c\tau}{2}(1 - e^{-2(t-t_0)/\tau}). \quad (\text{B.2})$$

In the limit $t \rightarrow \infty$, the mean relaxes to $m \rightarrow 0$ and the variance $\sigma^2 \rightarrow \frac{c\tau}{2}$. The Ornstein-Uhlenbeck process in this limit is called *fully relaxed*. Now, in order to generate an Ornstein-Uhlenbeck process numerically, one could make use of the update formula eq. (B.1) and the closed form of the process eq. (B.2). To create the whole process at once instead of using a series of updates, a different approach is needed.

B.2 Spectral density function

Let X be a stationary process with vanishing mean¹. Its second moment $\langle X^2(t) \rangle = \sigma^2$ is called the *intensity* of X . The *auto-covariance* (or *correlation function*) of this process is defined by

$$C_X(t') = \langle X(t)X(t+t') \rangle.$$

It is independent of t because X is stationary. Its Fourier representation is

$$C_X(t') = \int_0^\infty S_X(\nu) \cos(2\pi\nu t') d\nu.$$

Letting $t' = 0$ in the above equations gives the *Wiener-Khintchine theorem*,

$$\langle X^2(t) \rangle = \int_0^\infty S_X(\nu) d\nu,$$

¹The Ornstein-Uhlenbeck process is not stationary. The fully relaxed process is.

i.e. the *spectral density function* (also called *power spectrum*) $S_X(\nu)$ tells us what portion of the intensity of X is due to the frequencies between ν and $\nu + d\nu$. The fully relaxed Ornstein-Uhlenbeck process has an exponentially decaying auto-covariance

$$C_X(t') = \frac{c\tau}{2} e^{-t'/\tau}. \quad (\text{B.3})$$

Its spectral density function

$$S_X(\nu) = \frac{2c\tau^2}{1 + (2\pi\tau\nu)^2} \quad (\text{B.4})$$

describes a Lorentzian with full width at half-maximum $1/2\pi\tau$.

B.3 Numerical generation of the noise

This section describes how an Ornstein-Uhlenbeck process with specific properties is numerically generated. Measurements of the noise with a spectrum analyser show that the noise indeed is as desired.

B.3.1 Fourier representation

We can write an Ornstein-Uhlenbeck process $X(t)$ as the sum of its Fourier components (Rice, 1944),

$$X(t) = \sum_{k=0}^K (a_k \cos(2\pi\nu_k t) + b_k \sin(2\pi\nu_k t)),$$

with a_k and b_k independent random variables normally distributed around zero with a variance $\sigma^2 = S_X(\nu)\Delta\nu$, where $\nu_k = n\Delta\nu$. To minimize computational effort, it is recommended to rewrite the above as

$$X(t) = \sum_{k=0}^K c_k \cos(2\pi\nu_k t + \phi_k), \quad (\text{B.5})$$

with $c_k = \sqrt{2S_X(\nu)\Delta\nu}$ and ϕ_k a random phase angle uniformly distributed in the interval $[0, 2\pi[$. To represent $X(t)$ faithfully, the sums should have infinitely many terms ($K = \infty$). For practical reasons, we choose to cut off the sum when all significant contributions are present, for example, following Filipp (2006), at

$$\nu_{\max} = 7/\tau. \quad (\text{B.6})$$

At this point, 98.56% of the total power of the process is included.

The discrete frequency interval $\Delta\nu$ has to be chosen so that the period of the Fourier series representation of X , eq. (B.5), is larger than the duration of the experiment (about 500 ns). Letting $K = 55$ and $\tau = 100$ ns (or equivalently $\Gamma = 10$ MHz), we have $\Delta\nu = \nu_{\max}/(K - 1) = 1.30$ MHz, and a period $1/\Delta\nu = 771$ ns. Also, the fastest oscillations have a frequency of $\nu_{\max} = 70$ MHz, which is well below the effective output frequency of the Tek 5014 AWG (480 MHz) and the IF bandwidth of the IQ mixers (500 MHz). Fig. B.1 shows a realization of a process with these parameters and diffusion constant $c = 80 \text{ V}^2/\text{Hz}$ created using eq. (B.5). The corresponding spectral density function eq. (B.4) is shown, too.

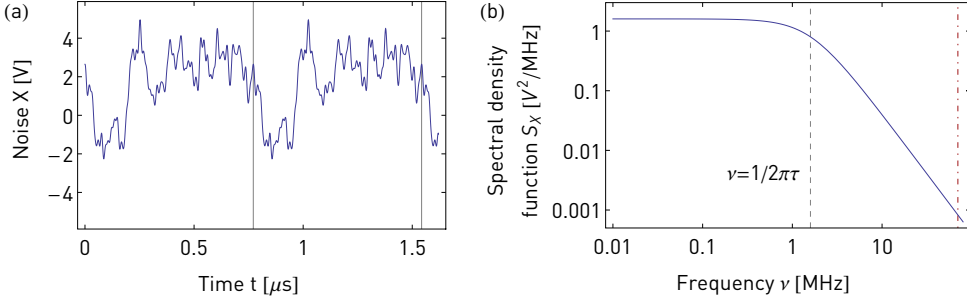


Figure B.1: (a) Example of an Ornstein-Uhlenbeck process $X(t)$ with relaxation time $\tau = 100$ ns (corresponding to a bandwidth $\Gamma = 10$ MHz) and diffusion constant $c = 80$ V²/Hz (corresponding to a standard deviation of $\sigma = 2$ V). The period of the process (indicated by vertical lines) is determined by $K = 55$ and $\nu_{\max} = 7/\tau = 70$ MHz as $1/\Delta\nu = K/\nu_{\max} \approx 771$ ns. (b) Spectral density function $S_X(\nu)$ on a doubly logarithmic scale. S_X is flat for low frequencies and has a knee at $\nu = 1/2\pi\tau = 1.59$ MHz (dashed vertical line). The trailing part has a slope of -2 , characteristic of the quadratic decay of a Lorentzian. The cutoff at $\nu_{\max} = 70$ MHz is indicated by a dash-dotted line.

A way to test the numerically generated Ornstein-Uhlenbeck process is to compute its auto-covariance function and to compare it to theory, eq. (B.3). To this effect, a process with parameters as in Fig. B.1 is generated according to eq. (B.5) and the auto-covariance is computed by numerically integrating ($\mathcal{T} = (K - 1)/\nu_{\max}$, see Rice (1944) on p. 31)²

$$C_X(t') = \frac{1}{\mathcal{T}} \int_0^{\mathcal{T}} X(t)X(t+t')dt. \quad (\text{B.7})$$

Fitting the auto-covariance function eq. (B.3) to the data thus obtained gives parameter estimates for the diffusion constant and the relaxation time which agree very well with the desired values (see Fig. B.2(a)). The correlation function however has a vertical offset which should be zero in theory. The value of this offset changes from noise realization to noise realization, and its mean tends to zero when $K \rightarrow \infty$. For $K = 55$, it is about 0.5 V². This means that there the noise exhibits some correlations at DC frequencies because of the finite number of Fourier components used to represent it.

B.3.2 Smoothing of the noise envelope

Ultimately, the noise process $X(t)$ will be added to an unperturbed signal during a certain time interval. To avoid discontinuities in the combined signal at those points t_i , t_f in time where the noise is ‘turned on’, $X(t)$ needs to be forced to zero at t_i and t_f . Therefore, $X(t)$ is multiplied with a smoothing function—in principle, any function which is zero at t_i , rises to one, stays at one until shortly before t_f , when it smoothly falls to zero.

Here, a type of Fermi-Dirac distribution $f(\beta, \mu, t) = 1/(1 + e^{-\beta(t-\mu)})$ was used. For the ascending part of the smoothing function, an interval of $\pm\beta$ around the inflexion point of

²This reference gives the definition $C_X(t') = \lim_{T \rightarrow \infty} \frac{1}{T} \int_{t=0}^T X(t)X(t+t')dt$, which, in the case of periodic functions, reduces to eq. (B.7).

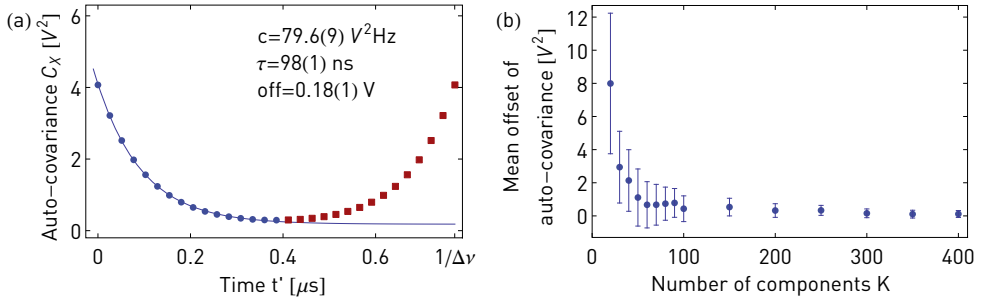


Figure B.2: (a) Auto-covariance function C_X of an Ornstein Uhlenbeck process $X(t)$ with parameters identical to Fig. B.1 ($\tau = 100$ ns, $c = 80$ V²Hz). The process has a period $K/v_{\max} \approx 771$ ns, and so does C_X . Dots and squares are computed values of C_X . The blue line is a fit of the expected function eq. (B.3) to the dots solely; the fitting function includes an additional vertical offset. The parameter estimates are printed in the plot. (b) Mean offset of the auto-covariance function as a function of the number of components K included in the Fourier decomposition of $X(t)$. For each value of K , thirty auto-covariance functions were considered.

f is excerpted, shifted and stretched out vertically to fit the image range $[0,1]$:

$$\tilde{f}(\beta, \mu, t) = \frac{f(\beta, \mu, t + \mu/2) - f(\beta, 0, -\mu/2)}{f(\beta, 0, \mu/2) - f(\beta, 0, -\mu/2)}.$$

For the descending part, this function is mirrored and shifted in time. The resulting smoothing function is

$$\hat{f} = \begin{cases} \tilde{f}(\beta, \mu, t + t_i + \mu/2) & \text{if } t_i < t \leq t_i + \mu \\ 1 & \text{if } t_i + \mu < t \leq t_f - \mu \\ \tilde{f}(\beta, \mu, -t + t_f + \mu/2) & \text{if } t_f - \mu \leq t_f \\ 0 & \text{else} \end{cases}$$

As mentioned above, the duration of ramp can be controlled by adjusting the ‘chemical potential’ μ , and its steepness by the ‘inverse temperature’ β . For the experiments presented in ch. 4 and ch. 5, $\mu = 10$ ns was chosen as a compromise between adiabatically turning on the noise and keeping the ramp duration short. Setting $\beta = 500$ MHz then results in a moderately steep ramp. A sample of six noise processes smoothed by this function in the interval $[t_i = 0, t_f = 0.5 \mu\text{s}]$ is shown in Fig. B.3(a); the smoothing function itself is shown in Fig. B.3(b). One sees that, as it should, the smoothing functions forces the noise process to 0 at $t = 0$ and at $t = 0.5 \mu\text{s}$ in 10 ns but does not affect it at other times.

When the smoothing functions reaches one, there is a discontinuity in its derivative. Although this kink does not matter, it could be avoided by using a squared sine instead of a Fermi-Dirac-like function.

B.3.3 Measurements with spectrum analyser

Whether the noise numerically generated via eq. (B.5) conforms to the design parameters can be tested with the help of the spectrum analyser. An AWG pattern of $5 \mu\text{s}$ length with noise (no DC component, $\Gamma = 10$ MHz and a variance of 10% of the dimensionless amplitude, output set to $2V_{\text{pp}}$) is created and run continuously on a channel of the AWG. This

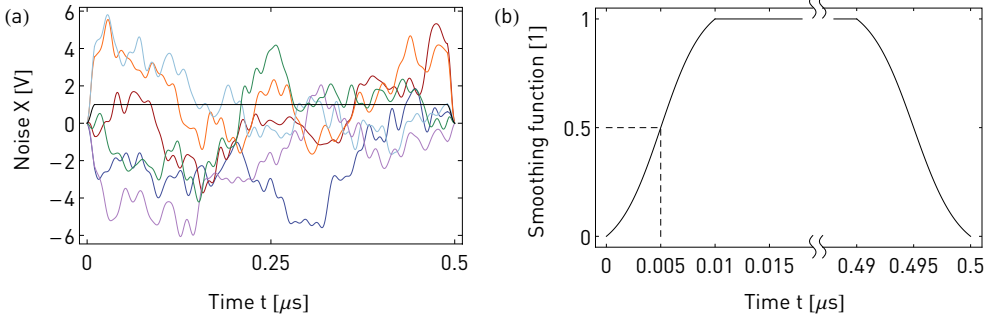


Figure B.3: (a) Six realizations of a noise process (coloured wiggly lines) smoothed by the function shown in black. The noise process has a bandwidth $\Gamma = 10$ MHz and a standard deviation of $\sigma = 2$ V. The smoothing function has $\mu = 10$ ns, $\beta = 500$ MHz and works in the interval $[t_i = 0, t_f = 0.5 \mu\text{s}]$. (b) Zoom on the ramps of the smoothing function in (a).

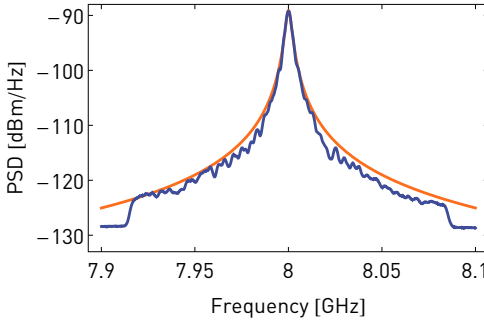


Figure B.4: Spectral density function of a c.w. signal consisting of noise upconverted to 8 GHz (blue curve), and fit (orange curve). See text for details.

signal is then upconverted to 8 GHz using an IQ mixer and measured with the spectrum analyser.³

The spectral density function of this signal is shown in Fig. B.4. The signal was recorded with a resolution bandwidth RBW of 3 MHz and a video bandwidth of 10 kHz. The video bandwidth was chosen very low in order to make the noise measurement less noisy (Agilent, 2012). A fit to the Lorentzian eq. (B.4) gives the parameters tabulated in Tab. B.1. For convenience, the expected values and the parameters describing the Lorentzian in the more standard form

$$\frac{A}{1 + \left(\frac{\nu - \nu_0}{\delta\nu_0/2}\right)^2} \quad (\text{B.8})$$

are also given. In eq. (B.8), ν_0 is the centre frequency, $\delta\nu_0$ the full width at half maximum (FWHM) and A the ‘amplitude’ of the Lorentzian (in units of a power spectral density). The signal is symmetric around the peak at 8 GHz. It vanishes at $8 \text{ GHz} \pm 70 \text{ MHz}$ (which

³Note that for noise measurements the spectrum analyser (Agilent E4407B) by default indicates dBm/RBW as a function of frequency, which can be converted to a spectral density function (dBm/Hz) by subtracting $10 \log_{10} \text{RBW}$.

Table B.1: Parameters of the noise process as set at generation, and as extracted from the fit (with corresponding uncertainties).

parameter			set	actual	error
center frequency	ν_0	[GHz]	8	8.000	$3 \cdot 10^{-6}$
relaxation time	τ	[ns]	100	99.78	0.27
diffusion constant	c	[W Hz]	—	39.04	0.17
intensity	$\sigma^2 = c\tau/2$	[μW]	—	1.948	0.010
‘amplitude’	$A = 2c\tau^2$	[fW/Hz]	—	388.7	2.7
FWHM	$\delta\nu_0 = 1/\pi\tau$	[MHz]	3.184	3.190	0.008
noise bandwidth	$\Gamma = 1/\tau$	[MHz]	10	10.02	0.03

corresponds to the cutoff-frequency from eq. (B.6), viz. $\nu_{\max} = 7/\tau = 70$ MHz), at which point the spectrum analyser records the noise floor at -131 dBm. The spectral density function is well-described by a Lorentzian, and the relaxation time extracted from the fit agrees very well with the expected value.

Determining the variance of the noise is somewhat more involved. The intensity computed from the fitted values for c and τ is $\sigma^2 = 1.948 \mu\text{W}$, resulting in a standard deviation

$$\sqrt{50 \Omega \cdot \sigma^2} = 9.87 \text{ mV}. \quad (\text{B.9})$$

of the noise at the input port of the spectrum analyser. This numerical value should be compared with variance one obtains by tracking the variance chosen at the generation of the noise through the upconversion chain.

First, the upconversion losses must be determined. All the components in the upconversion chain (from the output of the AWG to the input of the spectrum analyser) are listed in Tab. B.2. The combined losses are $\ell \approx 20.72$ dB. For the semi-rigid coaxial cables, the loss constant at 8 GHz is $\alpha = 2$ dB/m.

The upconversion losses can also be determined directly, e.g. by generating white noise in the band from 0 to 100 MHz with the AWG and (i) determining its power P_{dc} with the spectrum analyser, and (ii) first upconverting it to 8 GHz and then determining its power P_{ac} . A continuously run white noise pattern on an AWG Tek 5014 with $V_{\text{rms}} = 1$ V and run at $1V_{\text{pp}}$ gives a ratio

$$\ell' = 10 \log_{10} \frac{P_{\text{dc}}}{P_{\text{ac}}} = 10 \log_{10} \frac{1.2 \cdot 10^{-11} \text{ W}}{1.0 \cdot 10^{-13} \text{ W}} \approx 20.8 \text{ dB}.$$

Note that ℓ' reflects the losses nos.1 to 11 in Tab. B.2: the last semi-flexible coaxial cable, no.12, is not included in ℓ' because it is present in both measurements (i) and (ii). However in (ii) the signal at 8 GHz incurs losses in no.12 not present in (i) where the signal is at DC. These effects roughly compensate each other and so ℓ can be compared to ℓ' . They agree rather well—this is perhaps coincidental seeing how sensitive these power measurements are.

Table B.2: Components in the upconversion chain, and their losses.

no.	name	part number	loss [dB]
	AWG Tek 5014 output		
1	semi-flexible coaxial cable at d.c.		(small)
2	flange-mount connector		(small)
3	semi-rigid coaxial cable	MicroCoax UT-85-TP	0.2
4	SMA(m) connector	AEP 9401-1583-010	(small)
5	attenuator	Mini-Circuits BW-S10W2+	9.97
6	IQ mixer	Marki Microwave IQ-0714MXP	6.3
7	SMA(f)-SMA(f) adapter	SWMI 231-502SF	(small)
8	switch	SHX 801-02-L-3-1-15	0.3
9	semi-rigid coaxial cable	UT-85-TP	0.2
10	SMA(f) connector	AEP 9402-1583-010	(small)
11	DC block	Aeroflex Inmet 8039	≤0.5
12	semi-flexible coaxial cable at 8 GHz		2.75
	spectrum analyser		
	total upconversion loss		20.72 to 21.22

Second, the expected voltage (i.e. the standard deviation of the noise) can be computed from the variance of the noise at the output of the AWG

$$\begin{aligned}
 \sigma_{\text{output}} &= \text{variance in terms of dimensionless amplitude} \\
 &\quad \cdot \frac{1}{2} \text{ peak-to-peak voltage set on AWG} \\
 &= 10\% \cdot \frac{1}{2} \cdot 2\text{V} = 0.1\text{V} \cong -6.99\text{dB},
 \end{aligned}$$

and from there, the standard deviation at the input port of the spectrum analyser is found to be

$$\sigma = \sigma_{\text{output}} - \ell = -6.99\text{dB} - 20.72\text{dB} = -27.71\text{dB} \cong 9.20\text{mV},$$

in reasonable agreement with eq. (B.9).

BIBLIOGRAPHY

- Abadal A R. *Calibration of an IQ mixer for continuous and pulsed modulation*. Master's thesis, ETH Zurich (2014) (pp. 86 and 92)
- Abdumalikov A A, Astafiev O, Zagoskin A M, Pashkin Y A, Nakamura Y and Tsai J S. 'Electromagnetically induced transparency on a single artificial atom'. *Phys. Rev. Lett.* **104**, 193601 (2010) (p. 39)
- Abdumalikov A A, Fink J M, Juliusson K, Pechal M, Berger S, Wallraff A and Filipp S. 'Experimental realization of non-Abelian non-adiabatic geometric gates'. *Nature* **496**, 482 (2013) (pp. 12, 13, 39, and 77)
- Agilent. 'Spectrum and signal analyzer measurements and noise (application note)'. Tech. rep., Agilent Technologies (2012) (p. 100)
- Aharonov Y and Anandan J. 'Phase-change during a cyclic quantum evolution'. *Phys. Rev. Lett.* **58**, 1593 (1987) (p. 11)
- Ai Q, Huo W, Long G L and Sun C P. 'Nonadiabatic fluctuation in the measured geometric phase'. *Phys. Rev. A* **80**, 024101 (2009) (p. 46)
- Aitchison I J R and Wanelik K. 'On the real and complex geometric phases'. *Proc. R. Soc. Lond. A* **439**, 25 (1992) (p. 11)
- Ambegaokar V and Baratoff A. 'Tunneling between superconductors'. *Phys. Rev. Lett.* **10**, 486 (1963) (p. 21)
- Anandan J. 'Non-adiabatic non-abelian geometric phase'. *Phys. Lett. A* **133**, 171 (1988) (p. 11)
- . 'The geometric phase'. *Nature* **360**, 307 (1992) (pp. 8 and 11)
- Arvind, Mallesh K S and Mukunda N. 'A generalized Pancharatnam geometric phase formula for three-level quantum systems'. *J. Phys. A: Math. Gen.* **30**, 2417 (1997) (pp. 7 and 8)
- Baur M. *Realizing quantum gates and algorithms with three superconducting qubits*. Ph.D. thesis, ETH Zurich (2012) (pp. 14 and 32)

- Baur M, Filipp S, Bianchetti R, Fink J M, Göppl M, Steffen L, Leek P J, Blais A and Wallraff A. 'Measurement of autler-townes and mollow transitions in a strongly driven superconducting qubit'. *Phys. Rev. Lett.* **102**, 243602 (2009) (p. 39)
- Belov L A, Smolskiy S M and Kochemasov V N. *Handbook of RF, Microwave, and Millimeter-Wave Components*. Artech House, Boston & London (2012) (p. 81)
- Bergeal N, Schackert F, Metcalfe M, Vijay R, Manucharyan V E, Frunzio L, Prober D E, Schoelkopf R J, Girvin S M and Devoret M H. 'Phase-preserving amplification near the quantum limit with a Josephson ring modulator'. *Nature* **465**, 64 (2010) (p. 30)
- Berry M V. 'Quantal phase factors accompanying adiabatic changes'. *Proc. R. Soc. Lond. A* **392**, 45 (1984) (pp. 1, 9, and 10)
- . 'The geometric phase'. *Sci. Amer.* **259**, 46 (1988) (pp. 10 and 11)
- . 'Anticipations of the geometric phase'. *Physics Today* **43**, 34 (1990) (p. 11)
- Bhandari R and Samuel J. 'Observation of topological phase by use of a laser interferometer'. *Phys. Rev. Lett.* **60**, 1211 (1988) (p. 12)
- Bianchetti R. *Control and readout of a superconducting artificial atom*. Ph.D. thesis, ETH Zurich (2010) (pp. 22, 24, 30, 32, and 35)
- Bianchetti R, Filipp S, Baur M, Fink J M, Göppl M, Leek P J, Steffen L, Blais A and Wallraff A. 'Dynamics of dispersive single-qubit readout in circuit quantum electrodynamics'. *Phys. Rev. A* **80**, 043840 (2009) (pp. 29, 30, and 62)
- Bianchetti R, Filipp S, Baur M, Fink J M, Lang C, Steffen L, Boissonneault M, Blais A and Wallraff A. 'Control and tomography of a three level superconducting artificial atom'. *Phys. Rev. Lett.* **105**, 223601 (2010) (pp. 19, 23, and 39)
- Bitter T and Dubbers D. 'Manifestation of Berry topological phase in neutron spin rotation'. *Phys. Rev. Lett.* **59**, 251 (1987) (p. 12)
- Blais A, Gambetta J, Wallraff A, Schuster D I, Girvin S M, Devoret M H and Schoelkopf R J. 'Quantum-information processing with circuit quantum electrodynamics'. *Phys. Rev. A* **75**, 032329 (2007) (p. 31)
- Blais A, Huang R S, Wallraff A, Girvin S M and Schoelkopf R J. 'Cavity quantum electrodynamics for superconducting electrical circuits: An architecture for quantum computation'. *Phys. Rev. A* **69**, 062320 (2004) (pp. 1, 13, 19, 20, and 29)
- Blais A and Tremblay A M S. 'Effect of noise on geometric logic gates for quantum computation'. *Phys. Rev. A* **67**, 012308 (2003) (p. 49)
- Blanter Y M and Buttiker M. 'Shot noise in mesoscopic conductors'. *Physics Reports* **336**, 1 (2000) (p. 49)

- Blasone M, Henning P A and Vitiello G. 'Berry phase for oscillating neutrinos'. *Physics Letters B* **466**, 262 (1999) (p. 1)
- Bohm A. *Quantum mechanics: foundations and applications*. Theoretical and Mathematical Physics. Springer, Berlin, 3rd edn. (1993) (p. 12)
- Bohm A, Mostafazadeh A, Koizumi H, Niu Q and Zwanziger J. *The Geometric Phase in Quantum Systems: Foundations, Mathematical Concepts, and Applications in Molecular and Condensed Matter Physics*. Springer, Berlin (2003) (p. 11)
- Boissonneault M. *Effets non-linéaires et qualité de la mesure en électrodynamique quantique en circuit*. Master's thesis, Université de Sherbrooke (2007) (p. 31)
- Boissonneault M, Gambetta J M and Blais A. 'Improved superconducting qubit readout by qubit-induced nonlinearities'. *Phys. Rev. Lett.* **105**, 100504 (2010) (pp. 19 and 20)
- Brune M, Schmidt-Kaler F, Maali A, Dreyer J, Hagleitner E, Raimond J M and Haroche S. 'Quantum Rabi oscillation: A direct test of field quantization in a cavity'. *Phys. Rev. Lett.* **76**, 1800 (1996) (p. 13)
- Burnham K and Anderson D. *Model Selection and Multimodel Inference: A Practical Information-Theoretic Approach*. Springer, New York, 2nd edn. (2002) (p. 74)
- Bylander J, Gustavsson S, Yan F, Yoshihara F, Harrabi K, Fitch G, Cory D G, Nakamura Y, Tsai J S and D O W. 'Noise spectroscopy through dynamical decoupling with a superconducting flux qubit'. *Nat. Phys.* **7**, 565 (2011) (p. 49)
- Carollo A, Fuentes-Guridi I, Santos M F and Vedral V. 'Geometric phase in open systems'. *Phys. Rev. Lett.* **90**, 160402 (2003) (p. 49)
- Castellanos-Beltran M A and Lehnert K W. 'Widely tunable parametric amplifier based on a superconducting quantum interference device array resonator'. *Appl. Phys. Lett.* **91**, 083509 (2007) (pp. 23 and 30)
- Chambers J M, Cleveland W S, Kleiner B and Tukey P A. *Graphical methods for data analysis*. Wadsworth & Brooks/Cole (1983) (p. 74)
- Chen H, Hu M, Chen J and Du J. 'Observation of geometric phases for three-level systems using nmr interferometry'. *Phys. Rev. A* **80**, 054101 (2009) (p. 39)
- Chiorescu I, Bertet P, Semba K, Nakamura Y, Harmans C J P M and Mooij J E. 'Coherent dynamics of a flux qubit coupled to a harmonic oscillator'. *Nature* **431**, 159 (2004) (p. 14)
- Chow J M, Gambetta J M, Tornberg L, Koch J, Bishop L S, Houck A A, Johnson B R, Frunzio L, Girvin S M and Schoelkopf R J. 'Randomized benchmarking and process tomography for gate errors in a solid-state qubit'. *Phys. Rev. Lett.* **102**, 090502 (2009) (p. 15)
- Chruscinski D and Jamiolkowski A. *Geometric Phases in Classical and Quantum Mechanics*, vol. 36 of *Progress in Mathematical Physics*. Springer (2004) (p. 11)

- Clarke J and Wilhelm F K. 'Superconducting quantum bits'. *Nature* **453**, 1031 (2008) (p. 14)
- Collin R E. *Foundations for Microwave Engineering*. Wiley-IEEE Press, New York, 2nd edn. (2000) (pp. 17 and 81)
- Cucchietti F, Zhang J F, Lombardo F, Villar P and Laflamme R. 'Geometric phase with nonunitary evolution in the presence of a quantum critical bath'. *Phys. Rev. Lett.* **105**, 240406 (2010) (pp. 49 and 78)
- De Chiara G and Palma G M. 'Berry phase for a spin 1/2 particle in a classical fluctuating field'. *Phys. Rev. Lett.* **91**, 090404 (2003) (pp. 49, 50, 58, 59, and 71)
- Devoret M and Schoelkopf R J. 'Superconducting circuits for quantum information: An outlook'. *Science* **339**, 1169 (2013) (p. 14)
- Devoret M H. 'Quantum fluctuations in electrical circuits'. In Reynaud S, Giacobino E and Zinn-Justin J (eds.), *Quantum Fluctuations: Les Houches Session LXIII*, 351–386. Elsevier (1997) (p. 16)
- DiCarlo L, Chow J M, Gambetta J M, Bishop L S, Johnson B R, Schuster D I, Majer J, Blais A, Frunzio L, Girvin S M and Schoelkopf R J. 'Demonstration of two-qubit algorithms with a superconducting quantum processor'. *Nature* **460**, 240 (2009) (p. 39)
- Draper N R and Smith H. *Applied Regression Analysis*. John Wiley & Sons, New York (1998) (p. 92)
- Du J F, Zou P, Shi M J, Kwak L C, Pan J W, Oh C H, Ekert A, Oi D K L and Ericsson M. 'Observation of geometric phases for mixed states using NMR interferometry'. *Phys. Rev. Lett.* **91**, 100403 (2003) (p. 78)
- Duan L M, Cirac J I and Zoller P. 'Geometric manipulation of trapped ions for quantum computation'. *Science* **292**, 1695 (2001) (p. 77)
- Dutra S M. *Cavity Quantum Electrodynamics*. John Wiley & Sons, New York (2005) (p. 13)
- Dutta P and Horn P M. 'Low-frequency fluctuations in solids: 1/f noise'. *Rev. Mod. Phys.* **53**, 497 (1981) (p. 49)
- Eichler C, Salathe Y, Mlynek J, Schmidt S and Wallraff A. 'Quantum-limited amplification and entanglement in coupled nonlinear resonators'. *Phys. Rev. Lett.* **113**, 110502 (2014) (pp. 30 and 62)
- Eichler C and Wallraff A. 'Controlling the dynamic range of a josephson parametric amplifier'. *EPJ Quantum Technology* **1**, 2 (2014) (p. 30)
- Ellinas D, Barnett S and Dupertuis M. 'Berry's phase in optical resonance'. *Phys. Rev. A* **39**, 3228 (1989) (p. 49)
- Ericsson M, Achilles D, Barreiro J T, Branning D, Peters N A and Kwiat P G. 'Measurement of geometric phase for mixed states using single photon interferometry'. *Phys. Rev. Lett.* **94**, 050401 (2005) (p. 78)

- Faoro L, Siewert J and Fazio R. 'Non-Abelian holonomies, charge pumping, and quantum computation with Josephson junctions'. *Phys. Rev. Lett.* **90**, 028301 (2003) (p. 78)
- Fedorov A, Steffen L, Baur M, da Silva M P and Wallraff A. 'Implementation of a Toffoli gate with superconducting circuits'. *Nature* **481**, 170 (2012) (p. 39)
- Feng G, Xu G and Long G. 'Experimental realization of nonadiabatic holonomic quantum computation'. *Phys. Rev. Lett.* **110**, 190501 (2013) (p. 77)
- Feynman R, Sands M and Leighton R. *The Feynman Lectures on Physics Vol.3*. Addison-Wesley (1971) (p. 14)
- Filipp S. *New Aspects of the Quantum Geometric Phase*. Ph.D. thesis, Technischen Universität Wien (2006) (pp. 53 and 97)
- Filipp S, Klepp J, Hasegawa Y, Plonka-Spehr C, Schmidt U, Geltenbort P and Rauch H. 'Experimental demonstration of the stability of Berry's phase for a spin-1/2 particle'. *Phys. Rev. Lett.* **102**, 030404 (2009) (pp. 49, 58, 59, and 71)
- Filipp S and Sjöqvist E. 'Off-diagonal geometric phase for mixed states'. *Phys. Rev. Lett.* **90**, 050403 (2003) (p. 11)
- Fink J. *Quantum nonlinearities in strong coupling circuit QED*. Ph.D. thesis, ETH Zurich (2010) (p. 19)
- Fink J M, Göppl M, Baur M, Bianchetti R, Leek P J, Blais A and Wallraff A. 'Climbing the Jaynes-Cummings ladder and observing its nonlinearity in a cavity QED system'. *Nature* **454**, 315 (2008) (pp. 15 and 19)
- Fink J M, Steffen L, Studer P, Bishop L S, Baur M, Bianchetti R, Bozyigit D, Lang C, Filipp S, Leek P J and Wallraff A. 'Quantum-to-classical transition in cavity quantum electrodynamics'. *Phys. Rev. Lett.* **105**, 163601 (2010) (pp. 21 and 23)
- Foot C J. *Atomic Physics*. Oxford University Press (2007) (p. 91)
- Gambetta J M, Houck A A and Blais A. 'Superconducting qubit with Purcell protection and tunable coupling'. *Phys. Rev. Lett.* **106**, 030502 (2011) (p. 32)
- García de Polavieja G and Sjöqvist E. 'Extending the quantal adiabatic theorem: Geometry of noncyclic motion'. *Am. J. Phys.* **66**, 431 (1998) (p. 11)
- Gevorgian S, Linnér L J P and Kollberg E L. 'CAD models for shielded multilayered CPW'. *IEEE T. Microw. Theory.* **43(2)**, 772 (1995) (p. 17)
- Gillespie D T. 'The mathematics of Brownian motion and Johnson noise'. *Am. J. Phys.* **64(3)**, 225 (1996) (pp. 95 and 96)
- Glauber R J. 'The quantum theory of optical coherence'. *Phys. Rev.* **130**, 2529 (1963) (p. 49)

- Göppl M, Fragner A, Baur M, Bianchetti R, Filipp S, Fink J M, Leek P J, Puebla G, Steffen L and Wallraff A. 'Coplanar waveguide resonators for circuit quantum electrodynamics'. *J. Appl. Phys.* **104**, 113904 (2008) (pp. 16, 17, and 18)
- Hannay J H. 'Angle variable holonomy in adiabatic excursion of an integrable Hamiltonian'. *Journal of Physics A: Mathematical and General* **18**, 221 (1985) (p. 1)
- Harman A K, Ninomiya S and Adachi S. 'Optical constants of sapphire (α -Al₂O₃) single crystals'. *Journal of Applied Physics* **76**, 8032 (1994) (p. 17)
- Haroche S and Raimond J M. *Exploring the Quantum: Atoms, Cavities, and Photons*. Oxford University Press, New York, USA (2006) (p. 13)
- Hill G (ed.). *The Cable and Telecommunications Professionals' Reference*, vol. 2: Transport Networks. Focal Press, Waltham, 3rd edition edn. (2008) (p. 27)
- Hoi I C, Wilson C M, Johansson G, Palomaki T, Peropadre B and Delsing P. 'Demonstration of a single-photon router in the microwave regime'. *Phys. Rev. Lett.* **107**, 073601 (2011) (p. 39)
- Houck A A, Schreier J A, Johnson B R, Chow J M, Koch J, Gambetta J M, Schuster D I, Frunzio L, Devoret M H, Girvin S M and Schoelkopf R J. 'Controlling the spontaneous emission of a superconducting transmon qubit'. *Phys. Rev. Lett.* **101**, 080502 (2008) (p. 41)
- Ithier G, Collin E, Joyez P, Meeson P J, Vion D, Esteve D, Chiarello F, Shnirman A, Makhlin Y, Schrieffer J and Schön G. 'Decoherence in a superconducting quantum bit circuit'. *Phys. Rev. B* **72**, 134519 (2005) (p. 64)
- Jaynes E and Cummings F. 'Comparison of quantum and semiclassical radiation theories with application to the beam maser'. *Proceedings of the IEEE* **51**, 89 (1963) (p. 18)
- Ježek M, Fiurášek J and Hradil Z. 'Quantum inference of states and processes'. *Phys. Rev. A* **68**, 012305 (2003) (p. 47)
- Jin X Y, Kamal A, Sears A P, Gudmundsen T, Hover D, Miloxi J, Slattey R, Yan F, Yoder J, Orlando T P, Gustavsson S and Oliver W D. 'Thermal and residual excited-state population in a 3D transmon qubit'. <http://arxiv.org/abs/1412.2772> (2014) (p. 29)
- Johansson J, Saito S, Meno T, Nakano H, Ueda M, Semba K and Takayanagi H. 'Vacuum Rabi oscillations in a macroscopic superconducting qubit LC oscillator system'. *Phys. Rev. Lett.* **96**, 127006 (2006) (p. 19)
- Johansson M, Sjöqvist E, Andersson L M, Ericsson M, Hessmo B, Singh K and Tong D M. 'Robustness of non-adiabatic holonomic gates'. *Phys. Rev. A* **86**, 062322 (2012) (p. 77)
- Jones J A, Vedral V, Ekert A and Castagnoli G. 'Geometric quantum computation using nuclear magnetic resonance'. *Nature* **403**, 869 (2000) (pp. 12, 42, and 63)
- Joos E, Zeh H D, Kiefer C, Giulini D J W, Kupsch J and Stamatescu I O. *Decoherence and the appearance of a classical world in quantum theory*. Springer, Heidelberg & Berlin (2003) (p. 49)

- Kamleitner I, Solinas P, Müller C, Shnirman A and Möttönen M. 'Geometric quantum gates with superconducting qubits'. *Phys. Rev. B* **83**, 214518 (2011) (p. 78)
- Khanna G, Mukhopadhyay S, Simon R and Mukunda N. 'Geometric phases for $su(3)$ representations and three level quantum systems'. *Ann. Phys.* **253**, 55 (1997) (p. 8)
- Knill E, Laflamme R and Viola L. 'Theory of quantum error correction for general noise'. *Phys. Rev. Lett.* **84**, 2525 (2000) (p. 77)
- Koch J, Yu T M, Gambetta J, Houck A A, Schuster D I, Majer J, Blais A, Devoret M H, Girvin S M and Schoelkopf R J. 'Charge-insensitive qubit design derived from the Cooper pair box'. *Phys. Rev. A* **76**, 042319 (2007) (pp. 5, 14, 18, 19, 20, 29, 39, and 62)
- Kuratsuji H and Iida S. 'Effective action for adiabatic process: Dynamical meaning of Berry and Simon's phase'. *Prog. Theor. Phys.* **74**, 439 (1985) (p. 11)
- Kwiat P G and Chiao R Y. 'Observation of a nonclassical Berry's phase for the photon'. *Phys. Rev. Lett.* **66**, 588 (1991) (p. 12)
- Ladd T D, Jelezko F, Laflamme R, Nakamura Y, Monroe C and O'Brien J L. 'Quantum computers'. *Nature* **464**, 45 (2010) (p. 49)
- Lang C, Bozyigit D, Salathe Y, Eichler C and Wallraff A. 'Quantum signal analyzer for itinerant microwave radiation'. in preparation (2013) (p. 29)
- Leek P J, Fink J M, Blais A, Bianchetti R, Göppl M, Gambetta J M, Schuster D I, Frunzio L, Schoelkopf R J and Wallraff A. 'Observation of Berry's phase in a solid-state qubit'. *Science* **318**, 1889 (2007) (pp. 12, 39, 41, 42, 49, 59, and 63)
- Li X and Shi Y. 'Effect of decoherence on the berry phase of a spin-half in a rotating magnetic field'. *EPL (Europhysics Letters)* **103**, 20005 (2013) (p. 59)
- Lidar D A, Chuang I L and Whaley K B. 'Decoherence-free subspaces for quantum computation'. *Phys. Rev. Lett.* **81**, 2594 (1998) (p. 77)
- Liu Y. *Implementation and Characterization of 16-port Devices in Circuit Quantum Electrodynamics*. Master's thesis, ETH Zurich (2012) (p. 24)
- Lombardo F C and Villar P I. 'Corrections to the berry phase in a solid-state qubit due to low-frequency noise'. *Phys. Rev. A* **89**, 012110 (2014) (p. 59)
- Lupo C and Aniello P. 'Robustness of the geometric phase under parametric noise'. *Phys. Scr.* **79**, 065012 (2009) (p. 58)
- Makhlin Y, Schön G and Shnirman A. 'Quantum-state engineering with Josephson-junction devices'. *Rev. Mod. Phys.* **73**, 357 (2001) (p. 14)
- Malles K S and Mukunda N. 'The algebra and geometry of $SU(3)$ matrices'. *Pramana - J. Phys.* **49**, 371 (1997) (p. 7)

- Mallet F, Ong F R, Palacios-Laloy A, Nguyen F, Bertet P, Vion D and Esteve D. 'Single-shot qubit readout in circuit quantum electrodynamics'. *Nat. Phys.* **5**, 791 (2009) (p. 39)
- Manini N and Pistoiesi F. 'Off-diagonal geometric phases'. *Phys. Rev. Lett.* **85**, 3067 (2000) (p. 11)
- Martín-Martínez E, Dragan A, Mann R B and Fuentes I. 'Berry phase quantum thermometer'. *New J. Phys.* **15**, 053036 (2013) (pp. 59 and 78)
- Martín-Martínez E, Fuentes I and Mann R B. 'Using Berry's phase to detect the Unruh effect at lower accelerations'. *Phys. Rev. Lett.* **107**, 131301 (2011) (p. 78)
- Mead C A and Truhlar D G. 'On the determination of Born-Oppenheimer nuclear motion wave functions including complications due to conical intersections and identical nuclei'. *J. Chem. Phys.* **70**, 2284 (1979) (p. 1)
- Megrant A, Neill C, Barends R, Chiaro B, Chen Y, Feigl L, Kelly J, Lucero E, Mariantoni M, O'Malley P J J, Sank D, Vainsencher A, Wenner J, White T C, Yin Y, Zhao J, Palmstrom C J, Martinis J M and Cleland A N. 'Planar superconducting resonators with internal quality factors above one million'. *Appl. Phys. Lett.* **100**, 113510 (2012) (p. 18)
- Messiah A. *Quantenmechanik I*. deGruyter, Berlin (1991) (p. 8)
- Mlynek J A, Abdumalikov A A, Fink J M, Steffen L, Baur M, Lang C, van Loos A F and Wallraff A. 'Demonstrating W-type entanglement of Dicke states in resonant cavity quantum electrodynamics'. *Phys. Rev. A* **86**, 053838 (2012) (p. 19)
- Möttönen M, Vartiainen J J and Pekola J P. 'Experimental determination of the Berry phase in a superconducting charge pump'. *Phys. Rev. Lett.* **100**, 177201 (2008) (p. 12)
- Motzoi F, Gambetta J M, Rebentrost P and Wilhelm F K. 'Simple pulses for elimination of leakage in weakly nonlinear qubits'. *Phys. Rev. Lett.* **103**, 110501 (2009) (pp. 15 and 32)
- Mousolou V A, Canali C M and Sjöqvist E. 'Universal non-adiabatic holonomic gates in quantum dots and single-molecule magnets'. *New Journal of Physics* **16**, 013029 (2014) (p. 77)
- Mousolou V A and Sjöqvist E. 'Non-Abelian geometric phases in a system of coupled quantum bits'. *Phys. Rev. A* **89**, 022117 (2014) (p. 77)
- Mur-Petit J, García-Ripoll J J, Pérez-Ríos J, Campos-Martínez J, Hernández M I and Willitsch S. 'Temperature-independent quantum logic for molecular spectroscopy'. *Phys. Rev. A* **85**, 022308 (2012) (p. 59)
- Nakagawa N. 'Geometrical phase factors and higher-order adiabatic approximations'. *Annals of Physics* **179**, 145 (1987) (p. 11)
- Nakahara M. *Geometry, topology and physics*. Institute of Physics, Bristol and Philadelphia, 2nd edn. (2003) (pp. 6, 9, and 12)

- Nakahara M and Ohmi T. *Quantum Computing: From Linear Algebra to Physical Realizations*. Taylor & Francis Group (2008) (p. 5)
- Nakamura Y, Chen C D and Tsai J S. 'Spectroscopy of energy-level splitting between two macroscopic quantum states of charge coherently superposed by Josephson coupling'. *Phys. Rev. Lett.* **79**, 2328 (1997) (p. 14)
- Neeley M, Ansmann M, Bialczak R C, Hofheinz M, Lucero E, O'Connell A D, Sank D, Wang H, Wenner J, Cleland A N, Geller M R and Martinis J M. 'Emulation of a quantum spin with a superconducting phase qubit'. *Science* **325**, 722 (2009) (p. 39)
- Nielsen M A and Chuang I L. *Quantum Computation and Quantum Information*. Cambridge University Press, Cambridge (2000) (pp. 5 and 7)
- Pachos J K. *Introduction to topological quantum computation*. Cambridge University Press, Cambridge (2012) (p. 12)
- Paik H, Schuster D I, Bishop L S, Kirchmair G, Catelani G, Sears A P, Johnson B R, Reagor M J, Frunzio L, Glazman L I, Girvin S M, Devoret M H and Schoelkopf R J. 'Observation of high coherence in Josephson junction qubits measured in a three-dimensional circuit QED architecture'. *Phys. Rev. Lett.* **107**, 240501 (2011) (p. 18)
- Paladino E, Galperin Y, Falci G and Altshuler B. ' $1/f$ noise: Implications for solid-state quantum information'. *Rev. Mod. Phys.* **86**, 361 (2014) (p. 64)
- Pancharatnam S. 'Generalized theory of interference and its applications'. *Proc. Indian Acad. Sci.* **A44**, 247 (1956) (pp. 1 and 11)
- Paris M G A and Řeháček J (eds.). *Quantum State Estimation*, vol. 649 of *Lect. Notes Phys.* Springer, Berlin, Heidelberg (2004) (p. 55)
- Pechal M. *Berry phase in a weakly anharmonic qubit coupled to a microwave resonator*. Master's thesis, ETH Zurich (2010) (p. 44)
- Peres. *Quantum Theory: Concepts and Methods*. Kluwer Academic Publishers (2002) (p. 5)
- Pikovski I, Vanner M R, Aspelmeyer M, Kim M S and Brukner C. 'Probing Planck-scale physics with quantum optics'. *Nat. Phys.* **8**, 393 (2012) (p. 78)
- Pozar D M. *Microwave engineering*. John Wiley & Sons, Inc., New York, 4th edn. (2012) (pp. 16, 81, and 82)
- Quan H T, Song Z, Liu X F, Zanardi P and Sun C P. 'Decay of Loschmidt echo enhanced by quantum criticality'. *Phys. Rev. Lett.* **96**, 140604 (2006) (p. 78)
- Reed M D, DiCarlo L, Johnson B R, Sun L, Schuster D I, Frunzio L and Schoelkopf R J. 'High-fidelity readout in circuit quantum electrodynamics using the Jaynes-Cummings nonlinearity'. *Phys. Rev. Lett.* **105**, 173601 (2010) (p. 20)

- Resta R. 'Manifestations of Berry's phase in molecules and condensed matter'. *Journal of Physics: Condensed Matter* **12**, R107 (2000) (p. 12)
- Rezakhani A T and Zanardi P. 'General setting for a geometric phase of mixed states under an arbitrary nonunitary evolution'. *Phys. Rev. A* **73**, 012107 (2006) (p. 78)
- Rice S O. 'Mathematical analysis of random noise'. *Bell System Technical Journal* **23**, 282 (1944) (pp. 97 and 98)
- Richardson D J, Kilvington A I, Green K and Lamoreaux S K. 'Demonstration of Berry's phase using stored ultracold neutrons'. *Phys. Rev. Lett.* **61**, 2030 (1988) (p. 12)
- Robinson F N H. *Noise and fluctuations in electronic devices and circuits*. Clarendon Press (1974) (p. 49)
- Rong X, Huang P, Kong X, Xu X, Shi F, Wang Y and Du J. 'Enhanced phase estimation by implementing dynamical decoupling in a multi-pass quantum metrology protocol'. *Europhys. Lett.* **95**, 6 (2011) (pp. 59 and 78)
- Sakurai J J. *Modern quantum mechanics*. Addison-Wesley, Reading, revised edn. (1994) (p. 12)
- Samuel J and Bhandari R. 'General setting for Berry's phase'. *Phys. Rev. Lett.* **60**, 2339 (1988) (pp. 11, 51, and 58)
- Schlosshauer M. *Decoherence and the Quantum-to-Classical Transition*. Springer, Heidelberg Berlin (2007) (p. 49)
- Sillanpää M A, Li J, Cicak K, Altomare F, Park J I, Simmonds R W, Paraoanu G S and Hakonen P J. 'Autler-Townes effect in a superconducting three-level system'. *Phys. Rev. Lett.* **103**, 193601 (2009) (p. 39)
- Simon B. 'Holonomy, the quantum adiabatic theorem, and Berry's phase'. *Phys. Rev. Lett.* **51**, 2167 (1983) (pp. 1 and 11)
- Simons R N. *Coplanar waveguide circuits, components and systems*. Wiley Series in Microwave and Optical Engineering. Wiley Inter-Science (2001) (pp. 16 and 17)
- Sjöqvist E. 'Proposed interferometry test of noncyclic geometric phase'. *Physics Letters A* **286**, 4 (2001) (p. 12)
- . 'A new phase in quantum computation'. *Physics* **1**, 35 (2008) (pp. 12 and 49)
- Sjöqvist E, Pati A K, Ekert A, Anandan J S, Ericsson M, Oi D K L and Vedral V. 'Geometric phases for mixed states in interferometry'. *Phys. Rev. Lett.* **85**, 2845 (2000) (pp. 11 and 78)
- Sjöqvist E, Tong D M, Andersson L M, Hessmo B, Johansson M and Singh K. 'Non-adiabatic holonomic quantum computation'. *New J. Phys.* **14**, 103035 (2012) (pp. 13, 39, and 77)

- Solinas P, Möttönen M, Salmilehto J and Pekola J P. 'Decoherence of adiabatically steered quantum systems'. *Phys. Rev. B* **82**, 134517 (2010) (pp. 49 and 72)
- Solinas P, Sassetti M, Truini P and Zanghi N. 'On the stability of quantum holonomic gates'. *New J. Phys.* **14**, 093006 (2012) (p. 49)
- Solinas P, Zanardi P, Zanghi N and Rossi F. 'Holonomic quantum gates: A semiconductor-based implementation'. *Phys. Rev. A* **67**, 062315 (2003) (p. 78)
- Srinivasan S J, Hoffman A J, Gambetta J M and Houck A A. 'Tunable coupling in circuit quantum electrodynamics using a superconducting charge qubit with a V-shaped energy level diagram'. *Phys. Rev. Lett.* **106**, 083601 (2011) (p. 62)
- Steffen L. *Quantum Teleportation and Efficient Process Verification with Superconducting Circuits*. Ph.D. thesis, ETH Zurich (2013) (pp. 16, 17, 18, and 21)
- Steffen M, Martinis J M and Chuang I L. 'Accurate control of Josephson phase qubits'. *Phys. Rev. B* **68**, 224518 (2003) (p. 15)
- Suter D, Chingas G C, Harris R A and Pines A. 'Berry's phase in magnetic resonance'. *Molecular Physics* **61**, 1327 (1987) (p. 12)
- Suter D, Mueller K T and Pines A. 'Study of the Aharonov-Anandan quantum phase by NMR interferometry'. *Phys. Rev. Lett.* **60**, 1218 (1988) (p. 12)
- Taguchi Y, Oohara Y, Yoshizawa H, Nagaosa N and Tokura Y. 'Spin chirality, Berry phase, and anomalous Hall effect in a frustrated ferromagnet'. *Science* **291**, 2573 (2001) (p. 12)
- Thompson R J, Rempe G and Kimble H J. 'Observation of normal-mode splitting for an atom in an optical cavity'. *Phys. Rev. Lett.* **68**, 1132 (1992) (p. 13)
- Thouless D J, Kohmoto M, Nightingale M P and den Nijs M. 'Quantized hall conductance in a two-dimensional periodic potential'. *Phys. Rev. Lett.* **49**, 405 (1982) (p. 1)
- Tinkham M. *Introduction to Superconductivity*. McGraw-Hill (1996) (p. 14)
- Tomita A and Chiao R Y. 'Observation of Berry's topological phase by use of an optical fiber'. *Phys. Rev. Lett.* **57**, 937 (1986) (p. 12)
- Tong D M, Sjöqvist E, Kwek L C and Oh C H. 'Kinematic approach to the mixed state geometric phase in nonunitary evolution'. *Phys. Rev. Lett.* **93**, 080405 (2004) (p. 78)
- Toyoda K, Uchida K, Noguchi A, Haze S and Urabe S. 'Realization of holonomic single-qubit operations'. *Phys. Rev. A* **87** (2013) (pp. 12 and 77)
- Tycko R. 'Adiabatic rotational splittings and Berry's phase in nuclear-quadrupole resonance'. *Phys. Rev. Lett.* **58**, 2281 (1987) (p. 12)
- Uhlmann A. 'Parallel transport and 'quantum holonomy' along density operators'. *Rep. Math. Phys.* **24**, 229 (1986) (pp. 11 and 78)

- Unanyan R G, Shore B W and Bergmann K. 'Laser-driven population transfer in four-level atoms: Consequences of non-abelian geometrical adiabatic phase factors'. *Phys. Rev. A* **59**, 2910 (1999) (p. 77)
- Unruh W G. 'Notes on black-hole evaporation'. *Phys. Rev. D* **14**, 870 (1976) (p. 78)
- van Loo A, Fedorov A, Lalumière K, Sanders B, Blais A and Wallraff A. 'Photon-mediated interactions between distant artificial atoms'. *Science* **342**, 1494 (2013) (p. 17)
- Villar P I and Lombardo F C. 'Geometric phases in the presence of a composite environment'. *Phys. Rev. A* **83**, 052121 (2011) (p. 49)
- Vion D, Aassime A, Cottet A, Joyez P, Pothier H, Urbina C, Esteve D and Devoret M H. 'Manipulating the quantum state of an electrical circuit'. *Science* **296**, 886 (2002) (p. 14)
- Wagh A, Rakhecha V, Fischer P and Ioffe A. 'Neutron interferometric observation of non-cyclic phase'. *Phys. Rev. Lett.* **81**, 1992 (1998) (p. 12)
- Wallraff A, Schuster D I, Blais A, Frunzio L, Huang R S, Majer J, Kumar S, Girvin S M and Schoelkopf R J. 'Strong coupling of a single photon to a superconducting qubit using circuit quantum electrodynamics'. *Nature* **431**, 162 (2004) (pp. 14 and 19)
- Weinfurter H and Badurek G. 'Measurement of Berry's phase for noncyclic evolution'. *Phys. Rev. Lett.* **64**, 1318 (1990) (p. 12)
- Wen C. 'Coplanar waveguide: A surface strip transmission line suitable for nonreciprocal gyromagnetic device applications'. *IEEE Trans. Microwave Theory Tech.* **17**, 1087 (1969) (p. 16)
- Whitney R S and Gefen Y. 'Berry phase in a nonisolated system'. *Phys. Rev. Lett.* **90**, 190402 (2003) (p. 49)
- Whitney R S, Makhlin Y, Shnirman A and Gefen Y. 'Geometric nature of the environment-induced Berry phase and geometric dephasing'. *Phys. Rev. Lett.* **94**, 070407 (2005) (pp. 49, 58, 61, and 65)
- Wilczek F and Shapere A (eds.). *Geometric Phases in Physics*. World Scientific, Singapore (1989) (p. 11)
- Wilczek F and Zee A. 'Appearance of gauge structure in simple dynamical systems'. *Phys. Rev. Lett.* **52**, 2111 (1984) (p. 11)
- Wolff I. *Coplanar Microwave Integrated Circuits*. Wiley Inter-Science (2006) (p. 16)
- Wu H, Gauger E M, George R E, Möttönen M, Riemann H, Abrosimov N V, Becker P, Pohl H J, Itoh K M, Thewalt M L W and Morton J J L. 'Geometric phase gates with adiabatic control in electron spin resonance'. *Phys. Rev. A* **87**, 032326 (2013) (p. 49)
- Xu G F, Zhang J, Tong D M, Sjöqvist E and Kwek L C. 'Nonadiabatic holonomic quantum computation in decoherence-free subspaces'. *Phys. Rev. Lett.* **109**, 170501 (2012) (p. 77)

- Yamamoto T, Inomata K, Watanabe M, Matsuba K, Miyazaki T, Oliver W D, Nakamura Y and Tsai J S. 'Flux-driven Josephson parametric amplifier'. *Appl. Phys. Lett.* **93**, 042510 (2008) (p. 23)
- Yurke B and Buks E. 'Performance of cavity-parametric amplifiers, employing Kerr nonlinearities, in the presence of two-photon loss'. *J. Lightwave Technol.* **24**, 5054 (2006) (p. 22)
- Yurke B, Kaminsky P G, Miller R E, Whittaker E A, Smith A D, Silver A H and Simon R W. 'Observation of 4.2-K equilibrium-noise squeezing via a Josephson-parametric amplifier'. *Phys. Rev. Lett.* **60**, 764 (1988) (p. 30)
- Zanardi P and Rasetti M. 'Holonomic quantum computation'. *Phys. Lett. A* **264**, 94 (1999) (p. 12)
- Zhang J, Kwek L C, Sjöqvist E, Tong D M and Zanardi P. 'Quantum computation in noiseless subsystems with fast non-abelian holonomies'. *Phys. Rev. A* **89**, 042302 (2014) (p. 77)
- Zhang Y B, Tan Y W, Stormer H L and Kim P. 'Experimental observation of the quantum Hall effect and Berry's phase in graphene'. *Nature* **438**, 201 (2005) (p. 12)
- Zhu J, Shi M, Vedral V, Peng X, Suter D and Du J. 'Experimental demonstration of a unified framework for mixed-state geometric phases'. *Europhys. Lett.* **94**, 20007 (2011) (p. 78)
- Zu C, Wang W B, He L, Zhang W G, Dai C Y, Wang F and Duan L M. 'Experimental realization of universal geometric quantum gates with solid-state spins'. *Nature* **514**, 72 (2014) (pp. 13, 39, and 77)
- Zwanziger J W, Koenig M and Pines A. 'Non-Abelian effects in a quadrupole system rotating around two axes'. *Phys. Rev. A* **42**, 3107 (1990) (p. 12)

ACKNOWLEDGEMENTS

Andreas for providing shelter, equipment and scientific freedom; Jukka for taking time to be my co-examiner; Stefan for transoceanic support, and his vast stock of theoretical and experimental ideas, which he let me draw on; Simone for taking over the experiment and freeing me time to write; Romeo for first showing me—innocent still and unaware—how to measure using DirtySweep; Matthias for his work on the pulse generation library and his debugging skills; Clang for setting up the FPGA measurements, and Yves for continuing to develop it; Farruh for fabricating, troubleshooting, leak-testing, and probably many other things in ‘ing’, such as proofreading; Arjan for distracting me, either by running or by kicking or by knocking on the Mug of Vi, and for running; Marek for having lunch together and for letting me pester him with a countable infinity of questions, and proofreading; D17 (with, inter alii, Tobi, Anna, Lars, Philipp, and also our temporary crew Yulin, Michael and Lukas) for being such a cool office; Gabe for showing me how combat is properly done; Janis and Jonas for speaking Swiss German and filling Helium 6.0; Gaby for making cakes and handling the financial aspects of many a microwave-parts order; Andrea, Toni and Sina for their contributions during semester projects; 常川氏、那須田氏、辛抱づよく私の愚痴を聞いてくれてありがとうございます；親愛なる伊藤先生、伊藤研の皆様、私を温かく歓迎し、助けてくれて、厚く御礼申し上げます； my mum and dad for their support and for refraining from asking too many work-related questions; Beenzino, VJ, the King of Flow, The Quiett, 9 mm, EST, Schmittke and Chesnokov for setting the right frame of mind for writing.

CURRICULUM VITAE

Name Simon Jacques Berger
Date of birth 05/10/1985
Citizenship Swiss

Professional experience

2010 – 2015 Research assistant (with Prof. A. Wallraff) and teaching assistant, Department of Physics, ETH Zürich
2012 – 2013 Visiting researcher (with K. M. Itoh), Department of Applied Physics and Physico-Informatics, Keio University, Tokyo
2007 – 2008 Teaching assistant, Department of Mathematics, ETH Zürich (Calculus for mechanical engineers)
2005 Military service, Swiss Air Force, Payerne.

Education

2010 – 2015 PhD studies, Department of Physics, ETH Zürich, “*Geometric phases and noise in circuit QED*”
2008 – 2010 MSc Physics, ETH Zürich. Focus on particle physics and quantum computation.
2006 – 2009 Higher diploma of non-professional studies in piano, Conservatoire de Musique de Neuchâtel
2005 – 2008 BSc Physics, ETH Zürich. Focus on theoretical physics and particle physics
2002 – 2004 Diploma of non-professional studies in piano, Conservatoire de Musique de Neuchâtel
2001 – 2004 Matura, Lycée Denis-de-Rougemont, Neuchâtel. Focus on latin and physics

Zürich, February 2015